

# Oil-Flow and Distributed Roughness Experiments on CRM Wing Model

Erkki Soinne, Trafi

Title of publication <b>Oil-Flow and Distributed Roughness Experiments on CRM Wing Model</b>	
Author(s) Erkki Soinne	
Commissioned by, date Kari Wihlman, October 8th 2017	
Publication series and number <b>Trafı Research Reports 3/2018</b>	ISSN (online) 2342-0294 ISBN (online) ISBN 978-952-311-247-6 URN <a href="http://urn.fi/URN:ISBN:978-952-311-247-6">http://urn.fi/URN:ISBN:978-952-311-247-6</a>
Keywords aircraft, aerodynamics, anti-icing fluids	
Contact person Erkki Soinne	Language of the report English
Abstract This research report summarizes the oil-flow, sandpaper, anti-icing fluid and PVC plastic sheet wind tunnel experiments on the Common Research Model (CRM). The aerodynamic measurements were made with a force balance on lift and two wake rakes on the upper surface boundary layer displacement thickness aft of the model main wing. The oil-flow measurements investigated the qualitative flow characteristics.	

## **FOREWORD**

This research report is focused on the flow characteristics of CRM wing model, used for investigations in Cold Soaked Fuel Frost, which is an important subject in aviation safety. It forms part of the third year of the Frostwing project on the research of frost and anti/de-icing fluid effects on aircraft wing at take-off, performed under a Research agreement between the Federal Aviation Administration FAA and the Finnish Transport safety Agency Trafi.

Because Arteform Ltd did not want to write the report a work split was made, so that the analysis and documentation of the wind tunnel tests is done in this report based on the data and photographs provided by Arteform. The wind tunnel measurements were performed by the team of Arteform Ltd (MSc Tomi Honkanen and MSc Pekka Koivisto headed by MSc Juha Kivekäs) and their efforts to make good measurements are gratefully acknowledged.

Helsinki, November 15th 2018

Erkki Soinne

Chief Adviser, Aeronautics

Finnish Transport Safety Agency, Trafi

# Index

<b>Nomenclature .....</b>	<b>4</b>
<b>Abbreviations.....</b>	<b>4</b>
<b>1 Introduction.....</b>	<b>5</b>
<b>2 Wind tunnel test setup.....</b>	<b>6</b>
2.1 Wind tunnel.....	6
2.2 CRM wing model .....	8
2.3 Oil-Flow tests .....	13
2.4 Sandpaper tests.....	14
2.5 Anti-icing fluid tests.....	21
2.6 Plastic sheet tests .....	23
<b>3 Test results .....</b>	<b>26</b>
3.1 Performed wind tunnel runs.....	26
3.2 Oil-flow studies .....	26
3.3 Measurement accuracy in the 2017 tests.....	37
3.4 Sandpaper measurements .....	39
3.4.1 Lift coefficient .....	41
3.4.2 Boundary layer displacement thickness .....	50
3.5 Anti-icing fluid measurements.....	60
3.5.1 Lift coefficient .....	61
3.5.2 Boundary layer displacement thickness .....	67
3.6 PVC plastic sheet measurements.....	75
3.6.1 Measurement accuracy .....	76
3.6.2 Lift coefficient .....	77
3.6.3 Boundary layer displacement thickness .....	82
<b>4 Conclusions.....</b>	<b>88</b>
<b>References .....</b>	<b>89</b>

## Nomenclature

A	aspect ratio
$A_{\text{eff}}$	effective aspect ratio
b	wing span
c	airfoil chord
$C_L$	lift coefficient
$C_{L\text{Clean}}$	clean wing lift coefficient
$C_{L\alpha}$	wing lift curve slope
h	wing end plate height
k	surface roughness height
t	additional thickness
u	local flow speed within the boundary layer
U	wind tunnel speed
$U_{\text{LOC}}$	local flow speed
z	normal distance from wing surface
$\alpha$	angle of attack
$\alpha_i$	indicated angle of attack
$\delta$	boundary layer thickness
$\delta_f$	flap deflection
$\delta_s$	slat deflection
$\delta^*$	boundary layer displacement thickness

## Abbreviations

CSFF	Cold Soaked Fuel Frost
FEPA	Federation of European Producers of Abrasives
ISO	International Standardization Organization
OAT	Outside Air Temperature

## **1 Introduction**

The wing model of the modern jet aircraft Common Research Model (CRM) has been studied in preliminary wind tunnel tests with Cold Soaked Fuel Frost (CSFF) by Koivisto in ref. [1] and in ref. [2] by Soinne et al. In the present report complementary experiments are made with oil-flow, sandpaper and anti-icing fluids to characterize the wing model flow. At a later stage also measurements with a smooth PVC plastic sheet were made. Comparisons of lift losses and boundary layer thickening due to sandpapers, anti-icing fluids and the PVC sheet are made with the past CSFF results. The oil flow studies were performed to investigate the possible flow separations and the overall flow quality on the wing model.

## 2 Wind tunnel test setup

### 2.1 Wind tunnel

Arteform Low Speed Wind Tunnel is a closed circuit wind tunnel with an octagonal test section with dimensions of 2 m x 2 m and a test section length of 4 m. The test section is shown in Figure 1. The flow uniformity in the test section is better than 0.14 %, and the turbulence level is less than 0.28 % at a constant wind tunnel speed of 60 m/s. However, during acceleration the turbulence level is somewhat higher, see Figure 2. The turbulence level is relevant when a clean airfoil reference test is made. When the airfoil is contaminated (with frost or anti-icing fluid) it is not too sensitive for the tunnel turbulence level as the boundary layer is already much disturbed by the contamination.

The massive concrete structures of the wind tunnel ducts are outside the facility building. This makes the tunnel structure during winter time an efficient heat sink and the fan power, dissipated during a short period take-off run simulation, does not increase the test section temperature significantly ( $< 2^{\circ}\text{C}$ ). Temperatures in the test section follow roughly the daily outside air temperature (OAT). During the tests of this study the wind tunnel air temperature was approximately  $5^{\circ}\text{C}$ .

The temperature of the coolant tank was measured separately to follow the coolant fluid mean temperature before and during each aerodynamic test. The coolant tubing was connected to the cooling machine during this time. During the aerodynamic test the

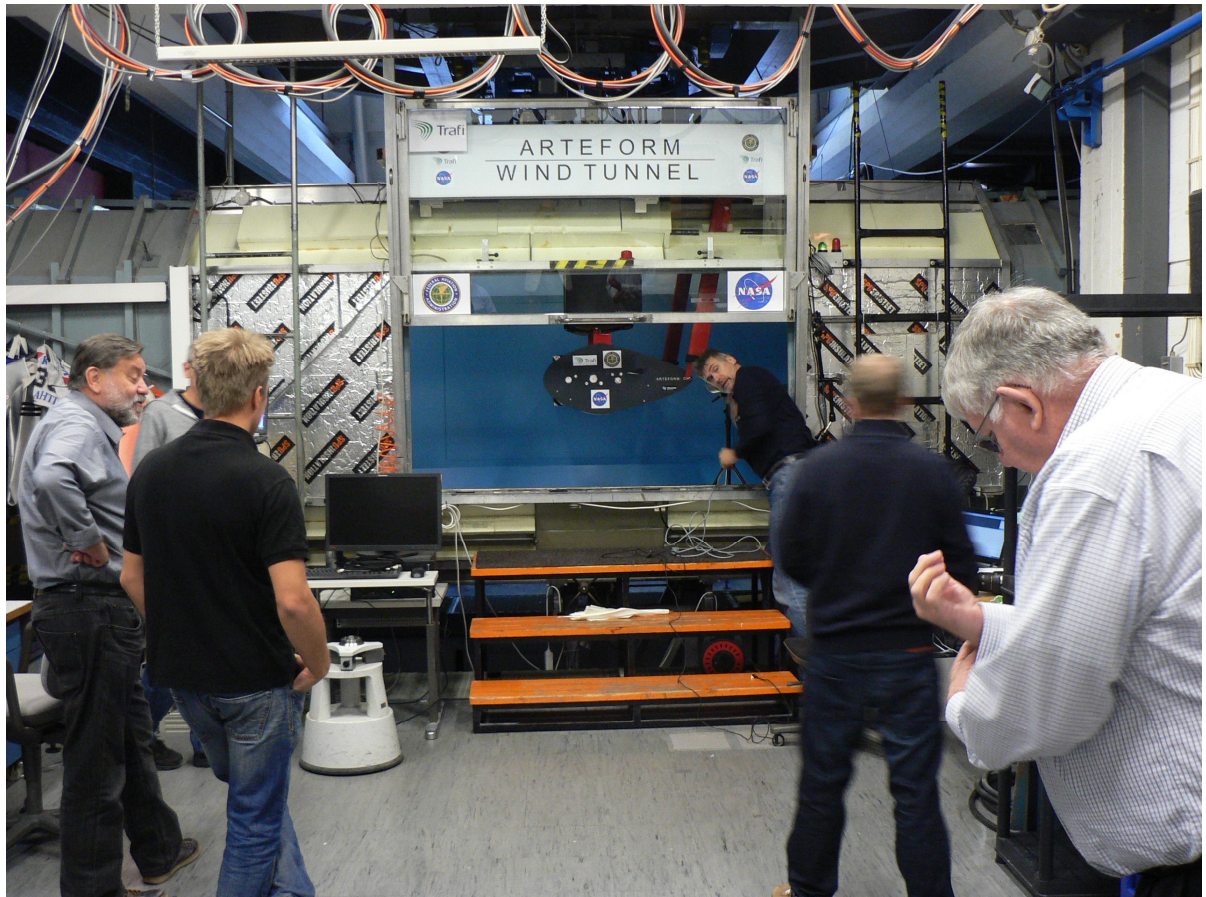


**Figure 1.** Arteform wind tunnel test section.

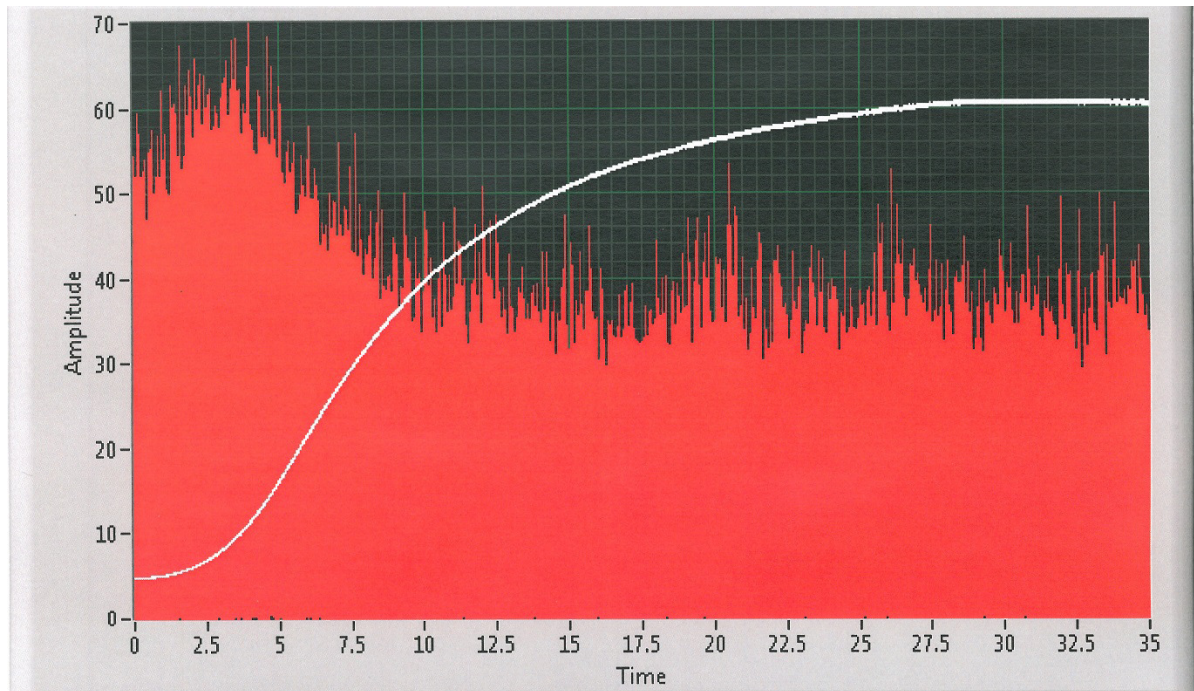


**Figure 2.** Test section turbulence level during tunnel acceleration. The white curve shows the tunnel speed in m/s and the red color the tunnel turbulence level multiplied with 10000 (Amplitude 30 corresponds to a turbulence level of 0,3 %). The measurement point was at the beginning of the test section at the octagonal test section center (Hurme ref. [3]).

coolant tubing was disconnected so as not to disturb the force measurements. Consequently the coolant temperature was not controlled during the aerodynamic tests. There were 10 temperature sensors in fuel tank inner skin, outer skin and within the fuel.

There is standard measuring software in the wind tunnel collecting the wind tunnel temperature, airspeed, dynamic pressure, relative humidity, balance forces and moments (lift, drag and pitching moment) and the wing angle of attack.

The effect of sandpaper and anti-icing fluid on the take-off performance is evaluated by measuring the lift coefficient degradation  $\Delta C_L$  due to contamination. This means sequential  $C_L$  measurements of the clean wing and a contaminated wing. As the result is a difference between the two lift coefficients at the same angle of attack, the repeatability of the tests is more relevant than the absolute accuracy of the lift coefficient itself.

## 2.2 CRM wing model

CRM is an acronym for Common Research Model of a modern jet aircraft configuration shown in Figure 3. The generic long range twin engine configuration was first optimized for cruise flight and then high lift devices were added on the wing creating a HL-CRM configuration, see Lacy&Sclafani ref. [4].

A representative section for the present studies was selected outboard of the wing planform kink as shown in Figure 4. The section was selected in the vicinity of the wing Mean Aerodynamic Chord and is free from the local flow conditions due to the engine and wing kink. In a wind tunnel test the critical flow conditions should be reproduced. Anti-icing fluid is applied on the wing upper surface only and also the possible frost on the wing upper surface is critical due to the upper surface retarding flow at high angle of attack. For this reason the section was taken in the local upper surface stream line direction. On a wing at subsonic speeds the local streamlines are directed inboard on the upper surface and outboard on the lower surface. CFD calculations in ref. [4] fig. 22 showed that in take-off configuration at high angle of attack the streamlines on the wing upper surface at the station for the representative wing section were directed  $11,3^\circ$  inboard. The wing section was taken in this direction and perpendicular to the wing leading edge to take into account the wing dihedral.

The local flow direction on the wing lower surface is outboard and cannot be exactly matched in the wind tunnel test. The upper surface flow condition is however most important to match as the effect of the lower surface condition to the upper surface is secondary even in subsonic flow. The details of the section cut are described by Kivekäs in ref. [5]. In a low speed case even on a swept wing the flow speed and the section perpendicular to the leading edge are not relevant contrary to the situation in a high-speed subsonic case.



**Figure 3.** Common Research Model of a modern jet aircraft configuration.

The original high speed configuration of the Common Research Model HS-CRM was created in the level flight condition with the wing in the deformed state as described in ref. [4]. The HS-CRM and the HL-CRM geometries are shown in Figure 5. HS-CRM geometry included a modification for practical reasons to have a trailing edge thickness of 0,20 inches in full scale to ensure a sufficient thickness on scaled down wind tunnel models. Figure 6 shows the trailing edge thicknesses of the HS-CRM and the theoretical HL-CRM configurations. To ensure on the HL-CRM model a practical trailing edge thickness of 1,5

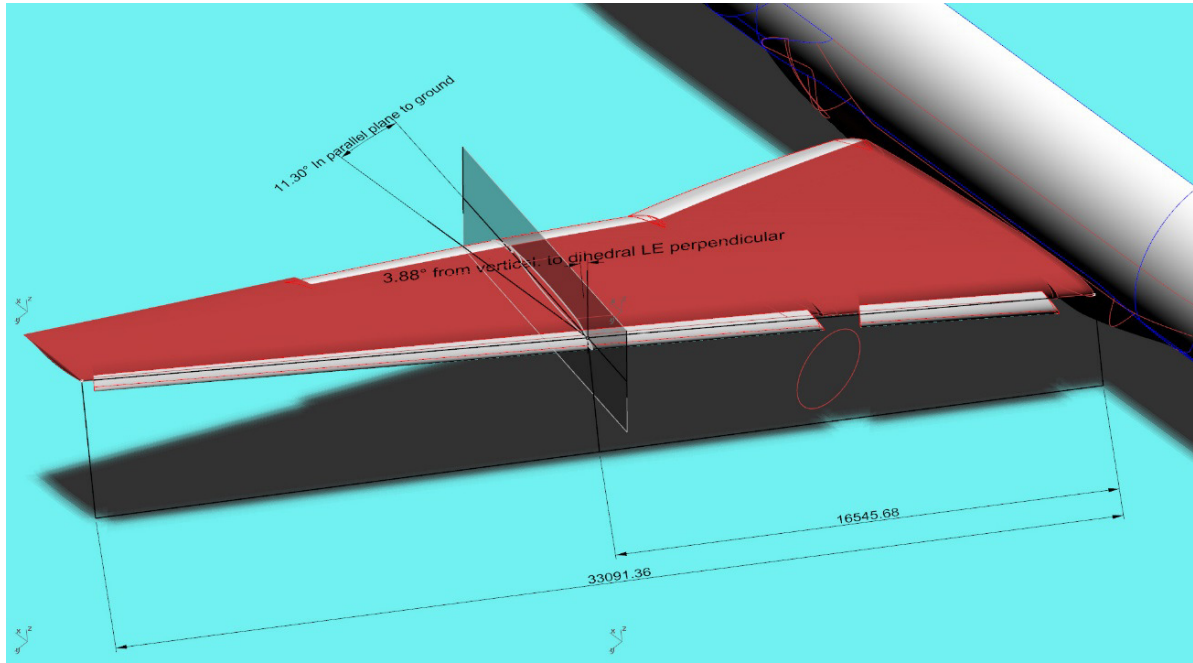


**Figure 4.** Representative wing section selection in the Common Research Model.

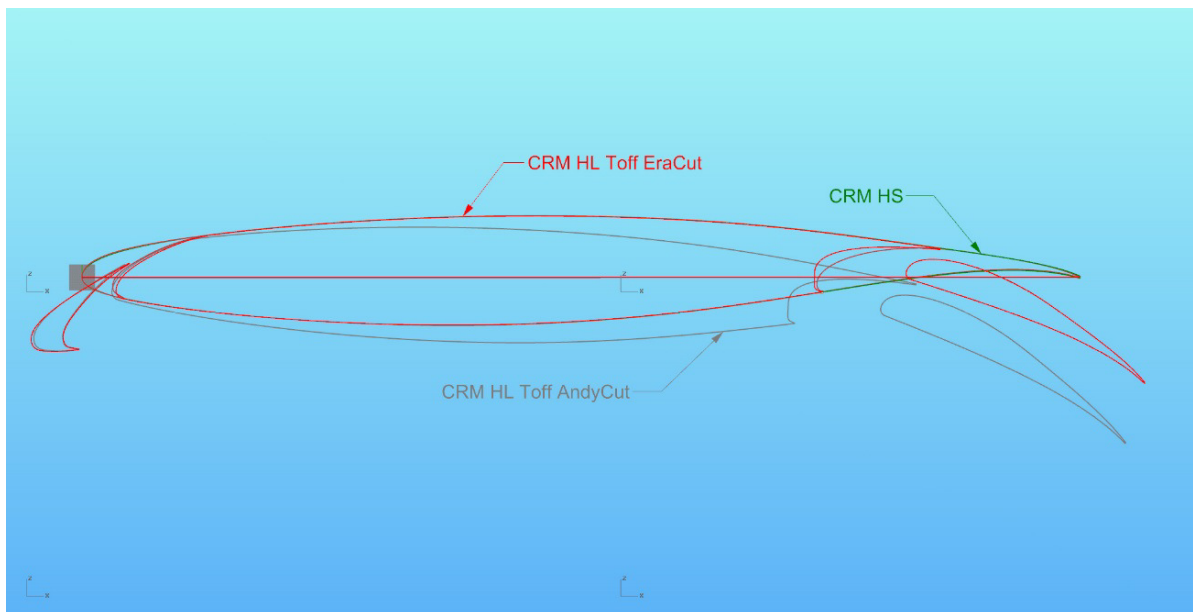


**Figure 5.** Geometries of the HS-CRM configuration (green line) and HL-CRM configuration (red line) in the selected representative section. The black line shows the HL-CRM configuration taken in a section perpendicular to the leading edge.

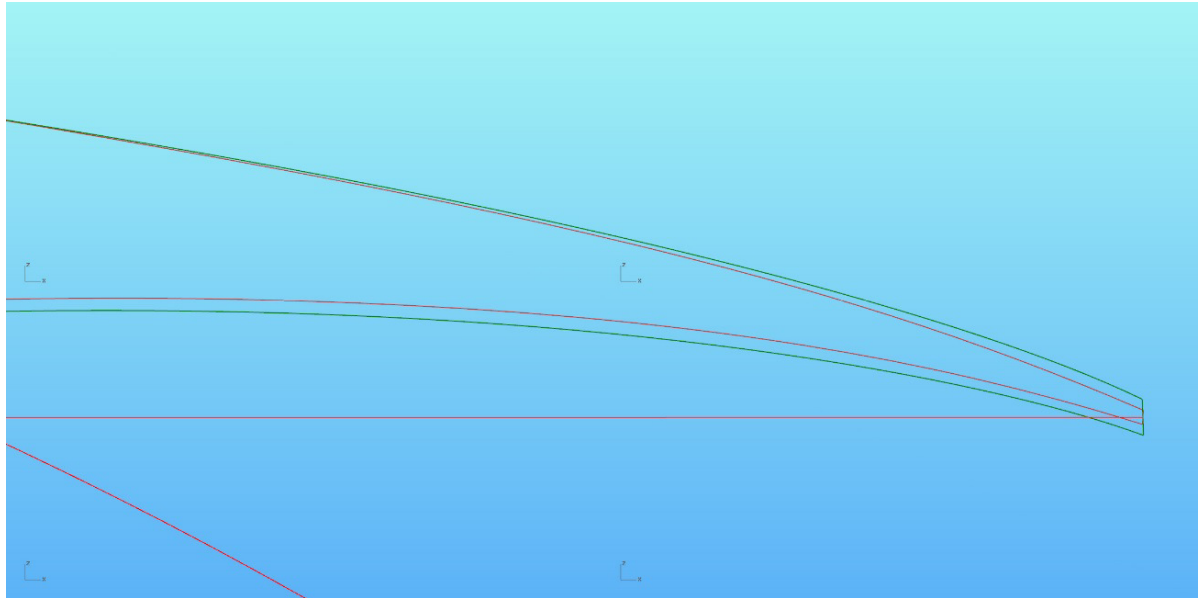


**Figure 6.** Comparison of the HS-CRM configuration (green line) and the theoretical HL-CRM configuration (red line) with the flap retracted.

mm when the airfoil chord is 625 mm the thickness was further increased linearly towards the trailing edge as shown in Figure 7. The final section to be tested is named "HL-CRM Mod" to emphasize that it is not taken parallel to a symmetry plane. However, the HL-CRM geometry is not defined by 2D sections parallel to a symmetry plane but a 3D surface. The 3D external surface geometry is not modified except at the vicinity of the trailing edge which is an insignificant modification.

The chord of 625 mm and span of 1550 mm of the rectangular wing model were chosen as a compromise of Reynolds number, test section blockage (wind tunnel corrections) and tunnel balance forces. Also for the take-off unusually large flap angle of  $25^\circ$  was reduced to  $10^\circ$  regarding the maximum balance forces. So in the tests the slat deflection was  $22^\circ$  and the flap deflection  $10^\circ$ , see Figure 8. In the ground roll the angle of attack  $\alpha$  was  $0^\circ$  giving for the wing model a lift coefficient of  $C_L=0,52$ . The rotation was made to  $9,2^\circ$  corresponding to a lift coefficient of  $C_L=1,50$  for the wing model.

To improve the two-dimensionality of the flow end plates were designed for the model. Without the end plates the wing model nominal aspect ratio is  $A=2,48$ . The effect of the end plates can be estimated in free flight with expression (ref. [6] Hoerner page 3-9)

$$A_{eff} = A(1 + 1,9 \frac{h}{b}) \quad (1)$$

where  $h$  is the end plate height and  $b$  the wing span. The end plates increase the model effective aspect ratio nominally to 3,696. In the tunnel test section the flow is constrained by the test section walls and the effective aspect ratio may be higher. The CRM wing model lift curve slope in the interval of angle of attack values  $\alpha=4^\circ \dots 8^\circ$  was measured for the configuration  $\delta_s=22^\circ$  and  $\delta_f=10^\circ$  as 6,103 per radian (ref. [1] page 6). Assuming a sectional lift curve slope of  $2\pi$  the effective aspect ratio can be calculated using the expression (ref. [7] Torenbeek page 473)

$$C_{L\alpha} = \frac{2\pi}{1 + 3/A} \quad (2)$$

Solving for the aspect ratio and using the measured value for the model wing lift curve

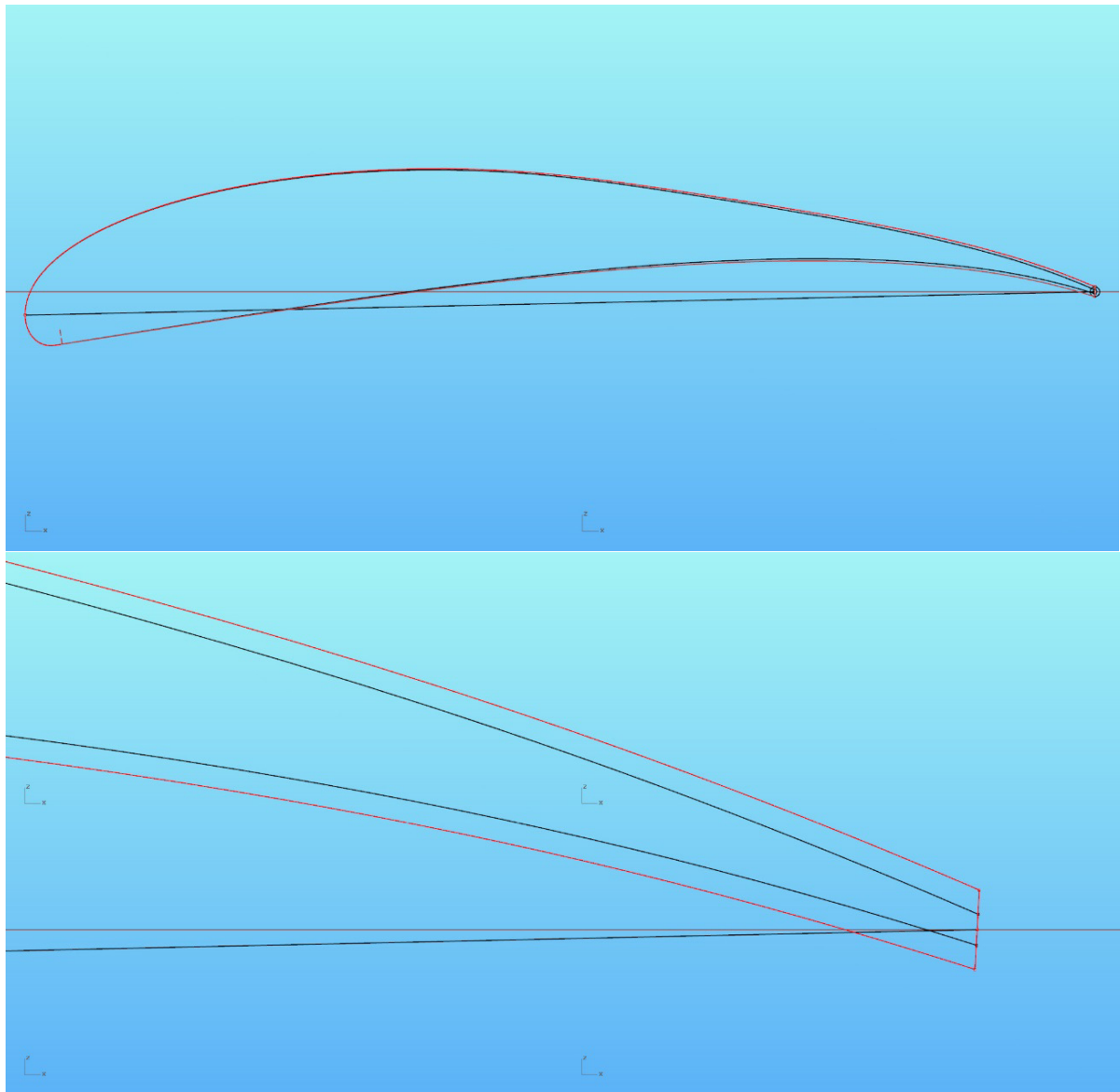


**Figure 7.** Comparison at the flap area of the theoretical HL-CRM configuration (black line) and the thickened HL-CRM configuration (red line).

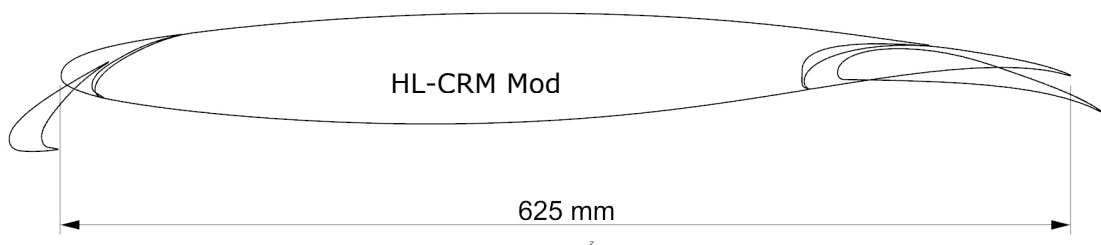


**Figure 8.** HL-CRM Mod wing model section with a slat deflection of  $22^\circ$  and flap deflection of  $10^\circ$  as used in the simulated take-off tests in the wind tunnel.

slope the expression gives for the model wing effective aspect ratio a value 101,8. This indicates that the model wing tips with the end plates are so close to the tunnel walls that the flow is quite close to a two-dimensional case. The flow in the wind tunnel test section is also constrained in vertical direction as the wing is in ground effect. According to Torenbeek (reference [7]) page 553 the effects of induced upwash and increased camber

increase the lift at moderate lift coefficients whereas at high values there is a reduction in lift due to a decrement in the local flow velocity. The airfoil pressure distribution may change considerably in the vicinity of ground in particular when effective trailing edge flaps are used. The end plates contain a hole in the vicinity of the flap leading edge to ensure flow attachment. The wing model is shown in Figure 9.

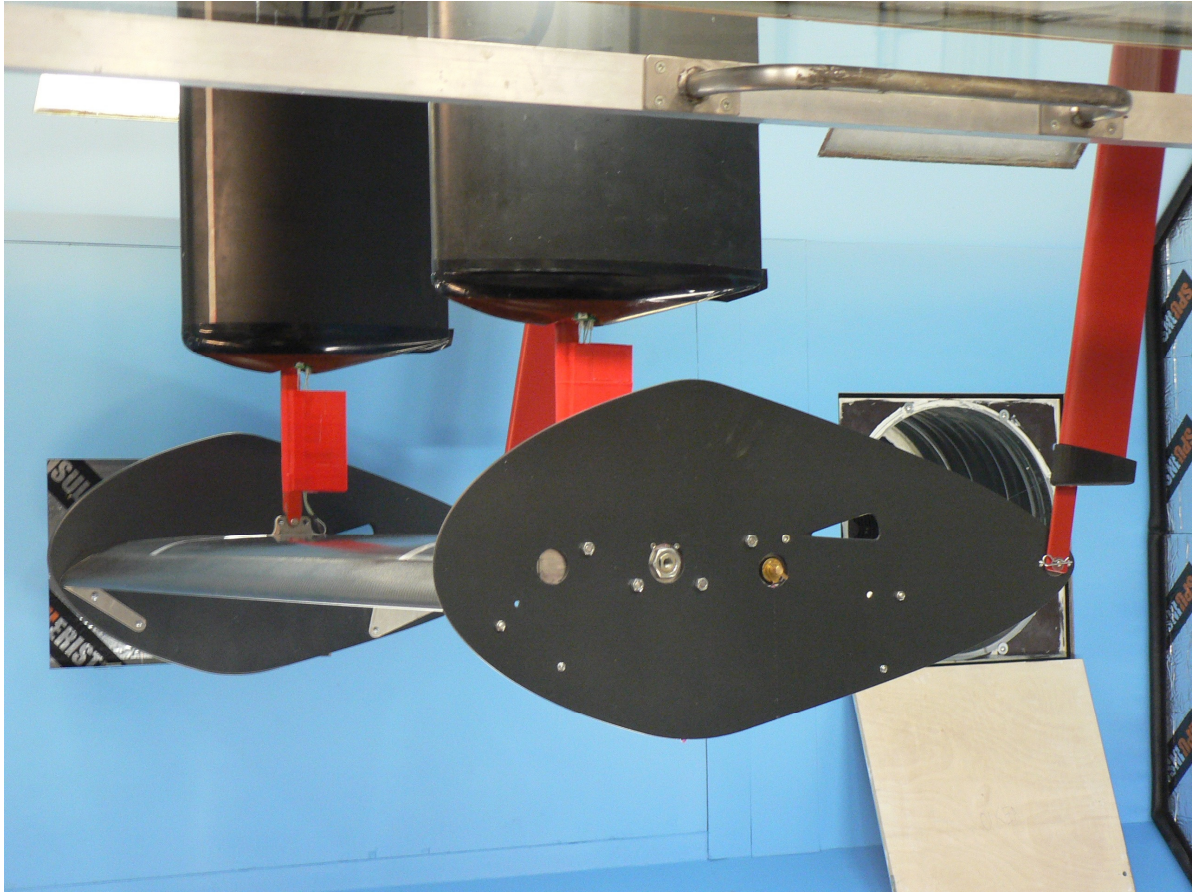


**Figure 9.** HL-CRM Mod wing model in the Arteform wind tunnel test section.

## 2.3 Oil-Flow tests

The past wind tunnel measurements on CSFF simulated and airliner take-off sequence. It began with a ground roll at zero angle of attack which gave a lift coefficient of about  $C_L=0,52$ . The speed increased in 30 seconds to 60 m/s and was then kept constant. When the speed reached the value 60 m/s the angle of attack was increased to  $9,2^\circ$  corresponding to a lift coefficient value of  $C_L=1,50$ . The nominal rotation rate was  $4,5^\circ/s$ . The test sequence (see Figure 10) is a compromise and was designed with a slat deflection  $22^\circ$  and flap deflection  $10^\circ$ . The wing model Reynolds number at the velocity of 60 m/s was about 2,5 million. The take-off sequence was designed by Koivisto in ref. [8], in which he explains the background and motivations for the selected simplifications.

The critical instant for the take-off is just after the rotation when the CSFF and anti-icing fluids have their largest effect on lift degradation. Due to the high angle of attack there is a risk of flow separation which would start at the junction of the wing model upper surface and the end plate, probably somewhere upstream of the flap slot. This test case was investigated with oil-flow technique to qualitatively study the flow characteristics. A mixture of 0,25 liters of lamp oil and 5 grams of titanium dioxide was used in the tests. The mixture of Kegerise&Neuhart ref. [9] page 15 was not known at the time of testing. Due to the tendency of the solvent to vaporize before reaching the 60 m/s tunnel speed the tests were conducted at a lower speed of 30 m/s. The corresponding model Reynolds number during the tests was about 1,3 million. It is generally known that the risk for flow separation increases with decreasing speed and Reynolds number. An example of this is shown in fig. 24 of ref. [9] in which results of oil-flow studies at a wing fuselage junction are studied at Reynolds numbers 0,62 million and 2,4 million. Also the Reynolds number in the present tests is so high that the flow characteristics regarding flow laminarisation, laminar separation and reattachment would not likely change, because these phenomena normally appear below Reynolds number 1 million.

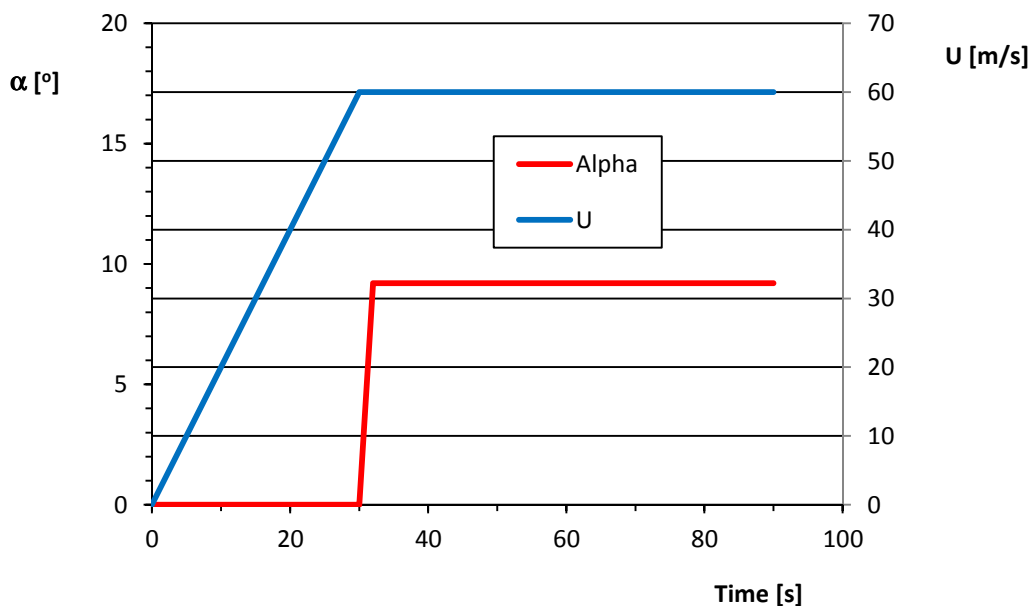


**Figure 10.** Variation of wind tunnel velocity  $U$  and model angle of attack  $\alpha$  during the simulated take-off sequence.

## 2.4 Sandpaper tests

The goal of the sandpaper measurements was to find a sandpaper roughness that gives the same effect as the Cold Soaked Fuel Frost with a dimensionless thickness of  $t/c=0,0005$ . This frost thickness gave a lift coefficient reduction of about 5,24%, the amount of which is accepted due to de/anti-icing treatment at take-off (ref. [10] Hill and Zierten, page 32).

In the former wind tunnel tests frost was formed on the wing tank area with typically glare ice forward of the front spar. Frost was also formed on the wing lower surface, but this is expected to have only a small effect when it does not exist far forward to affect the upper surface boundary layer. On an airfoil with a slat the effects are noticed only close to  $C_{Lmax}$  (ref. [11] Bragg et al, page 1377, 1378). Arteform was interested in varying the sandpaper at different positions on the wing lower surface as well as other experiments such as pressure belt measurements. After a couple of months a contract could be signed to study the topics of the customer.

The sandpaper was positioned on the wing model upper surface to cover the area with rough frost at about  $x/c=0.12$  to  $0.65$ . The sandpapers were installed as  $70 \times 450$  mm strips with adhesive backing as shown in Figure 11. The number of strips was 22 in the spanwise direction covering the entire upper surface except two narrow strips at the model support stations, see Figure 12. The sandpaper fore edge was positioned 30 mm aft of the slat trailing edge (Figure 13). The sandpaper was not applied on the model lower surface as the effect of frost on the lower surface is expected to be small

The sandpaper measurements were performed with three different roughness values, defined by ISO/FEPA grit numbers P40, P80 and P120. Sandpaper has a cardboard backing to which the grit is attached. Thus the grit roughness is smaller than the total thickness of the sandpaper. In this case the sandpaper was ordered with an adhesive tape to fix the paper on the wing which also adds to the total thickness  $t$ . The total thickness was measured with a micrometer and the thickness of the plastic sheet protecting the adhesive was subtracted from the result. Because the grit particles are embedded in the bonding material the actual roughness height is smaller than the average grain diameter  $k$ . The roughness height for sandpaper full of grit is typically half of the grain diameter (which is controlled by the sieve size). Looking in the photographs showing the sandpaper details (figures 13 to 19) it is obvious, that the sandpapers used contained empty spaces between the grit particles. Consequently the surface roughness was close to the grit size. The sandpaper configurations are summarized in Table 1.

The sandpaper fore end inevitably forms a step on the airfoil surface as shown in Figure 14. The possible effect of the step was studied with P40 sandpaper by placing a 15 mm wide P120 sandpaper strip in front of the fore end, see Figure 15. The P120 strip lifted off from the model surface during the tunnel run and for this reason the strip was secured with an aluminum tape (Figure 16). P80 sandpaper also lifted off from the model

**Table 1.** Investigated sandpaper configurations.

Configuration	t [mm]	k [mm]	t/c	k/c
Grit P40	1,180	0,425	0,00189	0,00068
Grit P80	0,550	0,201	0,00088	0,00032
Grit P120	0,410	0,125	0,00066	0,00020

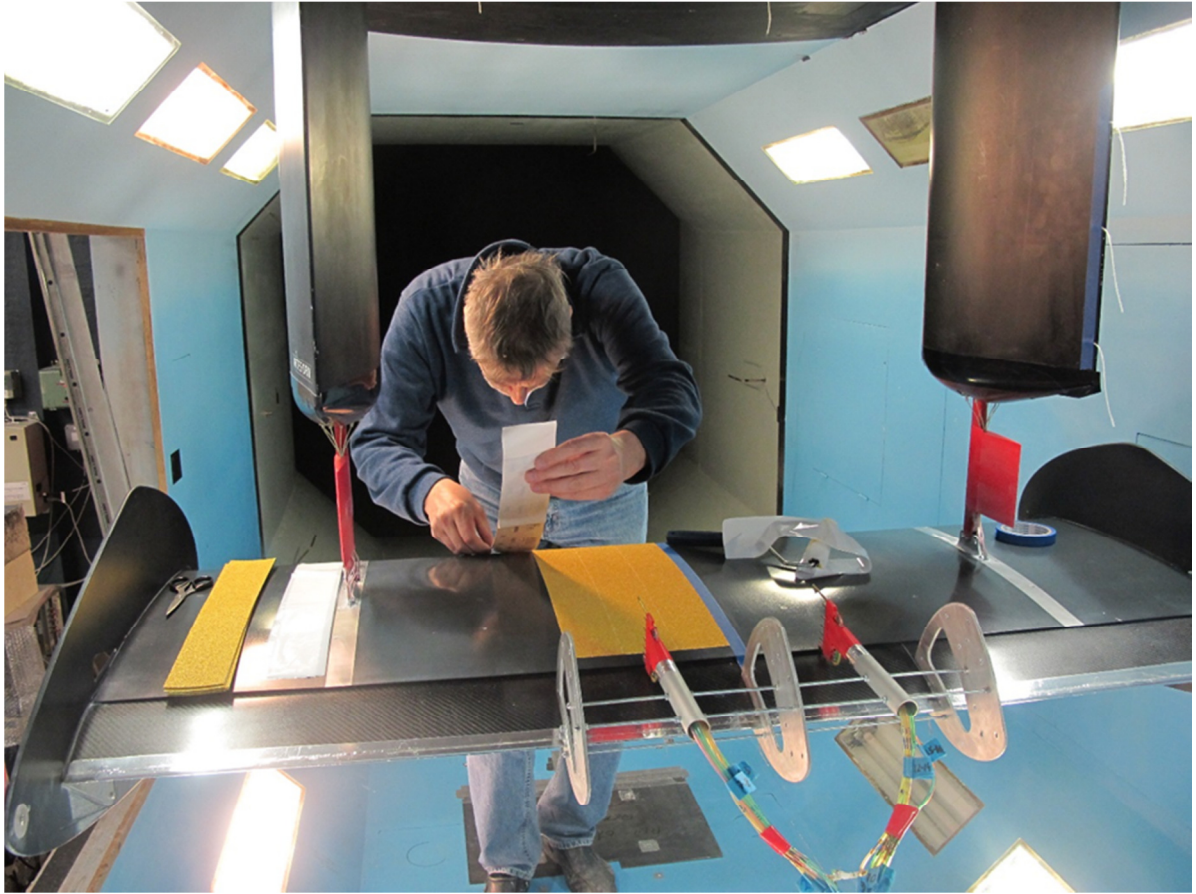


**Figure 11.** Installation of sandpapers.

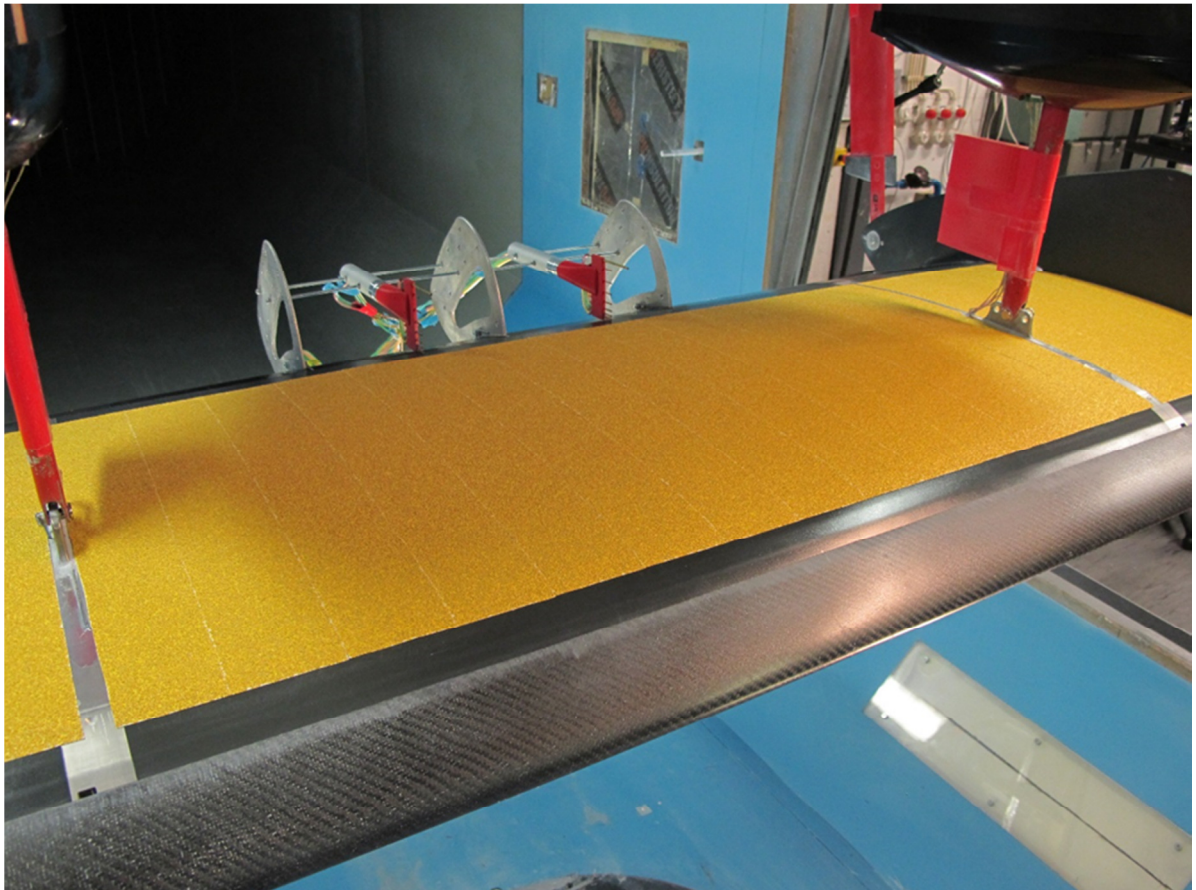


**Figure 12.** Overview of the wing model covered with P40 sandpaper.

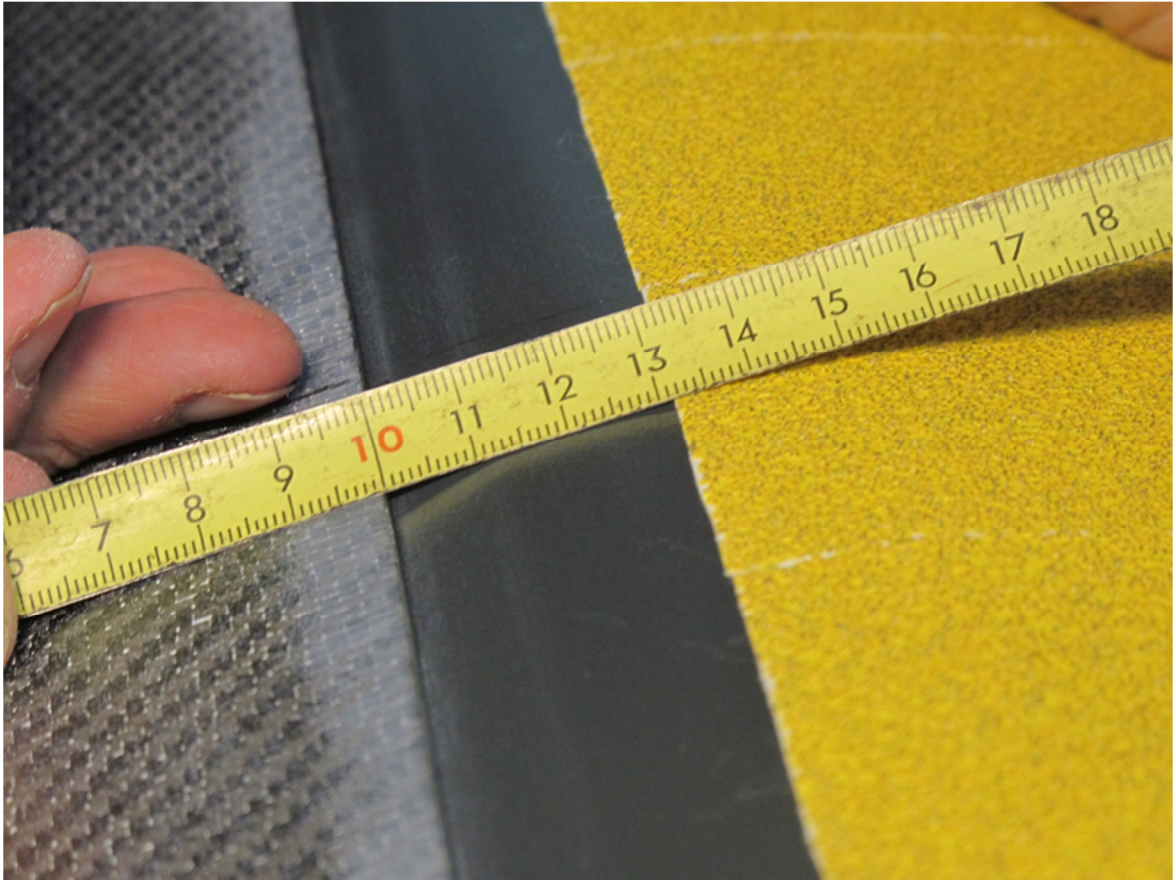


**Figure 13.** The gap between the slat and the sandpapers was about  $30\pm 1$  mm.

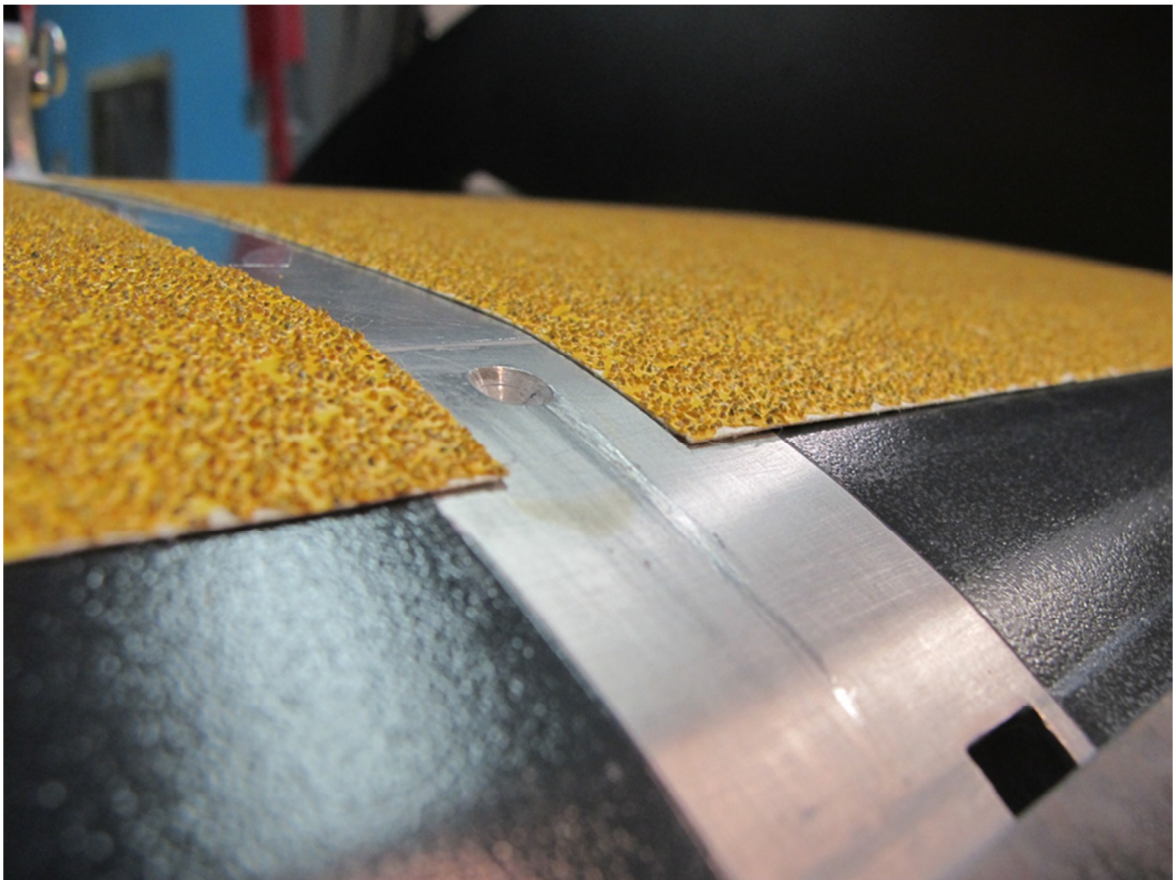


**Figure 14.** Close-up view of the wing leading edge area with the fore edge of the P40 sandpapers. Note the large grit/particle size.

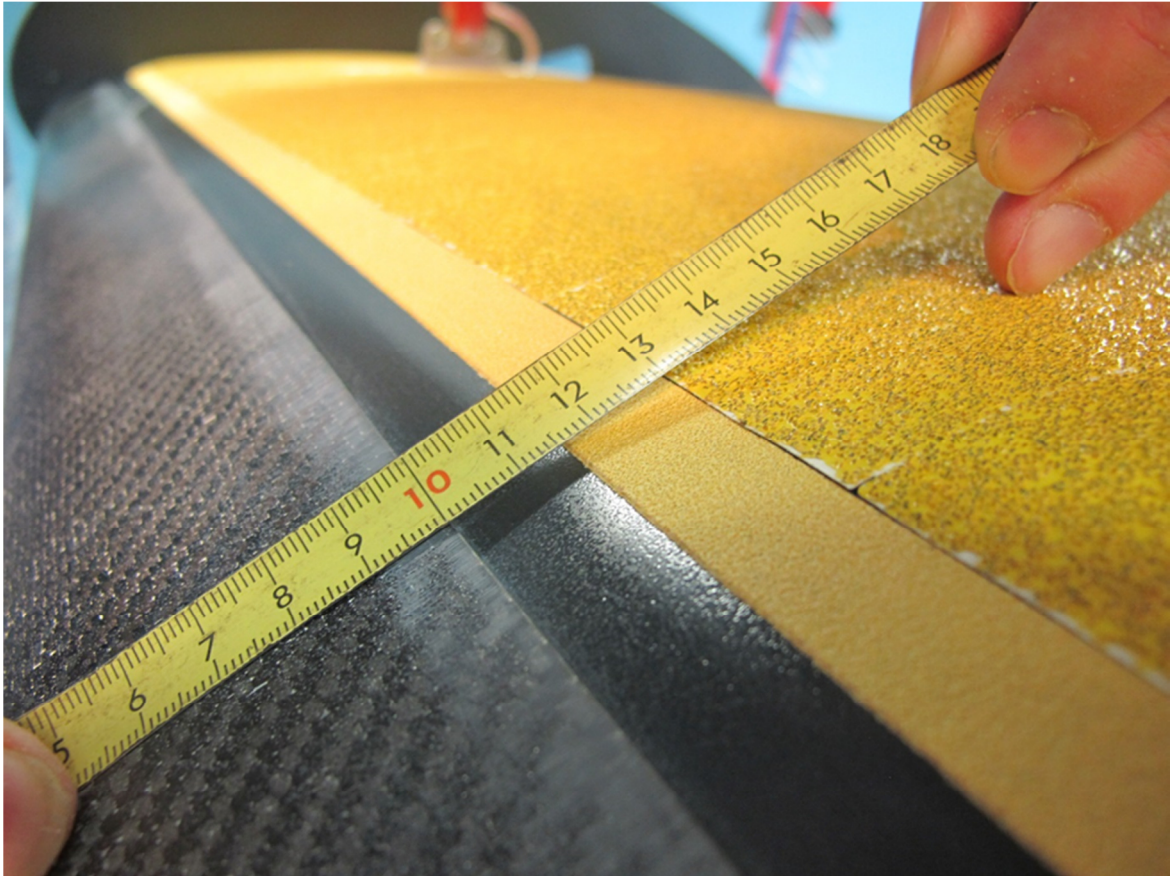


**Figure 15.** Narrow P120 sandpaper strip in front of the P40 sandpaper.

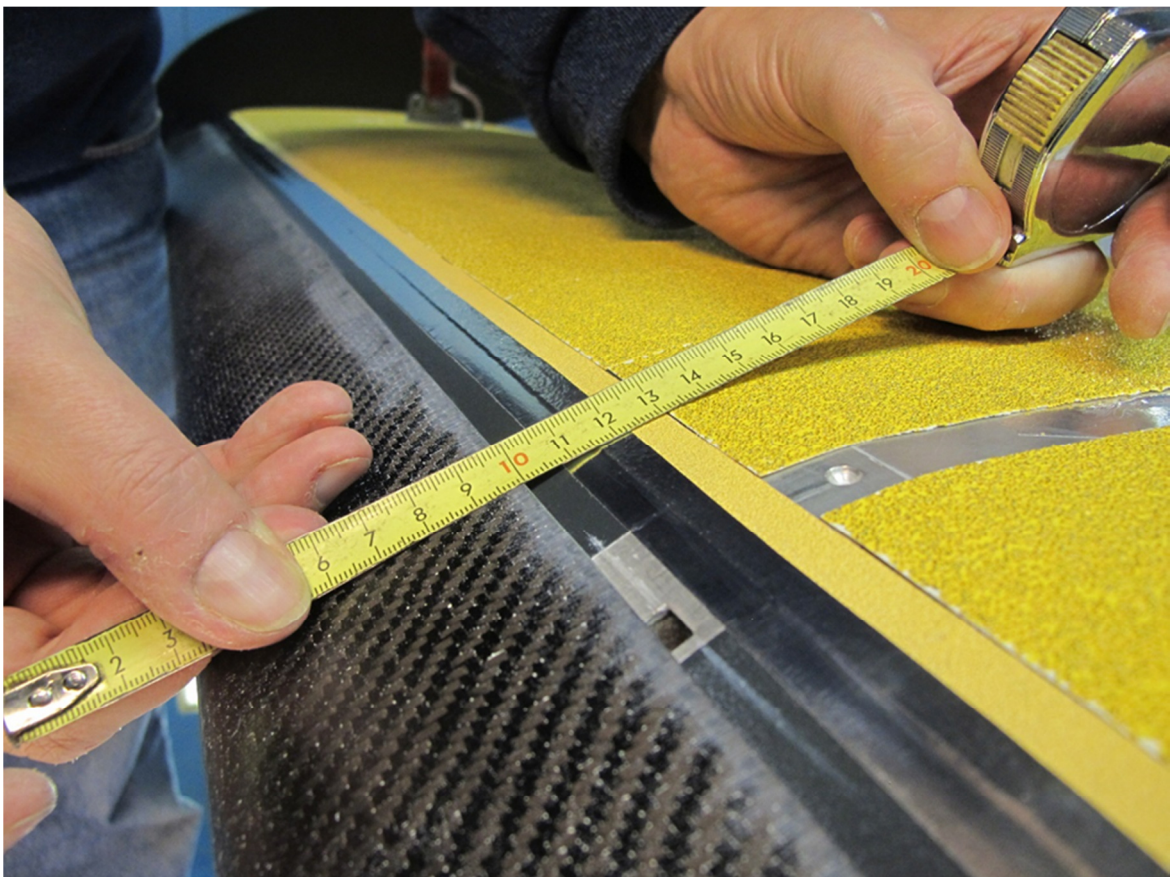


**Figure 16.** P120 sandpaper strip in front of the P40 sandpaper with additional aluminum tape to prevent the P120 strip from lifting off.

surface and was secured during the runs with aluminum tape. P40 sandpaper could be tested without the aluminum tape but the effect of the tape was also tested. The aluminum tapes at the fore edges of P40, P80 and P120 sandpapers are shown in Figure 17, Figure 18 and Figure 19.

The aerodynamic measurements consisted of the wing lift coefficient  $C_L$  and the corresponding boundary layer displacement thickness  $\delta^*$ . The lift coefficient was determined by measuring the wing lift force with the tunnel balance. The interesting time period is just after the take-off rotation when the CSFF has caused largest lift losses. However, with a sandpaper covered model the lift coefficient does not change when the model angle of attack is constant after the rotation. The boundary layer displacement thickness was measured at the aft end of the wing model main plane upper surface using two boundary layer rakes. The rakes were positioned in the spanwise direction symmetrically 120 mm from the wing model center line. The rake set up is shown in Figure 11 and Figure 12 and the rake tube locations in Figure 20.

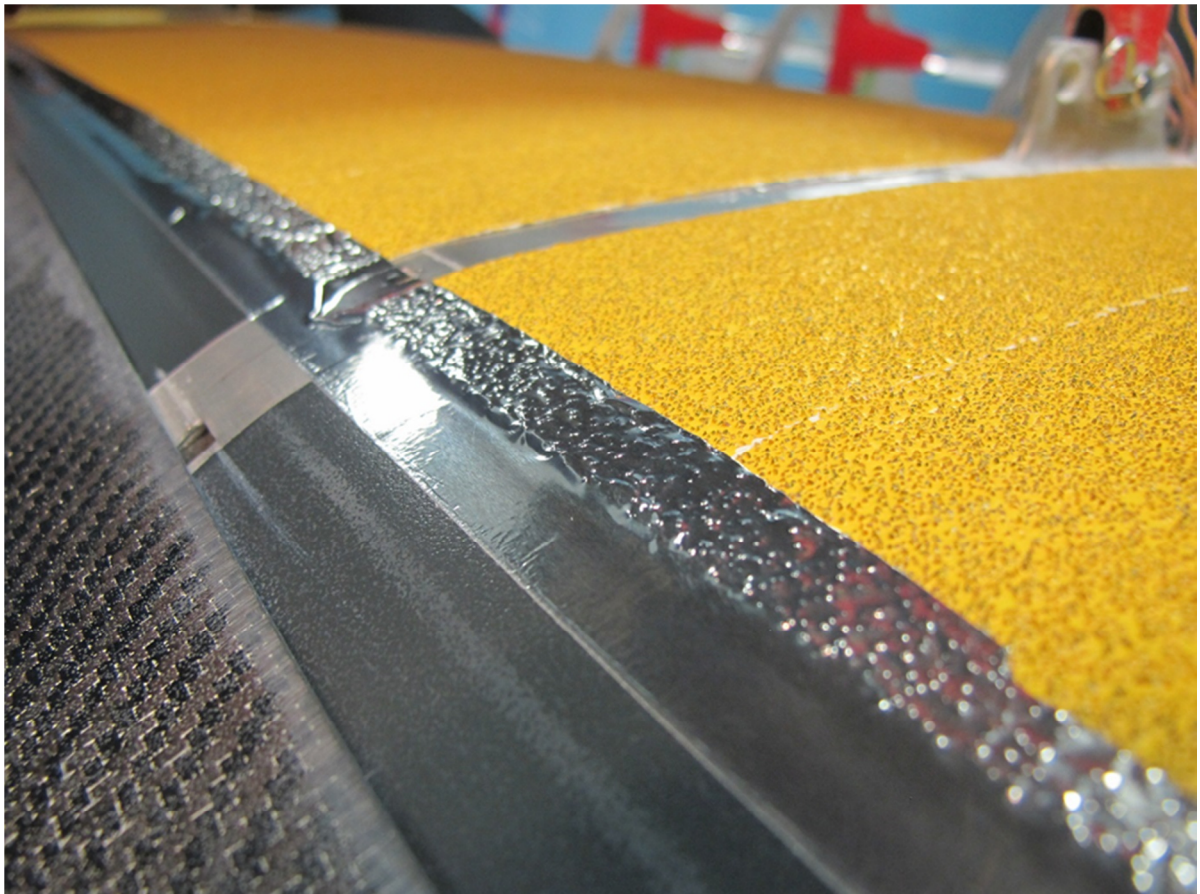


**Figure 17.** The P40 sandpaper fore edge of taped over with aluminum tape.

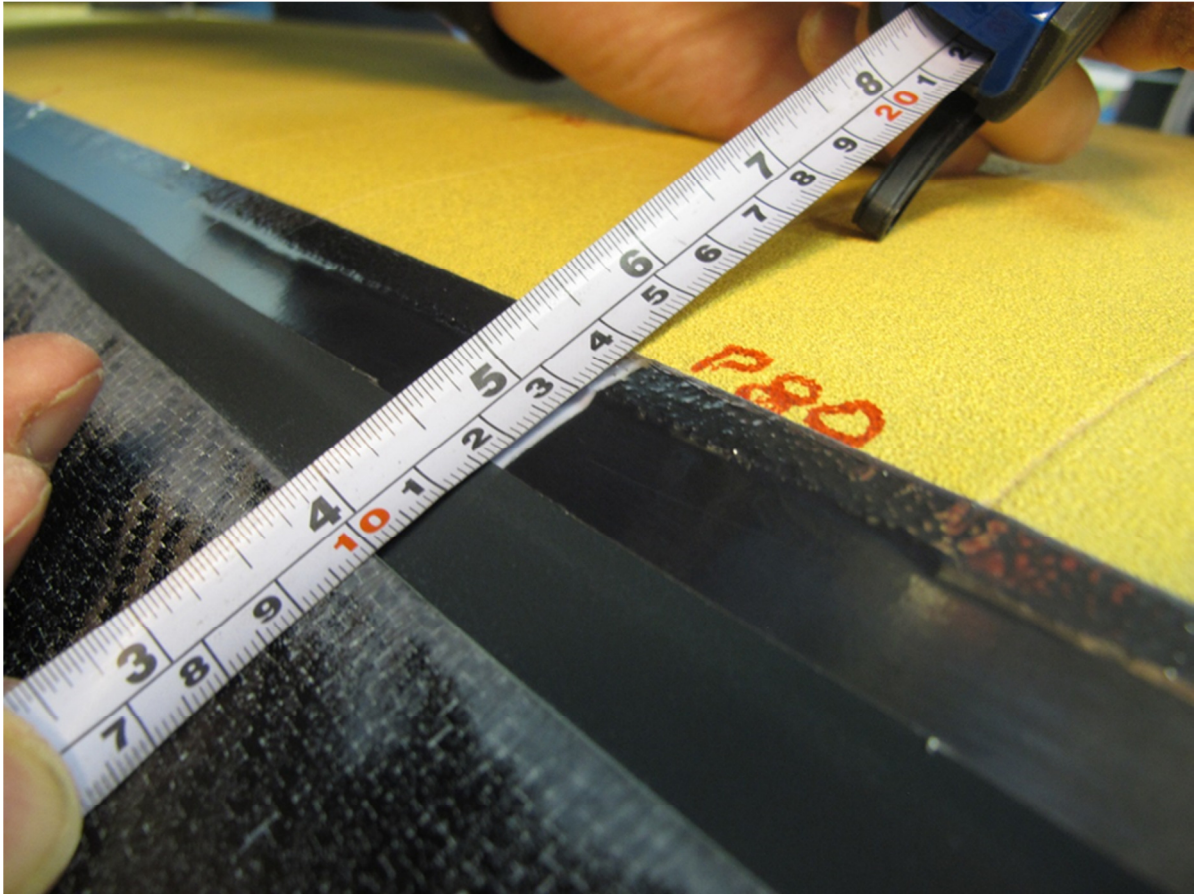


**Figure 18.** The P80 sandpaper fore edge taped over with aluminum tape.

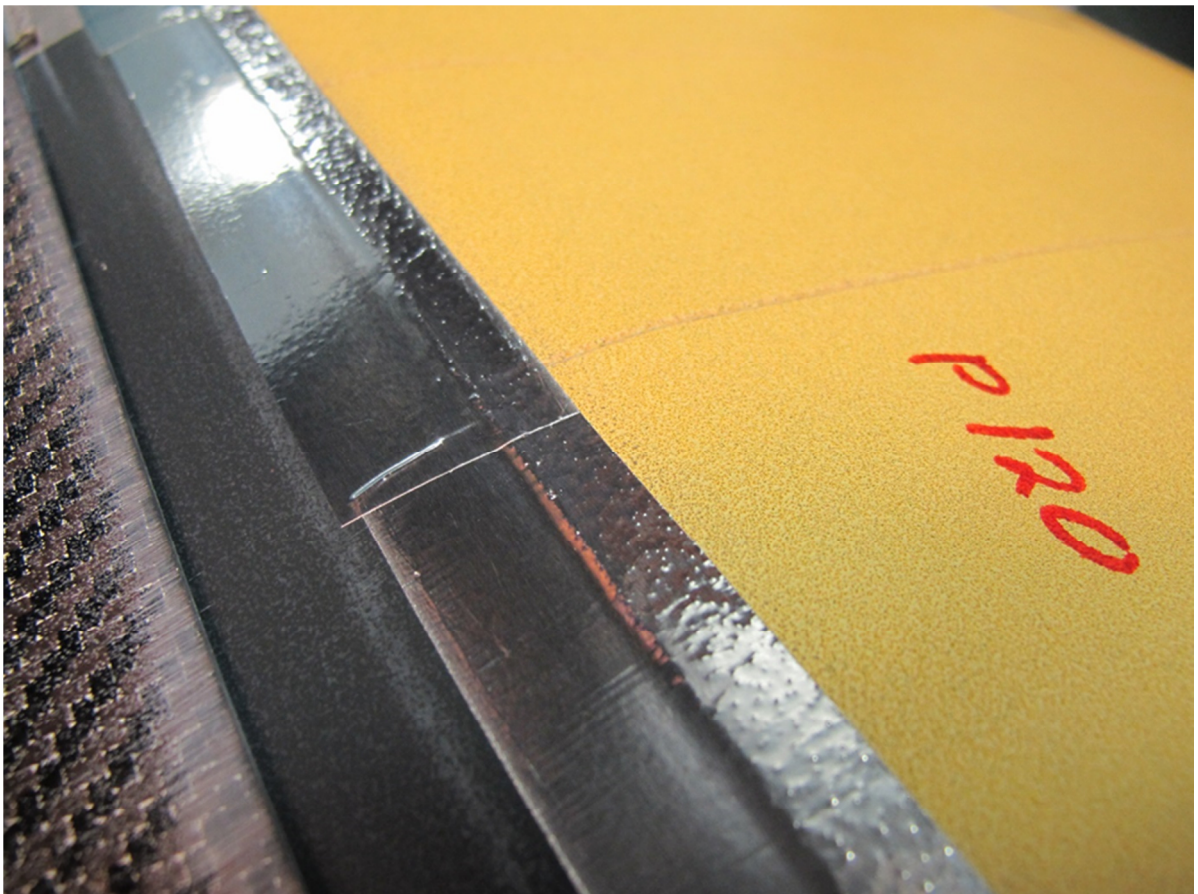


**Figure 19.** The P120 sandpaper fore edge taped over with aluminum tape.

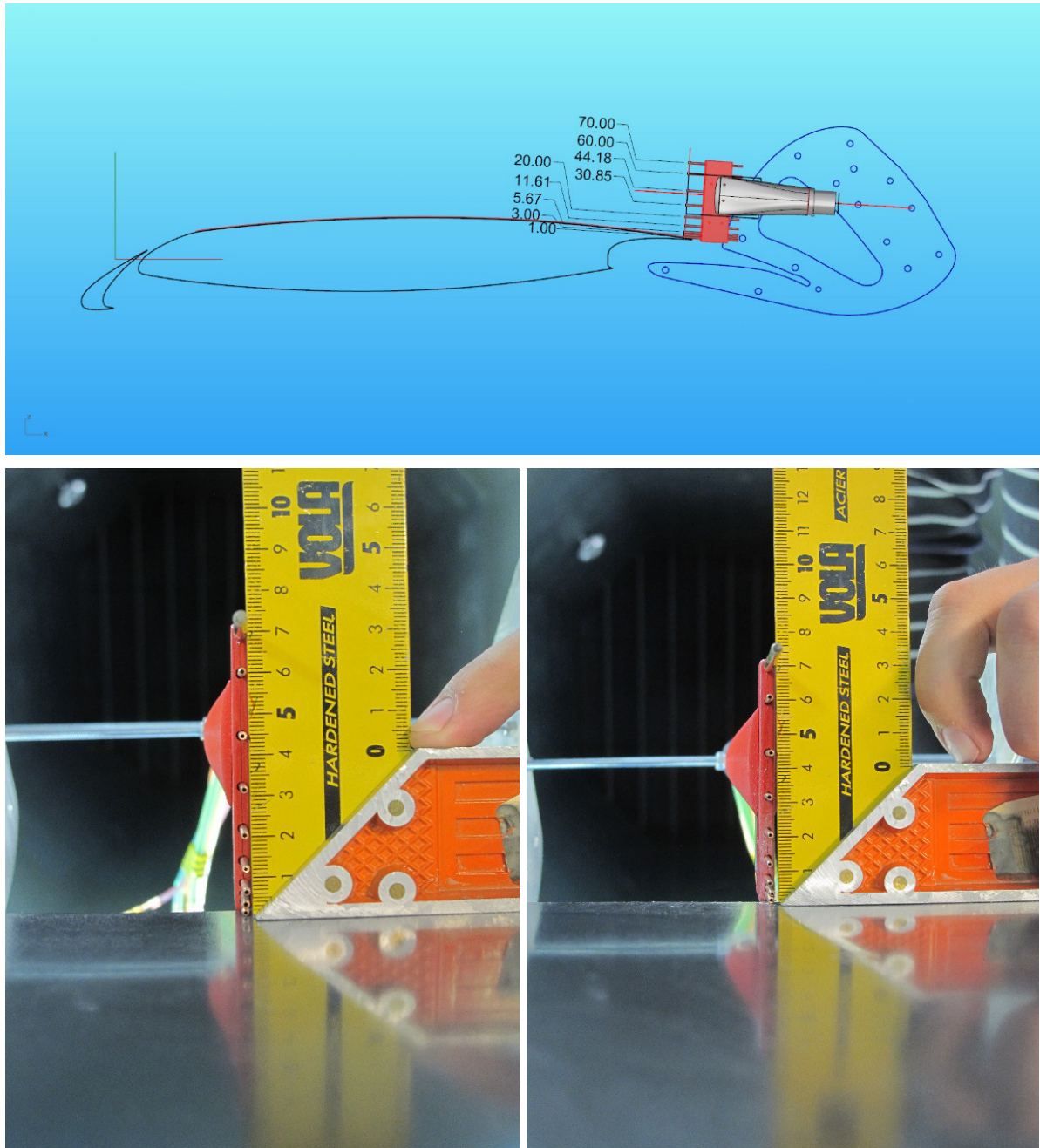


**Figure 20.** Rakes shown in their positions. The top most tube (70mm) is the static pressure tube. Being the most sensitive tube to incidence it defined the rake angle. All the others are total pressure tubes, which are not sensitive to local incidence. The left and right pictures show the rake tubes on the model left and right hand sides respectively (Kivekäs ref. [12]).

## 2.5 Anti-icing fluid tests

The goal of the anti-icing fluid measurements was to determine the typical lift loss and boundary layer thickening due to anti-icing fluid just after the take-off rotation. This would enable comparison of Cold Soaked Fuel Frost and sandpaper measurements with the fluids results. As the non-Newtonian type IV fluid was expected to produce the largest lift losses it was selected for the tests. The ambient temperature of about +5° C was good for the tests as the maximum viscosity of the used Type IV fluid appears around this temperature. Another test series was made with Type II fluid.

The anti-icing fluid was poured on the model before the test and checked that it covered the entire upper surface, see Figure 21 and Figure 22. The fluid layer thickness was measured with an Elcometer thickness gauge. The measured thicknesses were 1,5 mm and 1,2 mm for Type IV and II fluids respectively.

The aerodynamic measurements consisted of the wing lift coefficient  $C_L$  and the corresponding boundary layer displacement thickness  $\delta^*$ . The measurements were performed in the same way as for the sandpaper tests described in the previous chapter. In the first boundary layer measurements all total pressure tubes were on purpose unplugged. In the subsequent measurements the three tubes closest to the wing surface were plugged.

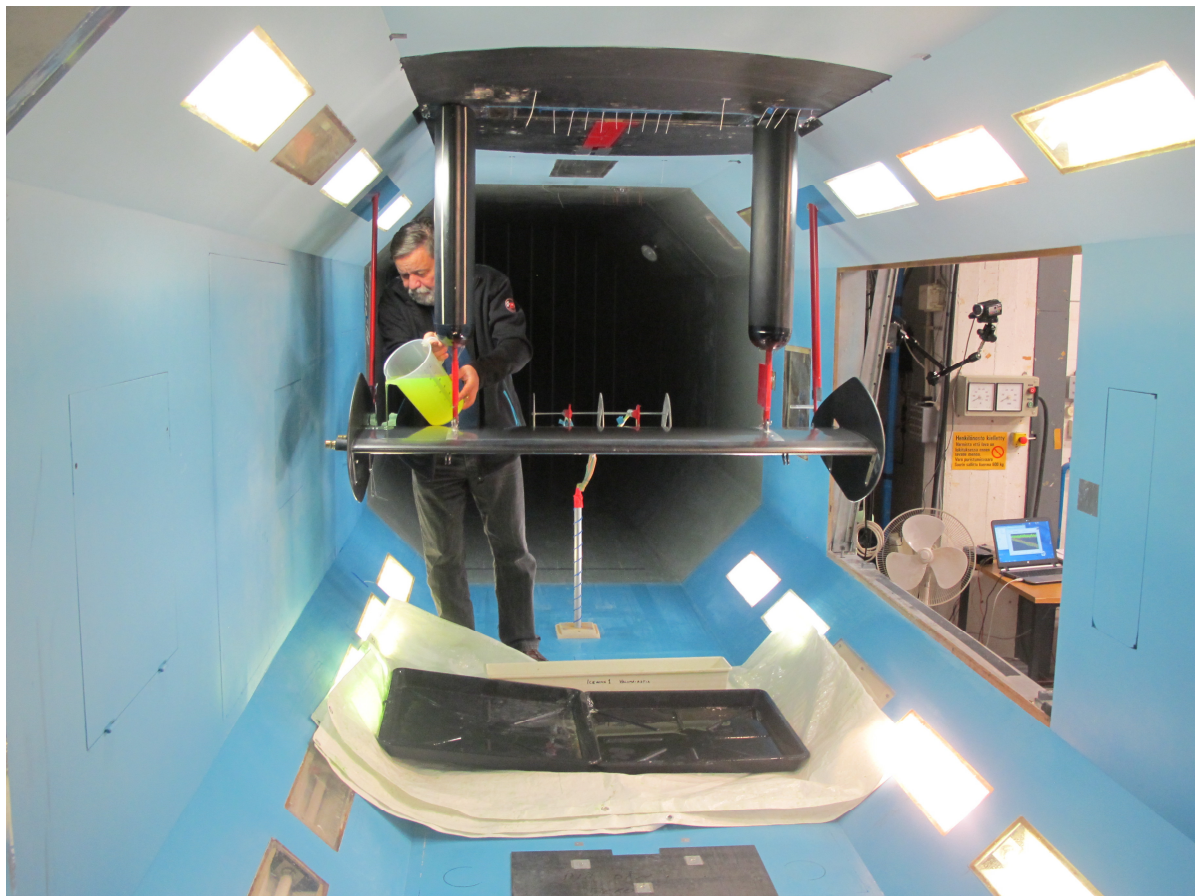


**Figure 21.** Applying anti-icing fluid on the wing model.

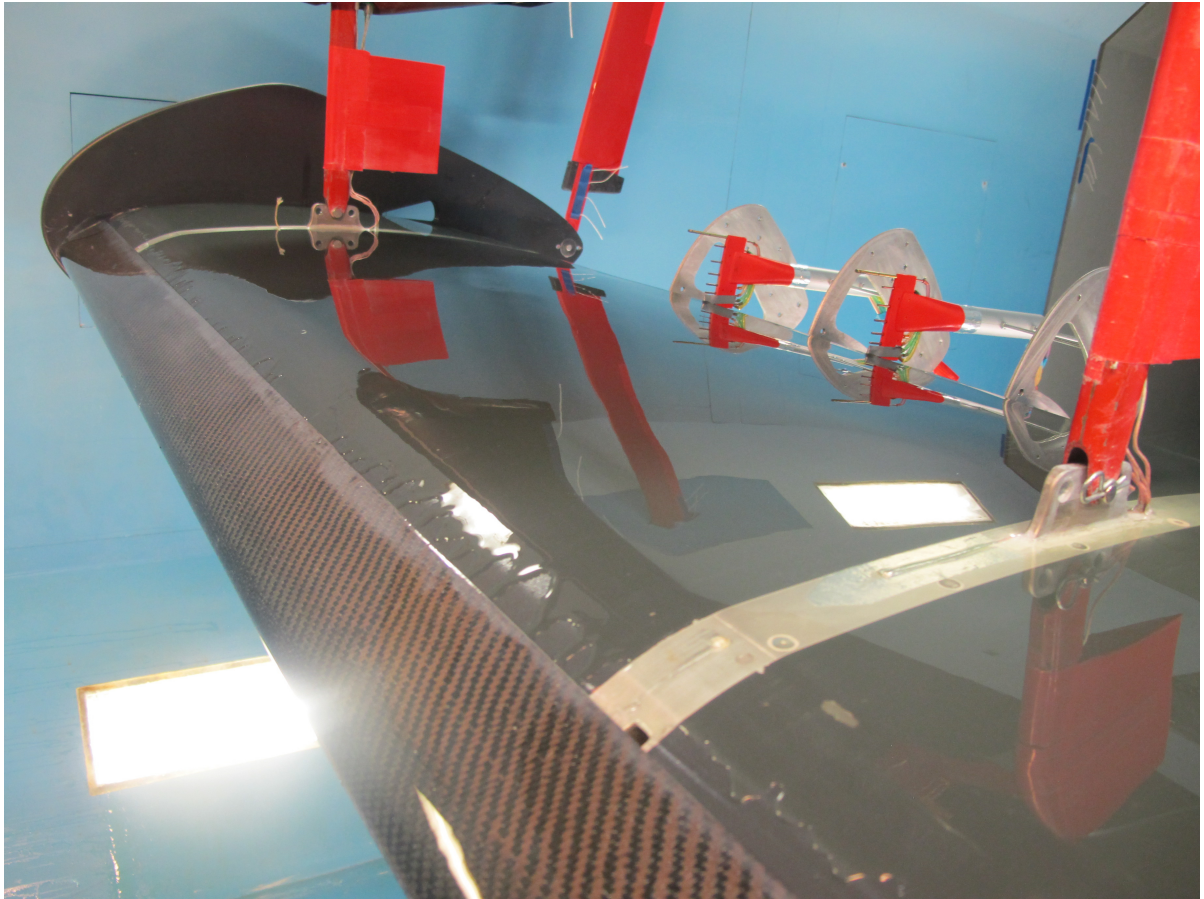


**Figure 22.** Type IV anti-icing fluid on the wing model.

## 2.6 Plastic sheet tests

The goal of the plastic sheet measurements was to investigate the effect of a smooth added thickness to separate the effects of the added surface thickness and roughness.

The PVC plastic sheet was positioned on the wing model upper surface to cover the same area as with the sandpapers, about  $x/c=0.12$  to  $0.65$ . The sheets were installed with double-sided tape. The tape is visible through the transparent PVC film in Figure 23. The orange strip under the PVC sheet fore edge is an especially easy to release double-sided tape. Above this an especially strong Scotch tape was used under the PVC plastic sheet. The total thickness of the tapes and the PVC plastic sheet was  $1,28$  mm in this area. The fore edge attachment was secured with an aluminum tape on top of the PVC sheet in the same way as on the sandpapers, as shown in Figure 24. Further downstream a transparent easy to release Scotch tape was used under the PVC sheet. The total thickness in the downstream area was  $0,98$  mm. The PVC sheets covered the entire upper surface except two narrow strips at the model support stations, see Figure 25. The PVC sheet fore edge was positioned  $30$  mm aft of the slat trailing edge. The PVC sheet aft edge was positioned in front of the boundary layer rake tubes in the same way as with the sandpapers, see Figure 26. No aluminum tape was used here. The PVC sheet was not applied on the model lower surface, which was also the method in in the sandpaper tests. The total thickness of the PVC sheet and the double sided tapes was measured with a micrometer. The PVC sheet configuration is summarized in Table 2.

The PVC plastic sheet fore end inevitably forms a step on the airfoil surface. The step height at fore edge consisted of the PVC plastic sheet, the orange tape and the especially strong Scotch tape. The aluminum tape exists upstream and downstream of the step and does not contribute to the step height. Further downstream the added thickness is smaller consisting of the PVC sheet and only the easy to release Scotch tape. There was no step between the two regions because the strong Scotch tape was of gel type and could be shaped to form a successive ramp. It is unknown why Arteform wanted to use an especially strong tape on top of the especially easy to release tape. The strong tape does not strengthen the bonding of the PVC sheet to the wing surface with a weak link in between. However, this is the configuration that was tested. The aerodynamically significant thickness is the one at the fore edge.

The aerodynamic measurements consisted of the wing lift coefficient  $C_L$  and the corresponding boundary layer displacement thickness  $\delta^*$ . The lift coefficient was determined by measuring the wing lift force with the tunnel balance. The interesting time period is just after the take-off rotation when the CSFF has caused largest lift losses. However, with a PVC sheet covered model the lift coefficient does not change when the model angle of attack is constant after the rotation. The boundary layer displacement thickness was measured at the aft end of the main wing upper surface using the two boundary layer rakes.

**Table 2.** Investigated PVC sheet configuration.

Configuration	t [mm]	k [mm]	t/c	k/c
PVC plastic sheet	1,280	0	0,00205	0



**Figure 23.** Overview of the wing model covered with PVC plastic sheet.



**Figure 24.** Installation of aluminum tape over the PVC plastic sheet fore edge.

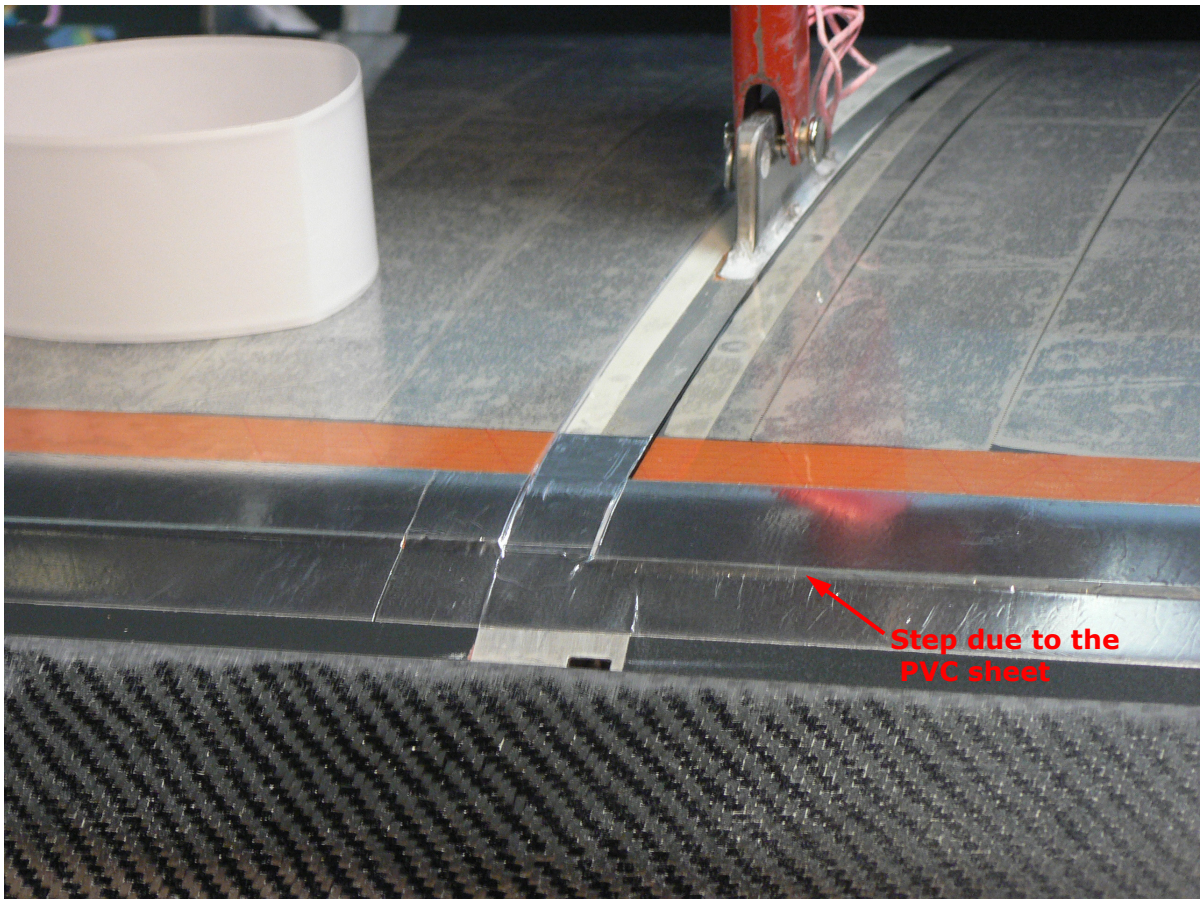


**Figure 25.** The PVC plastic sheet fore edge taped over with aluminum tape.

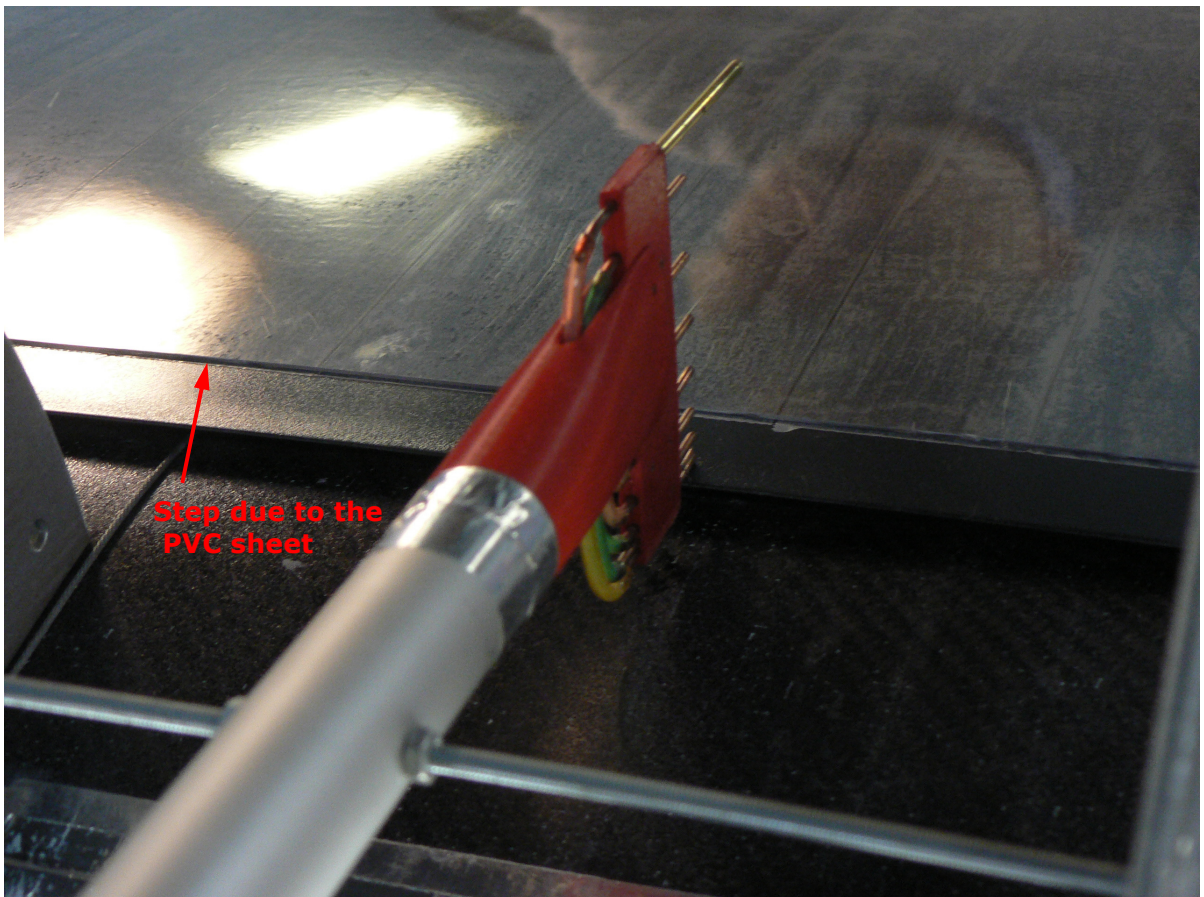


**Figure 26.** The PVC plastic sheet aft edge step.

### 3 Test results

#### 3.1 Performed wind tunnel runs

The oil-flow wind tunnel test runs were performed in October, the sandpaper tests during three days in November and the anti-icing fluids tests during two days in November 2017. At a later stage complementary plastic sheet tests were performed with a smooth PVC sheet in October 2018. In all wind tunnel tests the slat deflection of the HL-CRM Mod wing model was  $22^\circ$  and the flap deflection  $10^\circ$ . A more detailed description of the performed wind tunnel runs will be presented in the respective chapters of the test results.

#### 3.2 Oil-flow studies

In the case of a wing-body or wing-end plate junction the flow experiences the wing as an obstacle and is strongly retarded upstream of the wing resulting in a flow separation on the body or end plate surface. The flow is then accelerated above and below the airfoil nose part of the wing. Above and below the wing aft part the flow is retarded and experiences an adverse pressure gradient and a risk for separation. The following description of flow phenomena is based on the critical-point theory and measurements presented by Delery ref. [13], Simpson ref. [14] and Kegerise&Neuhart ref. [9].

The trajectories of the flow show on the vertical surface skin friction lines where a topological saddle point is typically formed, see Figure 27 a). At the saddle point the downstream continuing skin friction line meets an up stream flowing skin friction line and the flow velocity is zero at the saddle point thus being a stagnation point. There are two transversal out flowing skin friction lines showing that the flow continues up and down to pass around the wing. These skin friction lines form a separation line as aft of this line there is reversed flow. Between the wing nose and the separation line there may be visible a line of low shear which may merge further downstream with the separation line. The line of low shear is not a separation line but a line where the shear stress on the surface is minimized and oil-flow pigment accumulates.

Figure 27 b) depicts a section of the flow on a horizontal surface in front of the wing leading edge showing reversed flow and a separation bubble. In a three dimensional flow separation the streamlines do not have to remain in the surface but may turn out of the plane either up or down. The separation bubble initiates a rolling up of a vortex sheet which forms a horseshoe type primary vortex around the wing leading edge at the junction of the wing and the end plate, see Figure 27 c). The horseshoe vortex induces a vortical flow scrubbing the end plate between the low shear line and the wing leading edge manifesting in loss of oil-flow pigment. There may be a counter rotating secondary vortex and multiple vortices. The vortices are unsteady and may merge with the primary horseshoe vortex. Because vortex filaments are more susceptible to unsteady meandering in the presence of adverse pressure gradients one may expect that this happens around the downstream part of the wing. Further downstream at the airfoil aft part the flow may separate on the suction side of the wing trailing edge at the corner of the wing and end plate at high angle of attack. This separation is due to the local pressure increase at high angle attack which the boundary layer cannot withstand.

The present oil-flow tests were performed with a slat deflection of  $22^\circ$  and a flap deflection of  $10^\circ$  at an angle of attack  $9,2^\circ$  used in the take-off rotation tests. A mixture of 5 g of titanium dioxide and 250 ml of lamp oil was utilized in the tests. Due to the tendency of the oil-flow mixture to evaporate and dry prematurely the tunnel speed was accelerated to 30 m/s instead of the 60 m/s used in the take-off rotation tests. The corres-

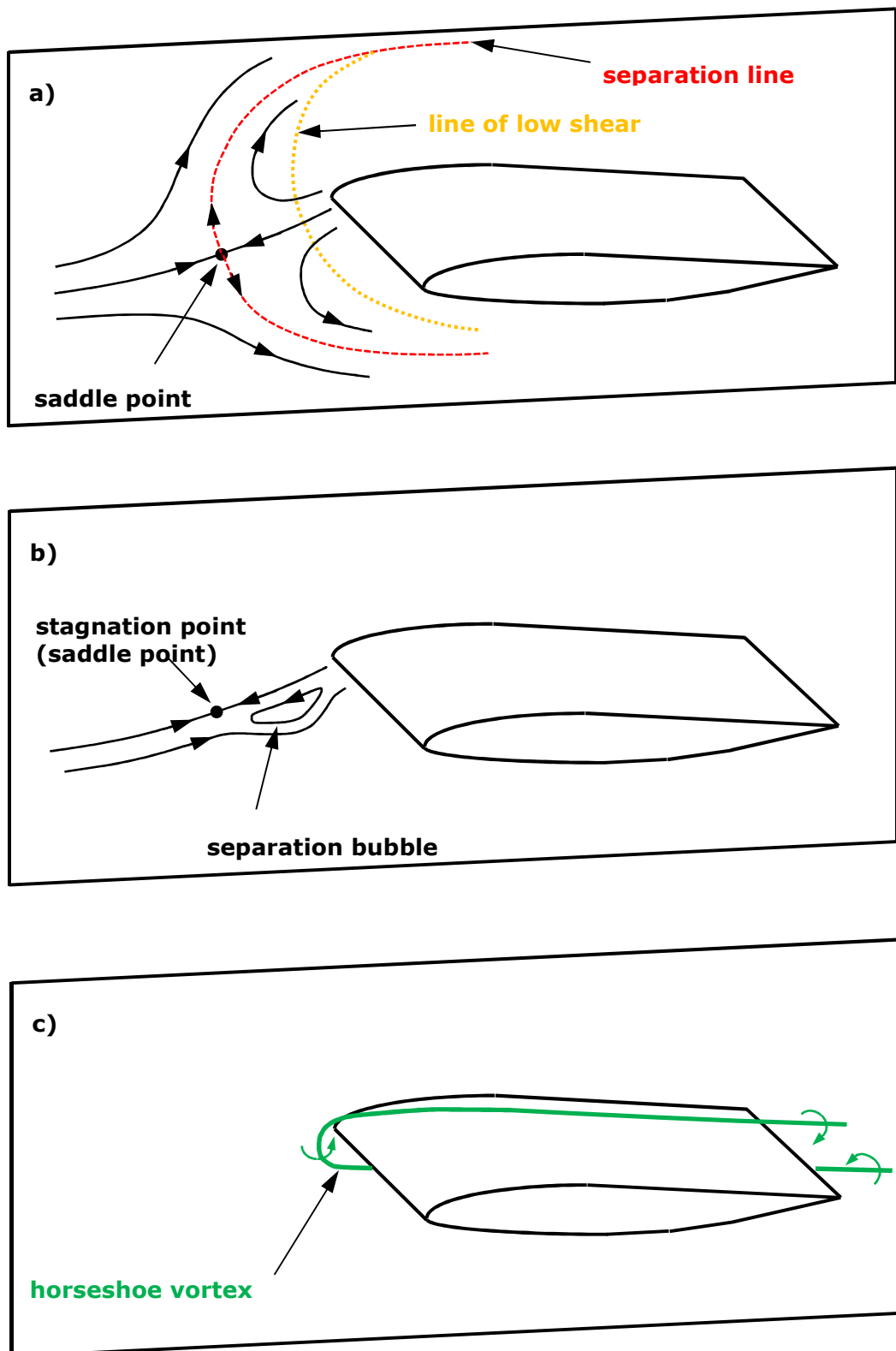


**Figure 27.** Wing-end plate junction flow with a) skin friction lines on the vertical surface, b) streamlines on a horizontal surface and c) formation of a horseshoe vortex.

ponding model Reynolds number was reduced approximately to 1,3 million from the nominal 2,5 million. This is not considered a problem as the risk for flow separation is higher at a lower Reynolds number and the tests are conservative if no separation appears. This generally known tendency was confirmed on page 22 of ref. [9] as oil-flow tests were performed at model Reynolds numbers of 0,62 million and 2,4 million. It is noted on page 21 of ref. [9] that quantitative comparisons with surface-flow visualizations are not generally warranted. For this reason only a qualitative analysis will be performed on the present oil-flow tests.

The present test configuration differs from the previously described generic wing-body configuration as there is a slat at the wing leading edge and a slotted flap at the trailing edge. No trip wire was used in the vicinity of the leading edge in the present tests. The end plate is also relatively short extending only marginally upstream of the slat leading edge. For this reason the separation line and the low shear lines probably will not be visible on the end plate. However, the horseshoe vortex is expected to be created due to the disturbance and will affect the flow on the airfoil critical aft part where the adverse pressure gradient prevails.

An overview of the flow in the junction of the wing upper surface and the end plate is shown in Figure 28 and Figure 29. Above the slat on the end plate there is visible an area of very little titanium dioxide indicating an area where the horseshoe vortex has scrubbed the end plate surface. Further downstream slightly above the junction corner a narrow band of scrubbed area continues indicating the presence of the vortex. Even further downstream the scrubbed area is more visible on the wing upper surface. Upstream of the flap there is the hole on the end plate and the flow emerging from the hole is visible. Downstream of the wing model strut is shown a conical wake area with disturbed turbulent flow.

Figure 30 shows the flow pattern more in detail on the model nose area. Aft of the slat slot there are two other low pigment areas, one in the corner of the end plate junction and the other one on the wing upper surface. The low pigment areas seem to indicate jets or disturbances emerging from the slat slot. The outboard disturbance seems to merge with the horseshoe vortex.

Figure 31 shows a close up view of the end plate hole. Upstream of the hole is a small hole leaking air from the outboard side of the end plate where the pressure is higher. This small flow and the larger flow through the bigger end plate hole form visible stream tubes with increasing widths. Aft of the larger hole there is a low pigment area indicating a flow separation on the end plate surface aft of the hole corner creating a very turbulent flow. There is no sign of flow separation on the flap or the wing upper surface, but there are three streaks of low pigment. One starts from the upstream end of the conical end plate hole. The second one is inboard of the first one and the third somewhat further inboard. The conical hole end may cause a disturbance or vortex which scrubs the wing surface. The second low pigment streak may be due to the horseshoe vortex which is pushed more inboard due to the flow through the end plate hole. The third low pigment area is probably not due to a counter rotating vortex as it is situated some distance inboard of the second one. There is also a low pigment area upstream of the third streak downstream of the slat slot. The cause is unknown but the area is not aft of the slat track bracket.

The width of the stream tube emanating from the end plate hole is indicated in Figure 32. The flow pattern outboard of the left end plate is shown in Figure 33. The flow is mostly attached with wedge shaped disturbances due to nuts etc.

The last photograph in Figure 34 visualizes the flow with tufts. It is seen that the tufts indicate attached flow on the inboard side of the end plate except aft of the hole. Note that the long tufts indicate a turbulent flow in the wake of the strut to which they are attached, not on the end plate surface. The tufts on the wing upper surface confirm that there is no noticeable flow separation.

The oil-flow tests at  $Re=1,3 \cdot 10^6$  show that on a clean airfoil there is no flow separation at the high angle of attack  $\alpha=9,2^\circ$  on the airfoil aft part where the critical adverse pressure

gradient prevails. Hence there will not be flow separation either at the higher Reynolds number  $Re=2,5 \cdot 10^6$ , used in the take-off rotation tests. The performed tests do not directly cover the situation when the wing upper surface is contaminated (for example with frost, anti-icing fluid or sandpaper). However, the end plate hole functions in the same way also with contaminated wing surface as the higher pressure outboard of the end plate enforces a flow through the hole. Consequently it is likely, that even with a contaminated surface there will not be flow separation in the wing-end plate junction on the aft part of the airfoil upper surface.



**Figure 28.** Overview of the oil flow pattern on the HL-CRM Mod wing model at  $Re=1,3$  million.

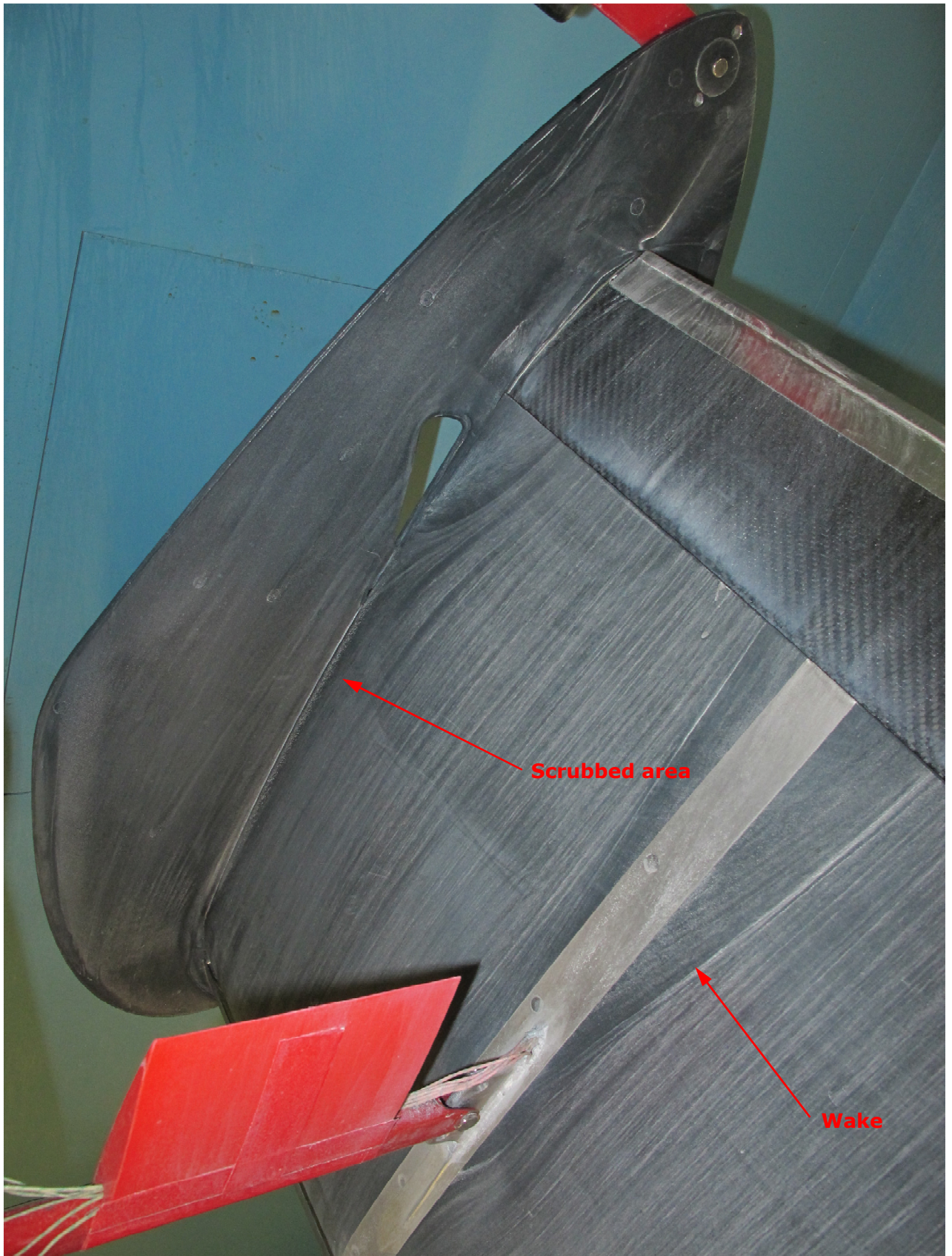


**Figure 29.** Overview of the oil-flow pattern on the HL-CRM Mod wing model at  $Re=1,3$  million.

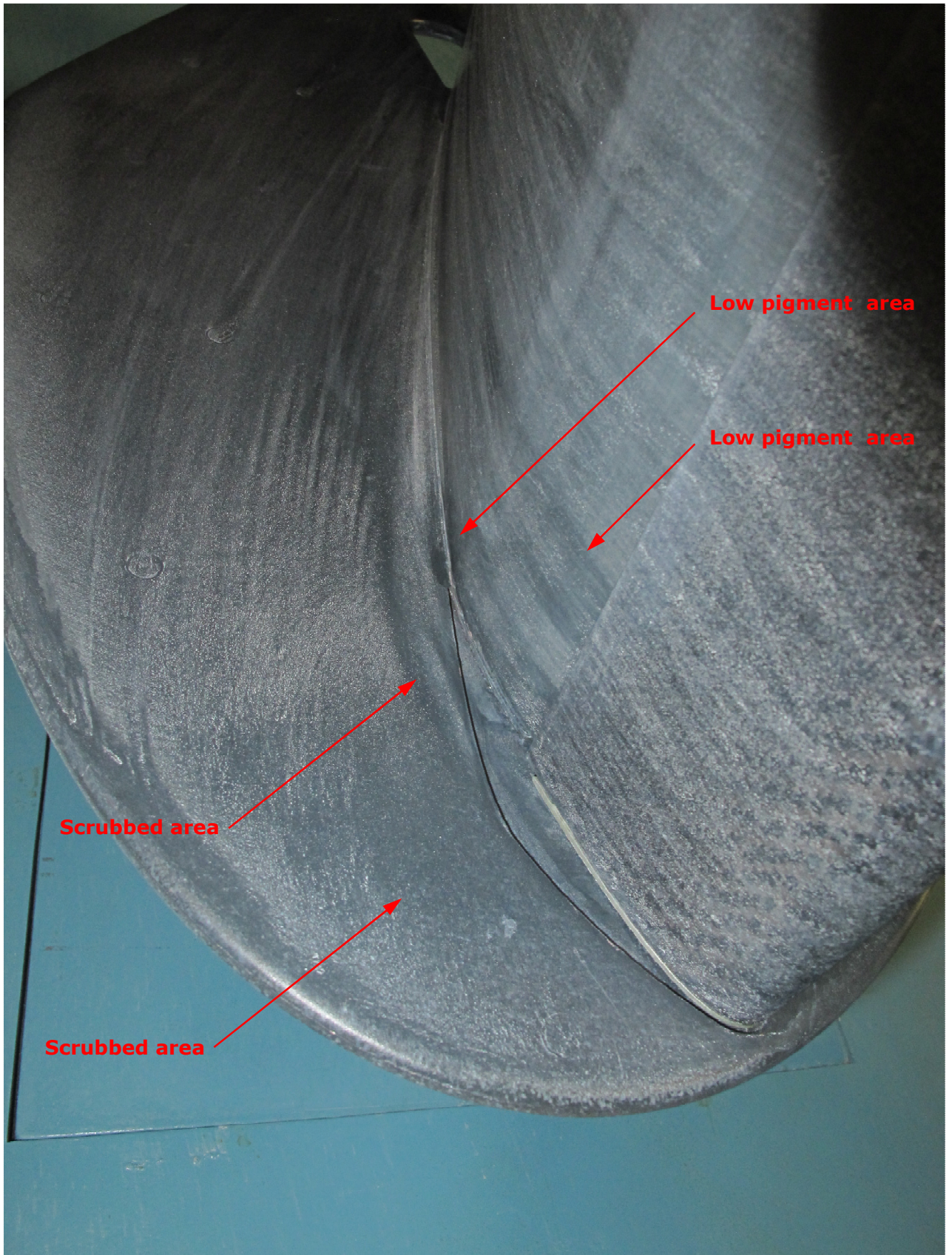


**Figure 30.** Oil flow pattern on the nose area of the HL-CRM Mod wing model at  $Re=1,3$  million.

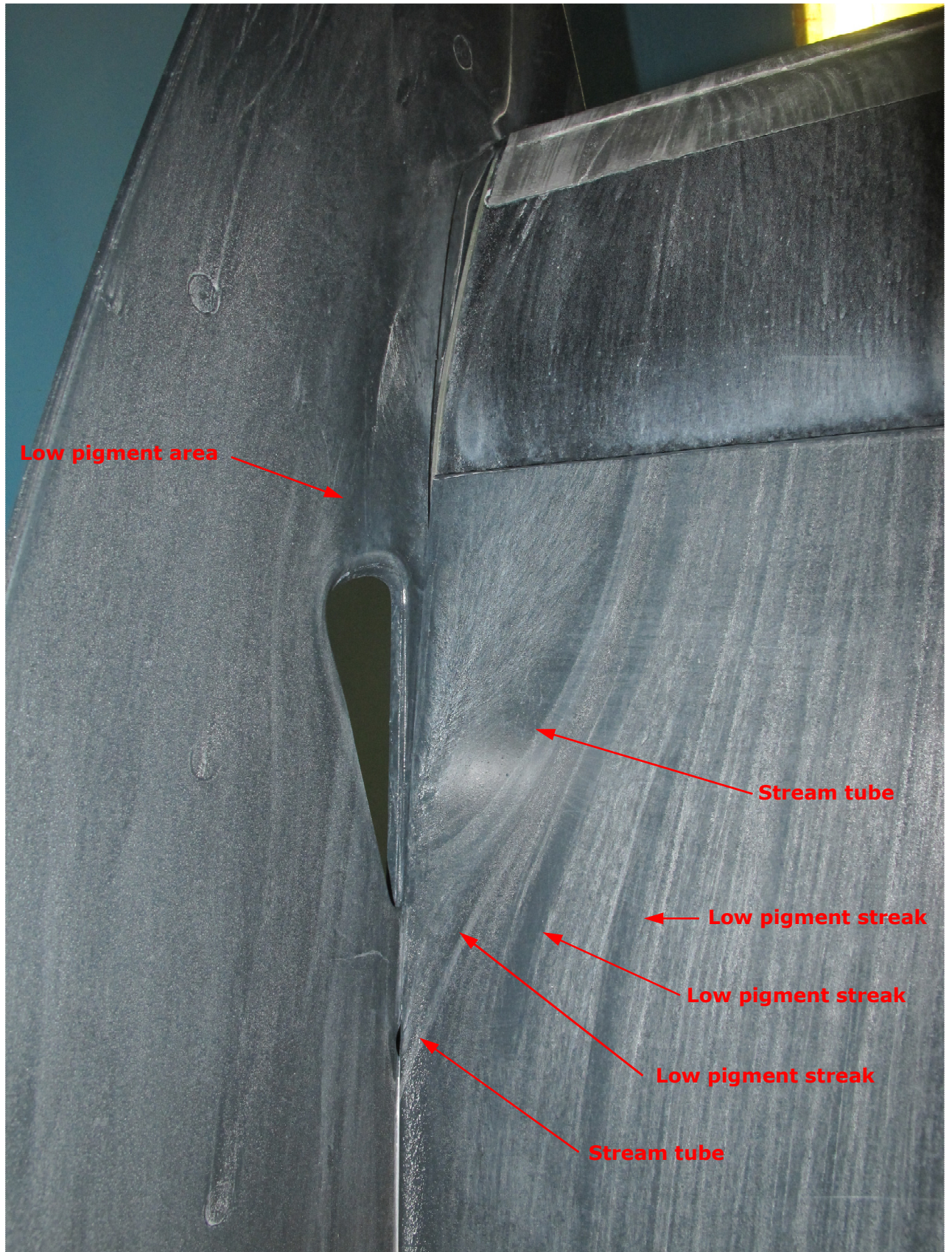


**Figure 31.** Oil flow pattern on the aft area of the HL-CRM Mod wing model at  $Re=1,3$  million.

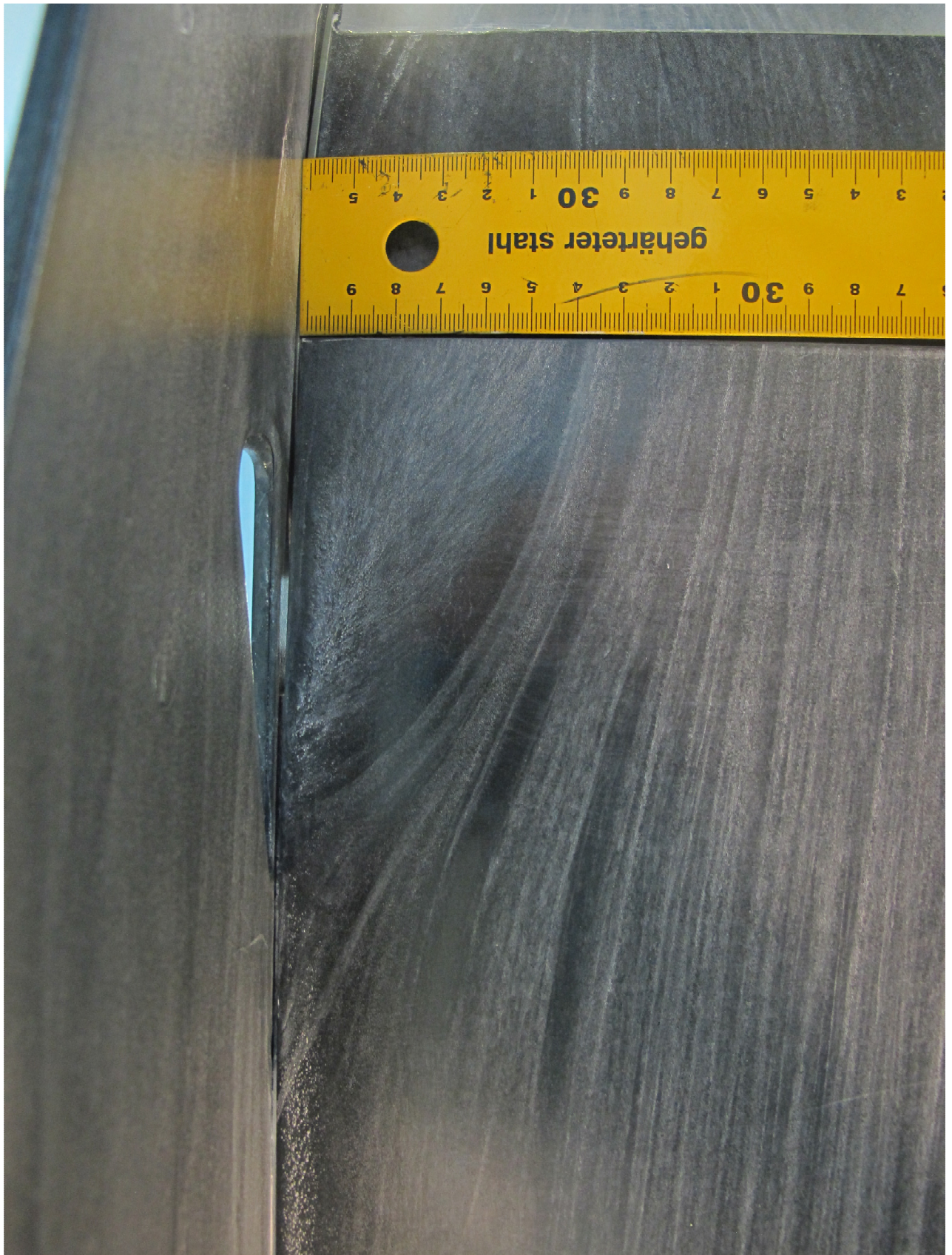


**Figure 32.** Oil flow pattern on the aft area of the HL-CRM Mod wing model at  $Re=1,3$  million. The ruler scale is 1 cm.



**Figure 33.** Oil flow pattern on the end plate of the HL-CRM Mod wing model at  $Re=1,3$  million.

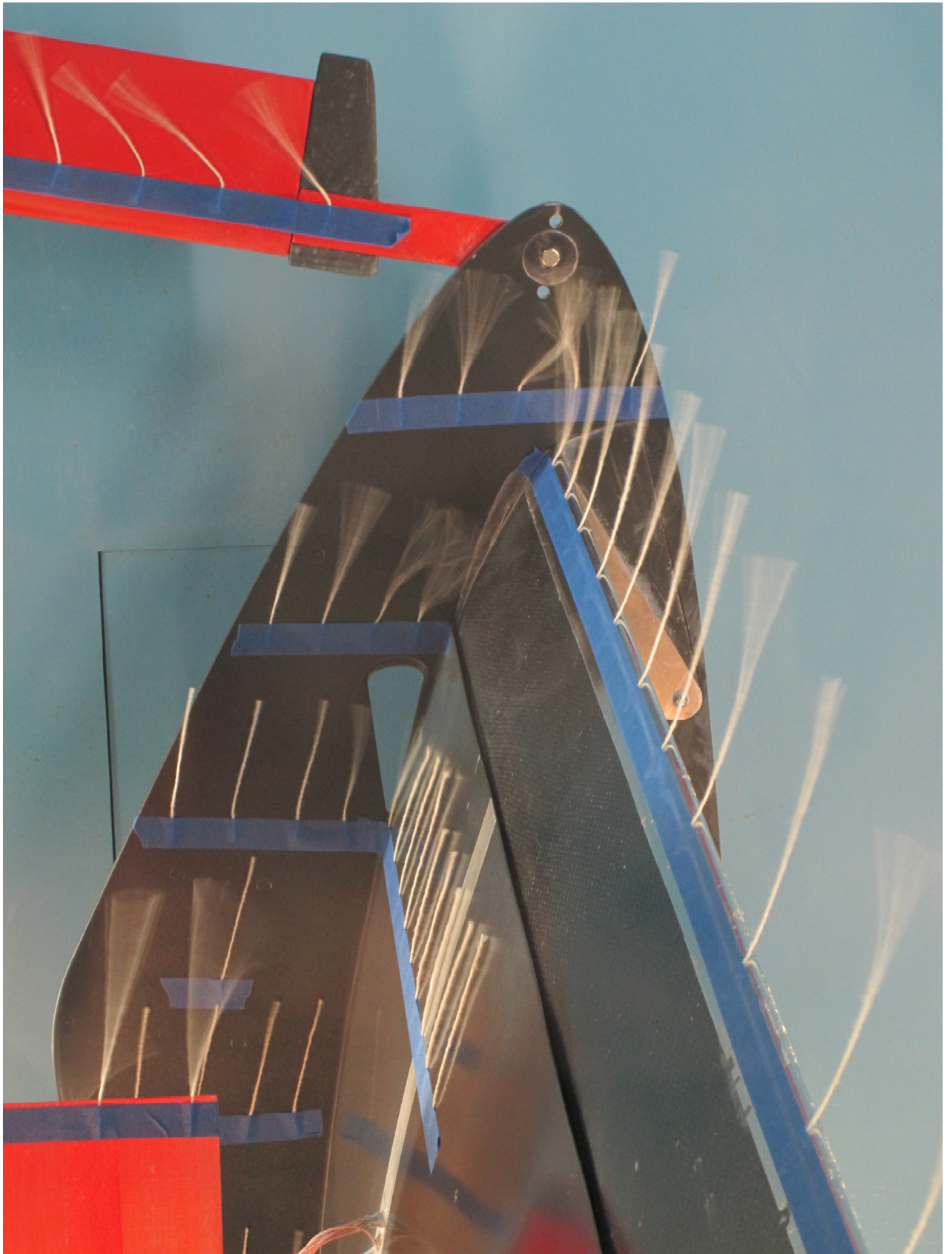


**Figure 34.** Overview of the flow pattern, visualized with tufts, on the HL-CRM Mod wing model at  $Re=1,3$  million.

### 3.3 Measurement accuracy in the 2017 tests

During the wind tunnel measurements in the autumn of 2017 the Arteform staff noticed that after the model rotation the angle of attack display flicked between two values namely  $6,02^\circ$  and  $6,37^\circ$  contrary to the measurements during the previous spring. The actual angle of attack is factor 1,53 higher. Despite the display flicking there was no noticeable movement of the model. Arteform did not look at the measured lift coefficient values, but decided to make multiple reference measurements with the clean model before and after the sandpaper and fluids tests and select those reference tests with the desired angle of attack displayed. Arteform did not either establish the accuracy of the measurements. This led to a large number of repeated reference and other tests increasing the total number of wind tunnel runs from 19 to 38. With both lift coefficient and displacement thickness measurements the number of files to be analyzed increased from 38 to 76. All this transpired to Trafı after the delivery of the files.

When checking the clean wing reference test results it was noticed later on at Trafı that the lift coefficient after rotation was constant, independent of the electronically displayed angle of attack value. Possibly the flicking of the electronic display was only a local electronic fault. However the average lift coefficient had increased from the value  $C_L=1,497$ , measured during the previous spring, to an average value of  $C_L=1,539$ . Arteform did not have an explanation for this increase, but it may be so that for some reason the angle to which the model was rotated had slightly increased. The lift coefficient increase of  $\Delta C_L=0,042$  corresponds to an angle of attack increase  $\alpha=0,39^\circ$  with the previously determined lift curve slope of  $C_{L\alpha}=6,103$  per rad (ref. [1] Koivisto page 6).

The repeatability of the lift coefficient measurements was however good. As will be shown in the next two chapters the deviations of the clean wing average values during the sandpaper measurements were even smaller than during the previous spring. During the first day of the fluids measurements the deviation of the clean wing average lift coefficient unexpectedly increased with about factor 4 to about  $\Delta C_L=\pm 0,01$ . Arteform had no explanation for the degradation of the accuracy. The degraded accuracy is still relatively good being about 20% of the lift loss due to the fluid. During the second day of fluids measurements the lift coefficient measurement accuracy was back on the good level of the sandpaper tests.

The boundary layer displacement thickness values of the clean wing reference tests were studied in detail at Trafı. The large number of test cases provided an extensive base for establishing the boundary layer rake measurement accuracy. As the boundary layer displacement thickness is not so sensitive for angle of attack changes as the lift coefficient, the average value was not much changed from the measurements during the previous spring. The average value of the clean wing reference case changed from the spring measurement value  $\delta^*=4,42$  mm to 4,52 mm.

The spring measurements had a maximum deviation of  $\Delta\delta^*=0,32$  mm from the average value which was however influenced by the movement of the rakes during the measurements. The autumn measurements were not anymore affected by rake movements, but due to a 7 factor larger number of measurements the maximum deviation from the average value increased slightly to  $\Delta\delta^*=0,33$  mm. The larger number of measurements also showed that the left and right hand side rakes gave about 0,46 mm different average values. The measurement repetitive accuracy on one of the rakes only was also better. The maximum deviation from the average value on one side only was less than  $\Delta\delta^*=0,14$  mm. A more detailed presentation of the calculation of the average values and the variation of the results will be given in the following two chapters.

It was noticed during the investigation of the fluids test results, that the previously used boundary layer displacement thickness calculation routines in the Excel files did not function anymore. It turned out that Arteform, without telling the customer, had used on the right hand side rake one of the eight pressure measurement tubes for their own experiments during the Trafı tests. As will be seen in the following chapters the degradation on

accuracy was small and caused mainly a nuisance of extra work to sort out what really had been measured.

The first test of Type IV fluid was made on purpose with all rake tubes unplugged. At the beginning of the test the three tubes closest to the wing model surface were contaminated with the fluid but during the interesting part of the test, after the wing model rotation, the tubes were again open and functioning. In the second test run of Type IV fluid all tubes were still unplugged but the results showed disturbances in the three pressure tubes closest to the model surface. In the two runs with Type II fluid the three pressure tubes closest to the surface were plugged. The velocity profiles of all boundary layer measurements were plotted and an estimate will be made in the following chapters how the plugging influenced the measurements.

### 3.4 Sandpaper measurements

The goal of the sandpaper measurements was to find a sandpaper roughness that gives the same effect as the Cold Soaked Fuel Frost with a dimensionless thickness of  $t/c=0,0006$ . This frost thickness gave a liftoff lift coefficient reduction of about 6%, the amount of which is now accepted due to de/anti-icing treatment at take-off, see FAA Policy Statement ref. [15]. Another goal was to correlate the lift reduction to boundary layer displacement thickness values. Both the boundary layer rake measurements at the main wing upper surface aft edge and the force balance were simultaneously performed as time histories during the simulated take-off sequence. The interesting part is after rotation and with sandpaper the values are unchanged at constant angle of attack.

The sandpaper measurements were performed in three days, using one grit size per day. Each day also clean wing reference measurements were done before and after the sandpaper measurements. Summaries of the sandpaper runs are presented in Table 3, Table 4 and Table 5. The target angle of attack in the wing model control system was  $5,9^\circ$  if nothing else is indicated in the tables. This has in the past given an actual indicated control angle of attack  $\alpha_i$  from  $5,98^\circ$  to  $6,02^\circ$ . However, the control system has lately more often indicated an actual control angle of attack of  $6,37^\circ$ . The magnification factor between the wing model angle of attack and control angle of attack is 1,53. Corresponding to a control angle of attack of  $5,9^\circ$  the factor yields a nominal wing model angle of attack  $9,027^\circ$ . During the November 10th measurements the control angle of attack display was during two wind tunnel runs flicking between two values. The display value was not registered for two runs. The November 14th wind tunnel runs contain two cases with different target values for the angle of attack.

**Table 3.** Measurements of sandpaper roughness P40 on November 10th 2017.

Run	Description	$\alpha_i$ [°]
Ref 1	Clean wing reference run	6,02...6,37
Ref 2	Clean wing reference run	6,02...6,37
Ref 3	Clean wing reference run	
Ref 4	Clean wing reference run	6,37°
P40 Run1	Sandpaper P40	6,02°
P40 Run2	Sandpaper P40	6,37°
P40 AluLE	Sandpaper P40 with aluminum tape at the fore edge	6,02°
P40 P120Strip	Sandpaper P40 with P120 strip in front of the fore edge. The strip detached from the wing surface during the run.	
P40 P120Strip AluLE	Sandpaper P40 with P120 strip in front of the fore edge secured with aluminum tape	6,02°
Ref after1	Clean wing reference run	6,02°

**Table 4.** Measurements of sandpaper roughness P80 on November 13th 2017.

<b>Run</b>	<b>Description</b>	<b><math>\alpha_i</math> [°]</b>
Ref 1	Clean wing reference run	5,98
Ref 2	Clean wing reference run	6,02
P80 AluLE Run1	Sandpaper P80 with aluminum tape at the fore edge	6,37
P80 AluLE Run2	Sandpaper P80 with aluminum tape at the fore edge	6,37
P80 AluLE Run3	Sandpaper P80 with aluminum tape at the fore edge	5,98
Ref after1	Clean wing reference run	6,37°
Ref after2	Clean wing reference run	6,02

**Table 5.** Measurements of sandpaper roughness P120 on November 14th 2017.

<b>Run</b>	<b>Description</b>	<b><math>\alpha_i</math> [°]</b>
Ref 1	Clean wing reference run	5,98
Ref 2	Clean wing reference run	6,37
P120 AluLE Run1	Sandpaper P120 with aluminum tape at the fore edge	6,37
P120 AluLE Run2	Sandpaper P120 with aluminum tape at the fore edge	6,37
P120 AluLE Run3	Sandpaper P120 with aluminum tape at the fore edge	6,37
P120 AluLE Run4	Sandpaper P120 with aluminum tape at the fore edge. Target $\alpha_i=5,8^\circ$	5,78
P120 AluLE Run5	Sandpaper P120 with aluminum tape at the fore edge. Target $\alpha_i=6^\circ$	6,41
P120 AluLE Run6	Sandpaper P120 with aluminum tape at the fore edge. Rotation rate 2,5 °/s	6,02
Ref after1	Clean wing reference run	6,37
Ref after2	Clean wing reference run	6,02

### 3.4.1 Lift coefficient

The measurement frequency of the force balance measurements was about 0,45 seconds. The clean wing measurements are collected into Figure 35, Figure 36 and Figure 37. The measurements show a small variation although the result should be the same. This is due to inaccuracy in force measurement, angle of attack after rotation and all other sources of possible variations. The average values of twenty measurement points (about 9 seconds) after the rotation gave for the highest curve a value  $C_L=1,542$  and for the lowest  $C_L=1,533$  giving a range of average lift coefficient values of 0,0089. During each day the variation in  $C_L$  was even smaller. The range of the lift coefficient values is slightly smaller, than the corresponding number 0,0097 during the previous spring measurements (ref. [2] Soenne et al page 43), showing that the repeatability of the measurements is good. However the average value during the sandpaper measurements had increased from the previous spring value  $C_L=1,497$  by  $\Delta C_L=0,040$  to  $C_L=1,537$ . It may be so that for some reason the angle to which the model was rotated had slightly increased.

The target angle of attack in the rotation is set in the tunnel control program. The acting angle of attack is read in an optical disc which is connected via linkage to the wing model. The actual value is compared in the control program with the target value and adjusted as needed. Possibly the reading of the optical disc position has changed from the previous spring. In the sandpaper tests the repeatability of the runs was as good as during the spring but with a shift in the lift coefficient after the rotation.

The repeatability of the averaged lift coefficient values  $\pm 0,0045$  is within the previously derived value  $\pm 0,006$  of ref. [1]. The measured balance force values contain wind tunnel corrections for flow blockage due to the model and test section boundary layer but not due to flow curvature due to the wing model. Thus the accuracy is on the repeatability of the lift coefficient not on the absolute value.

When two values of lift coefficient are measured it is possible that both errors have the same sign or opposite signs resulting in an error on the difference of 0 and 0,0089 respectively. Or the error on the difference could be some value in between. Assuming that the maximum errors act simultaneously in opposite directions is probably too conservative. However, it is likely that combining two inaccurate measurements cause a larger error than in a single measurement. Often a combined error, caused by several independent factors, is estimated using a root mean square value of the individual errors. The difference of two lift coefficients will then have an inaccuracy of  $\sqrt{2} * 0,0045 = 0,0063$ .

The lift coefficient time histories measured on a wing with different sandpapers on the upper surface are shown in Figure 38, Figure 39 and Figure 40. During the take-off roll before the rotation the lift coefficient should be constant as a constant angle of attack was specified. However, in all figures a varying lift coefficient is depicted. This is due to a backlash in the mechanical system controlling the angle of attack. At higher angles of attack the system bottoms and this problem has not affected the lift force measurements after the rotation.

As is seen in Figure 38 the lift coefficient of the wing model with P40 sandpaper is hardly dependent on the sandpaper fore edge configurations. The average lift coefficient of the three wind tunnel runs with P40 sandpaper (including the one with the P120 Strip Failed, the strip detached from the surface) was  $C_L=1,437$  with a range of lift coefficient values  $\Delta C_L=0,0023$ . For the wing model with P40 sandpaper and aluminum tape at the sandpaper fore edge the lift coefficient was  $C_L=1,438$ . P40 sandpaper with a P120 strip and aluminum tape increased the lift coefficient only slightly to  $C_L=1,440$ . The changes due to the tape are in a logical order, but only marginal and below the measurement accuracy.

Figure 39 shows three wind tunnel runs with P80 sandpaper and aluminum tape on the sandpaper fore edge. The average lift coefficient for the three runs was  $C_L=1,500$  with a range of lift coefficients of values  $\Delta C_L= 0,0084$  which was within the established measurement accuracy.

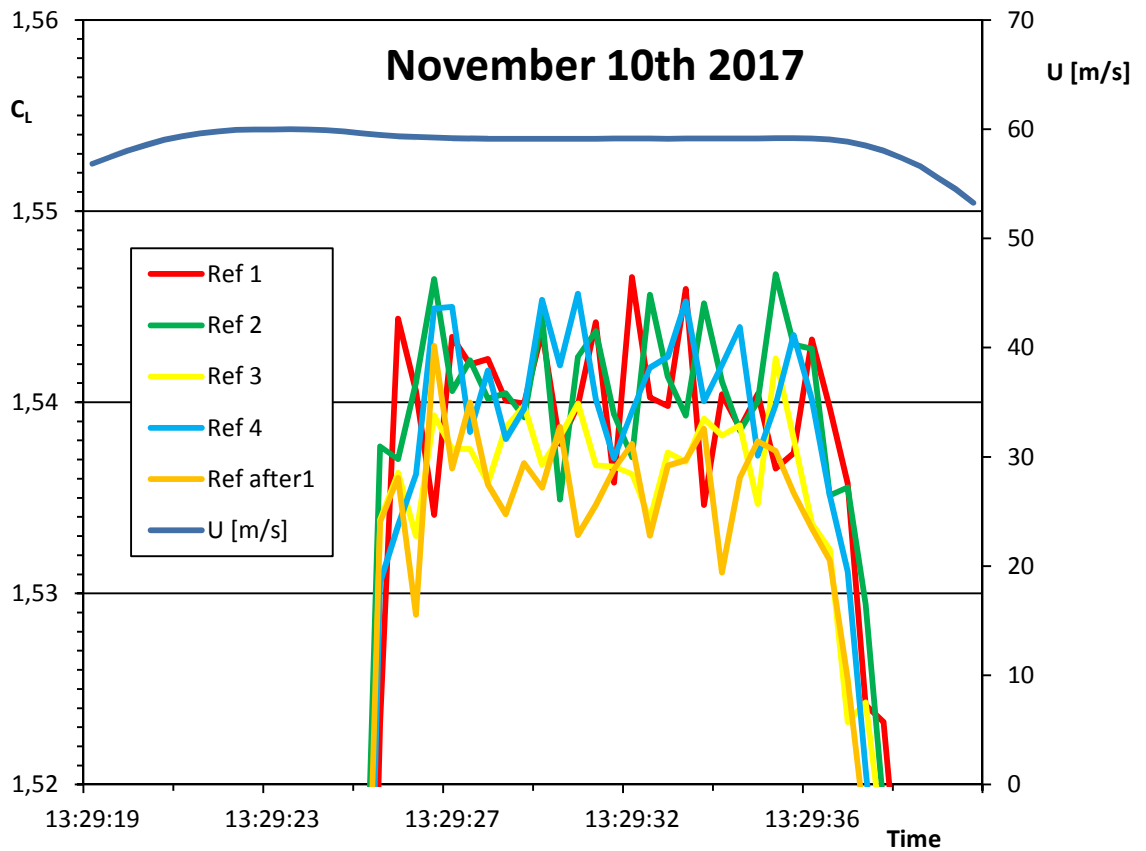
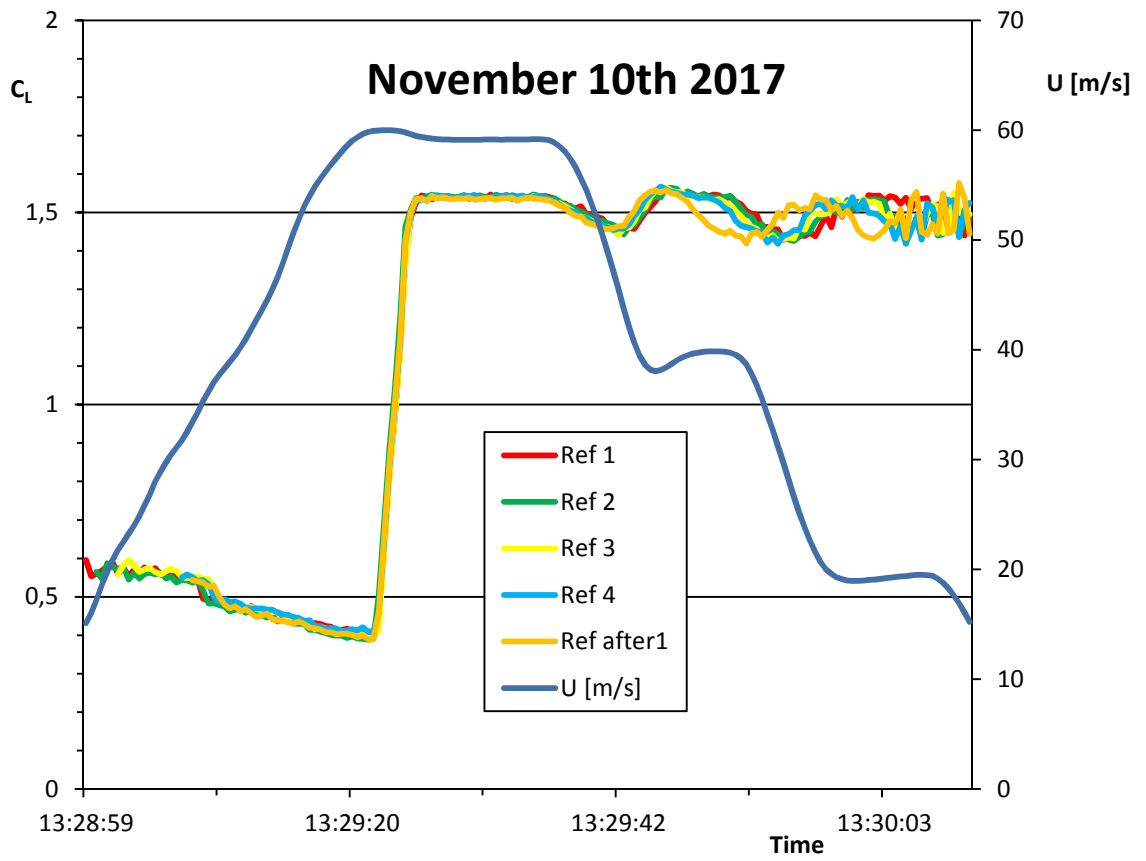


**Figure 35.** Lift coefficient  $C_L$  as function of time during a simulated take-off on a clean wing during the measurements on November 10th.

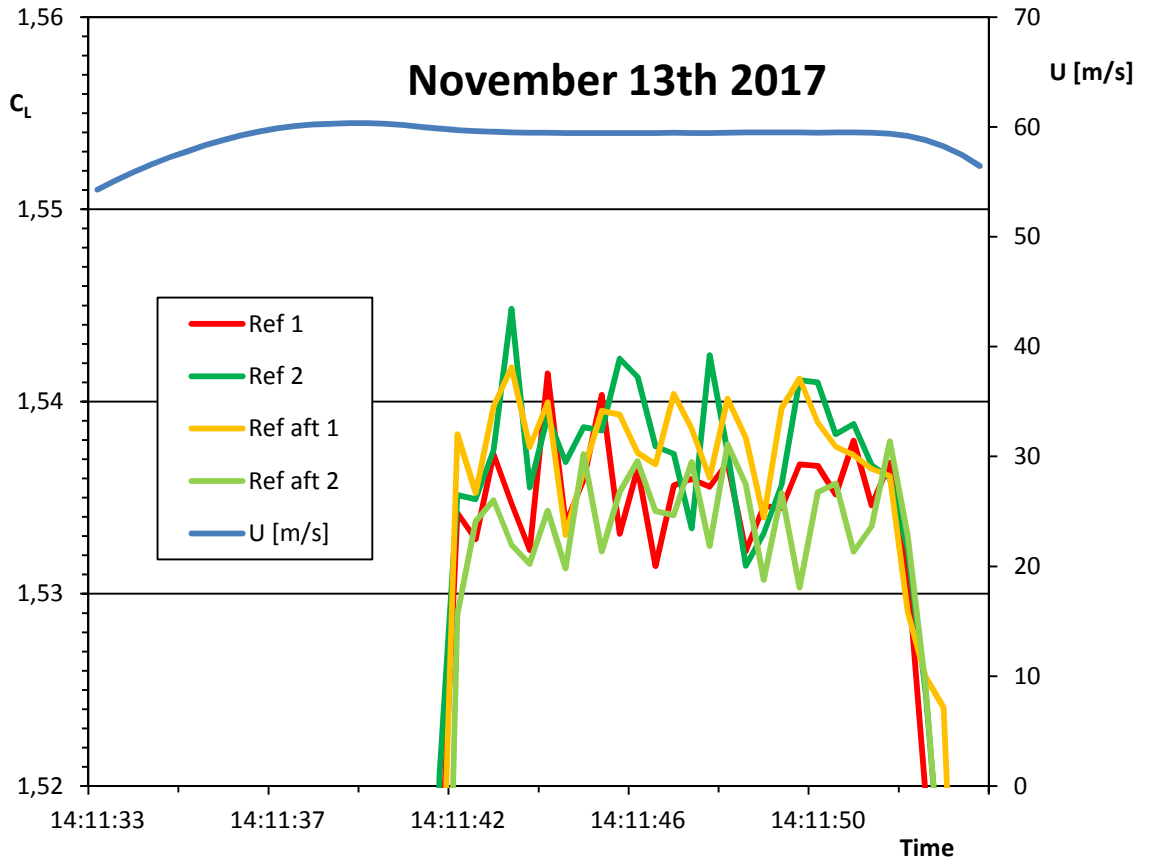
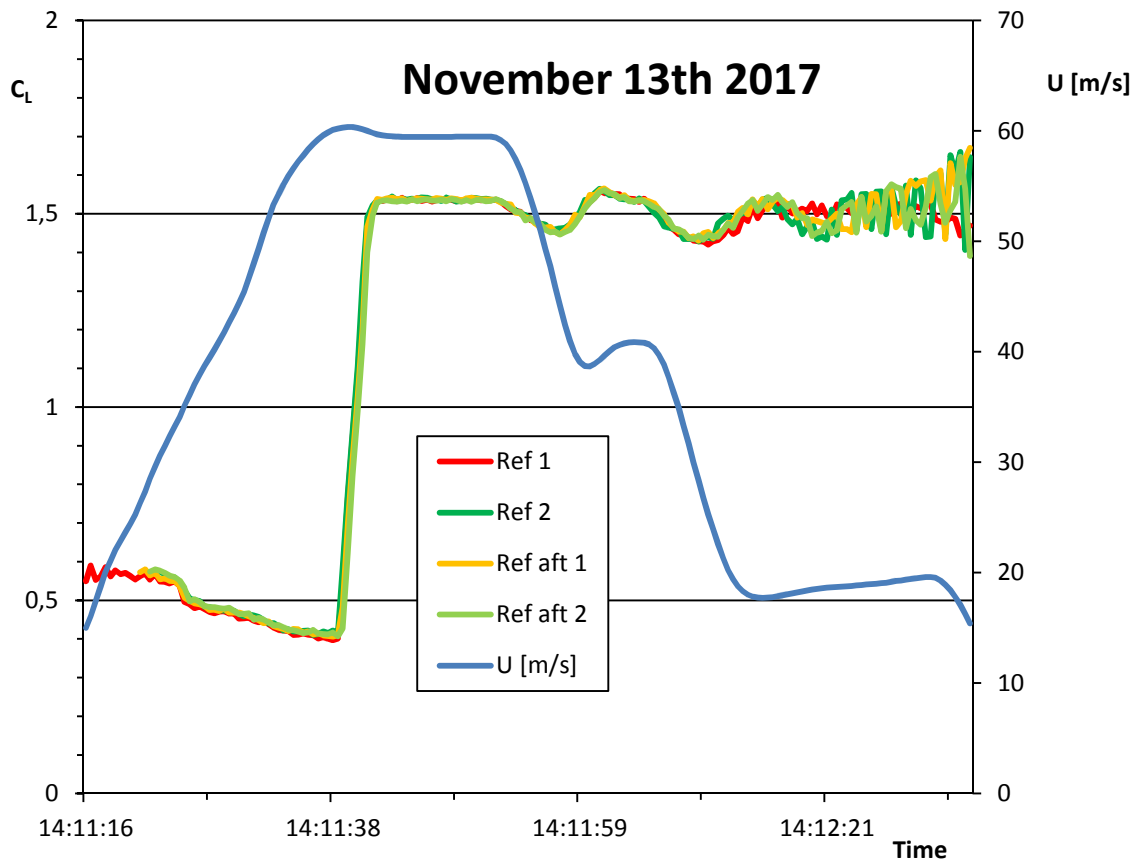


**Figure 36.** Lift coefficient  $C_L$  as function of time during a simulated take-off on a clean wing during the measurements on November 13th.

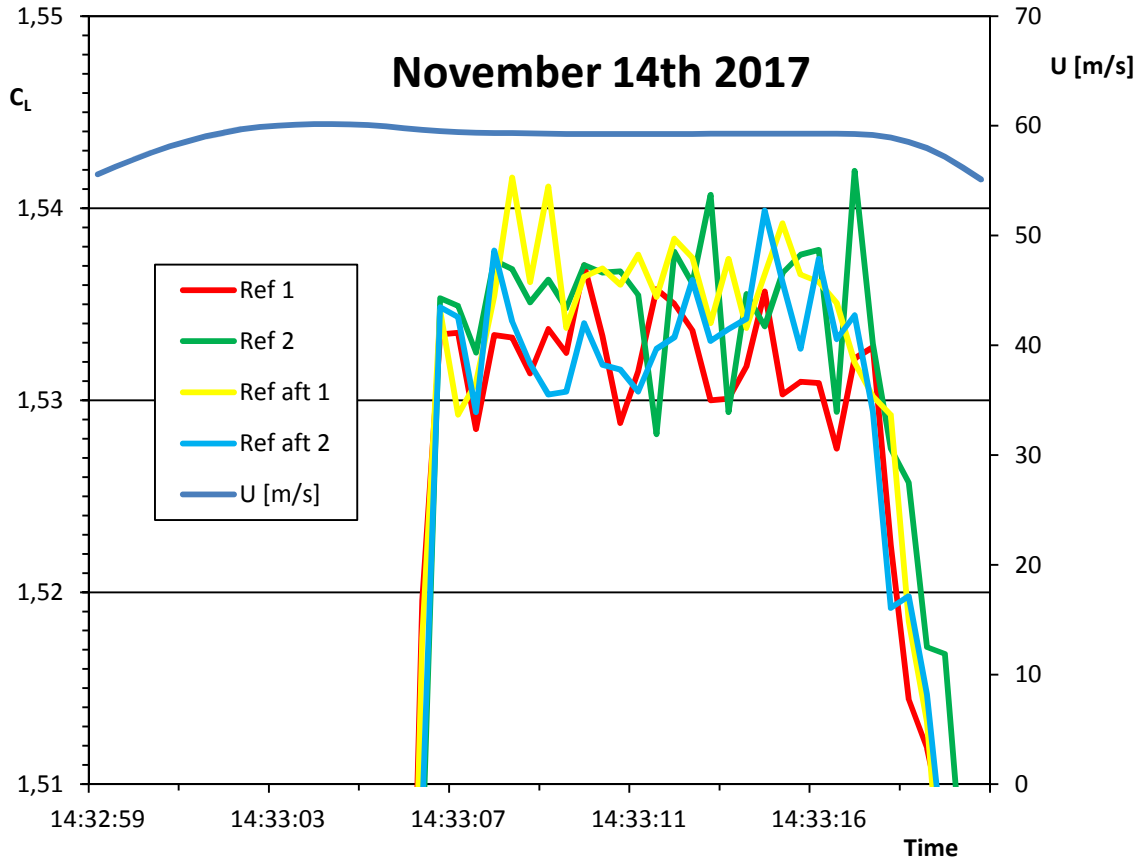
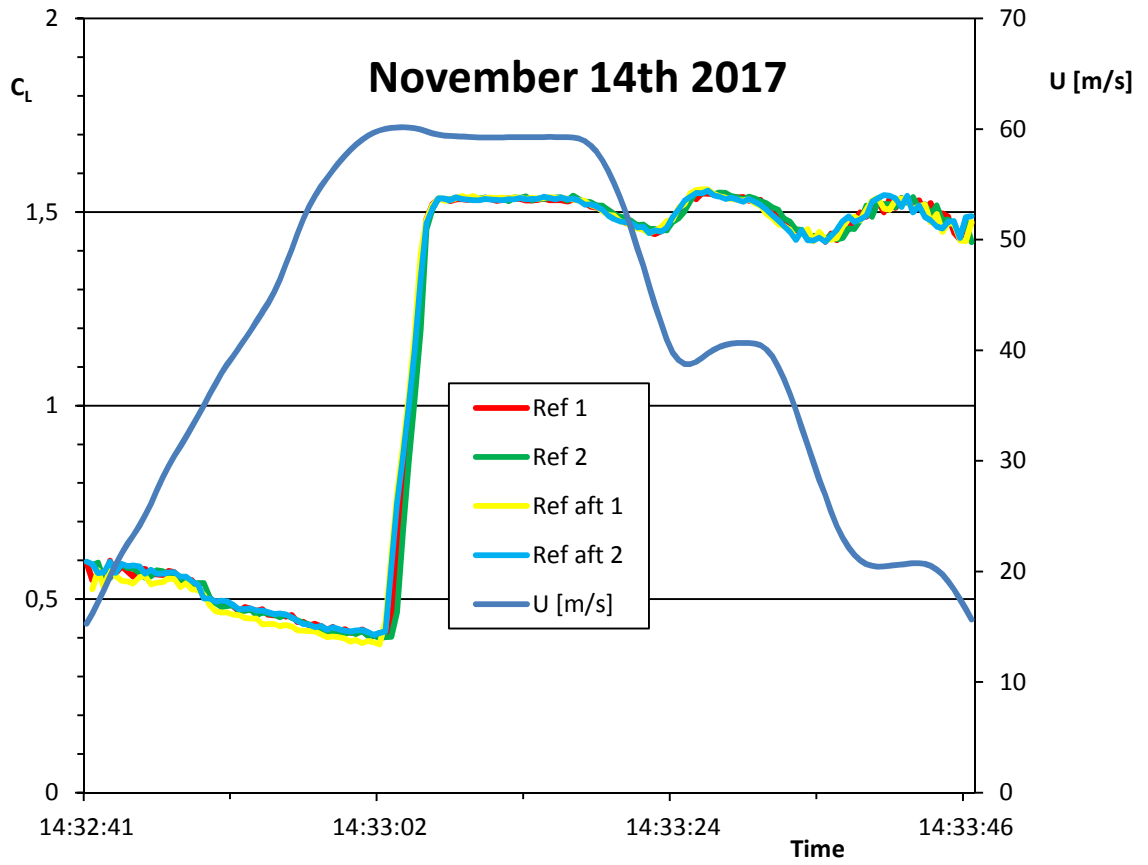


**Figure 37.** Lift coefficient  $C_L$  as function of time during a simulated take-off on a clean wing during the measurements on November 14th.

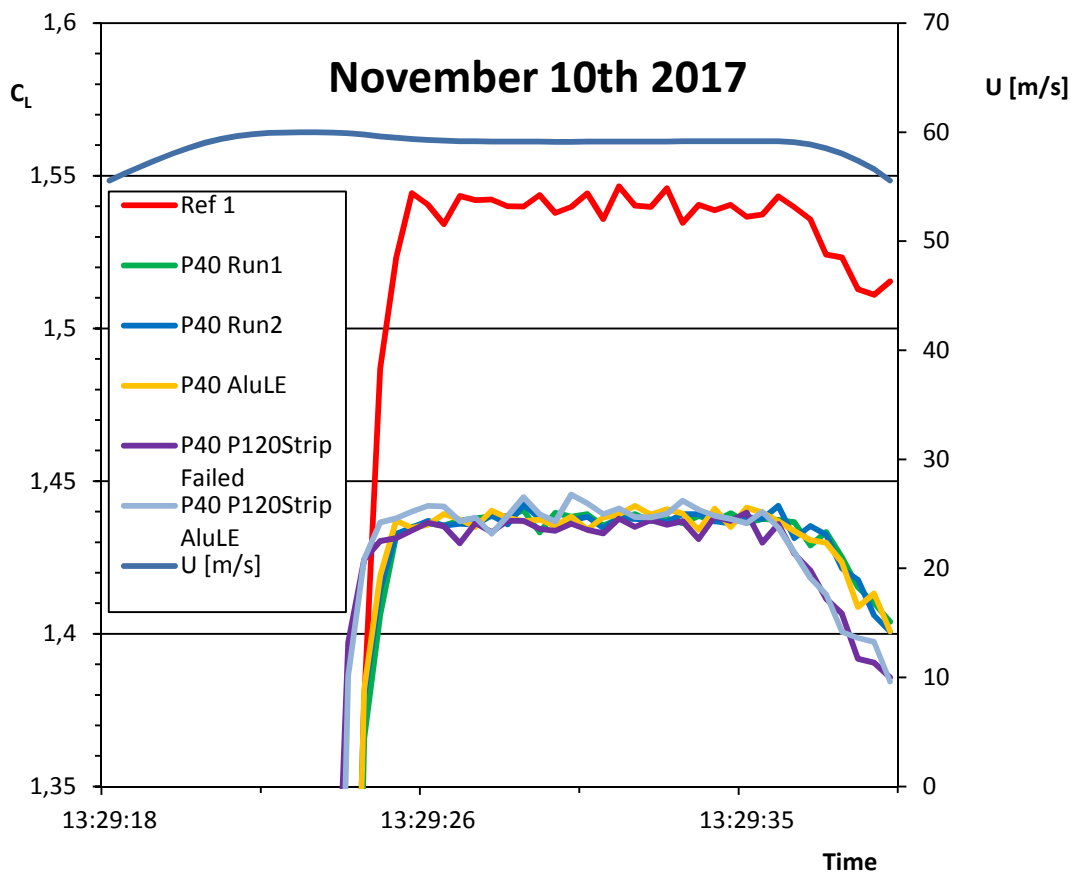
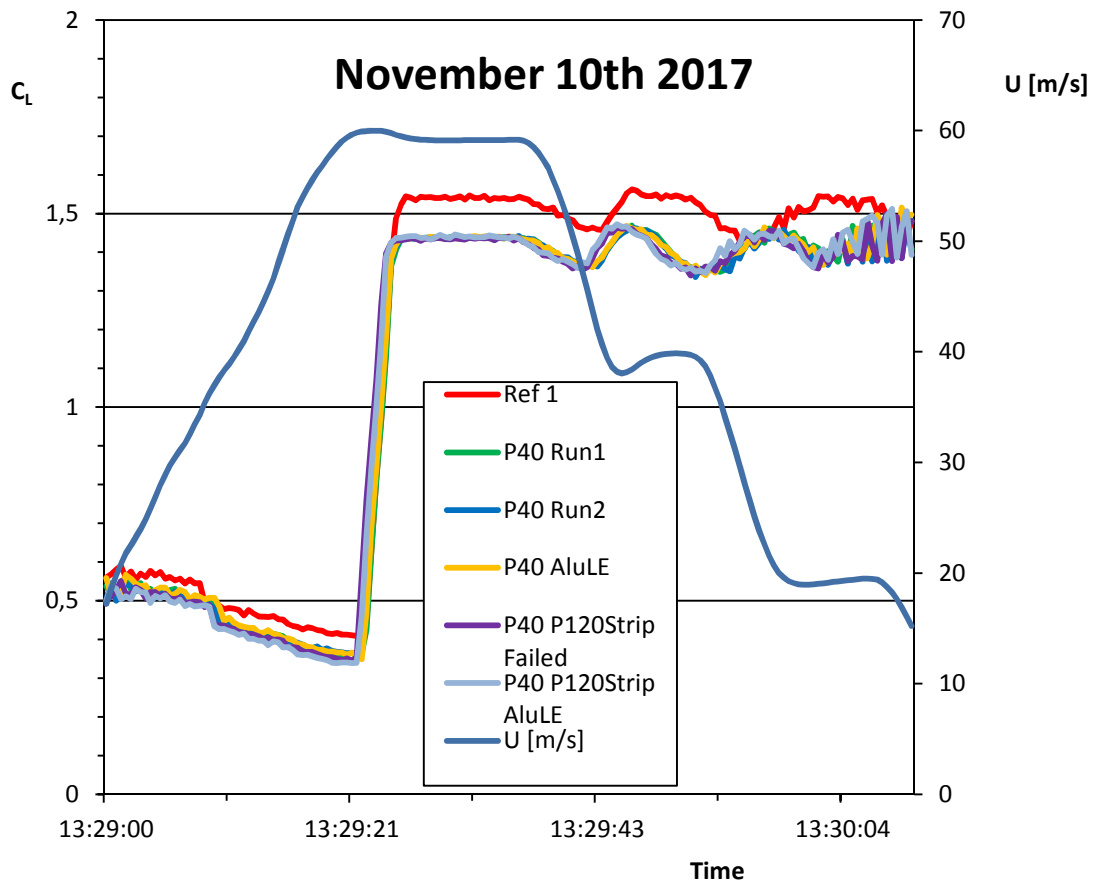


**Figure 38.** Lift coefficient  $C_L$  as function of time during a simulated take-off of P40 sandpaper measurements.

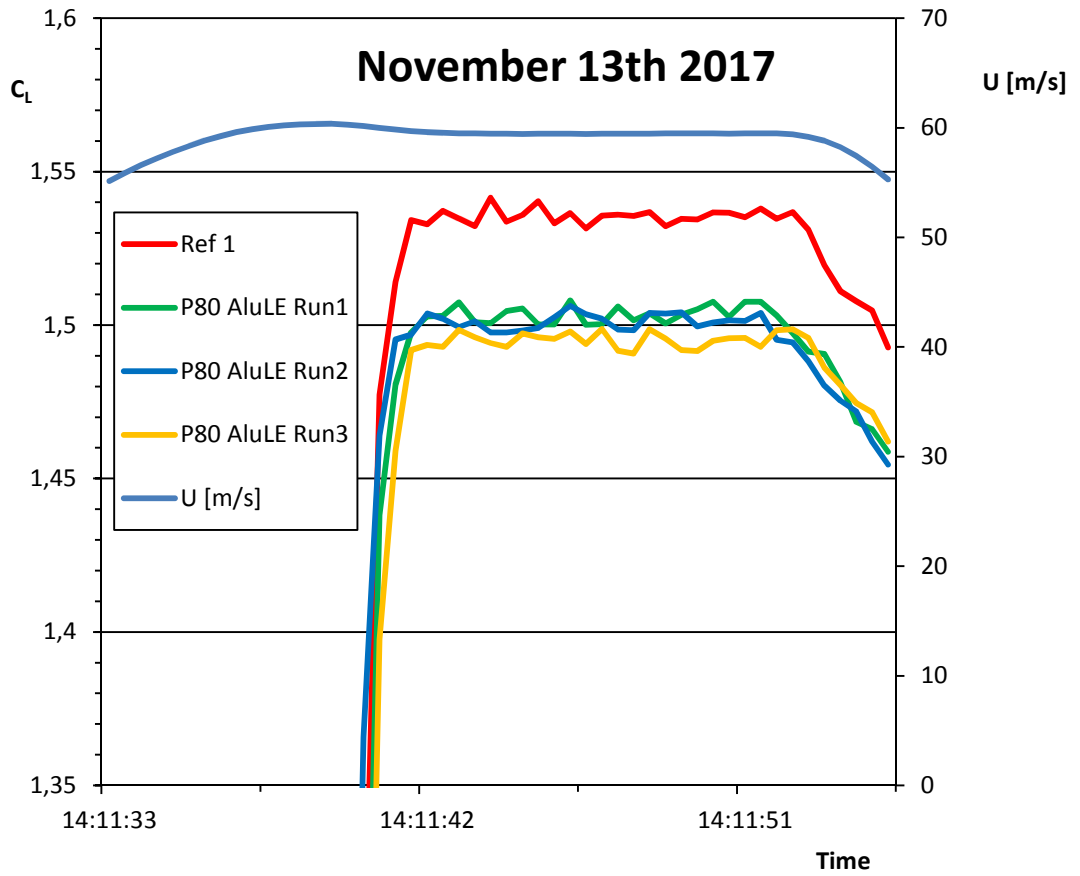
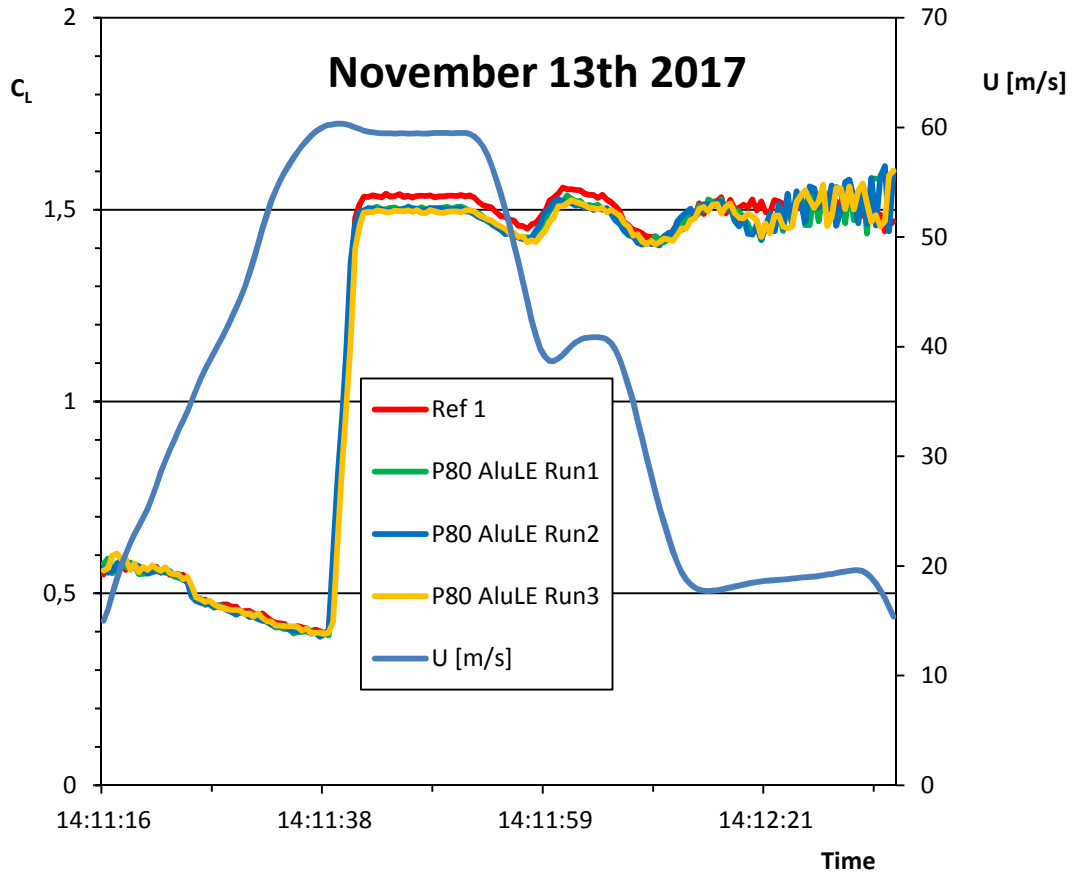


**Figure 39.** Lift coefficient  $C_L$  as function of time during a simulated take-off of P80 sandpaper measurements.

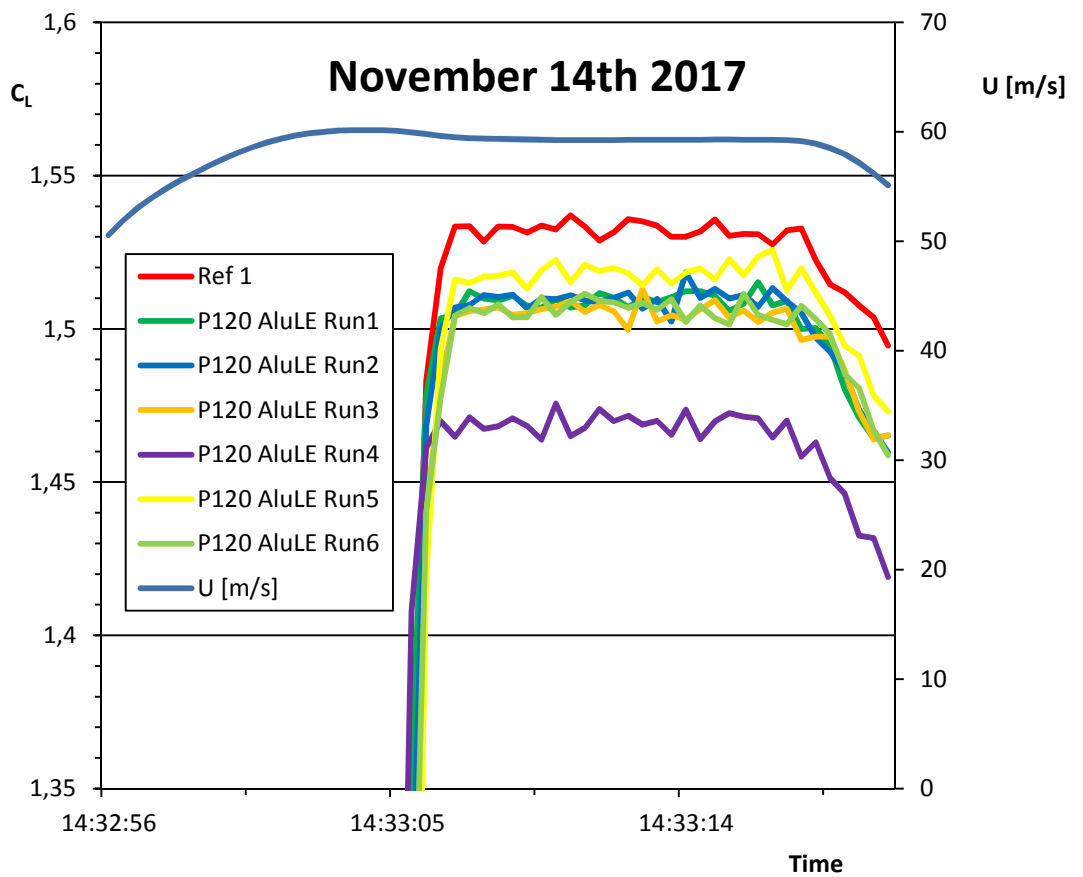
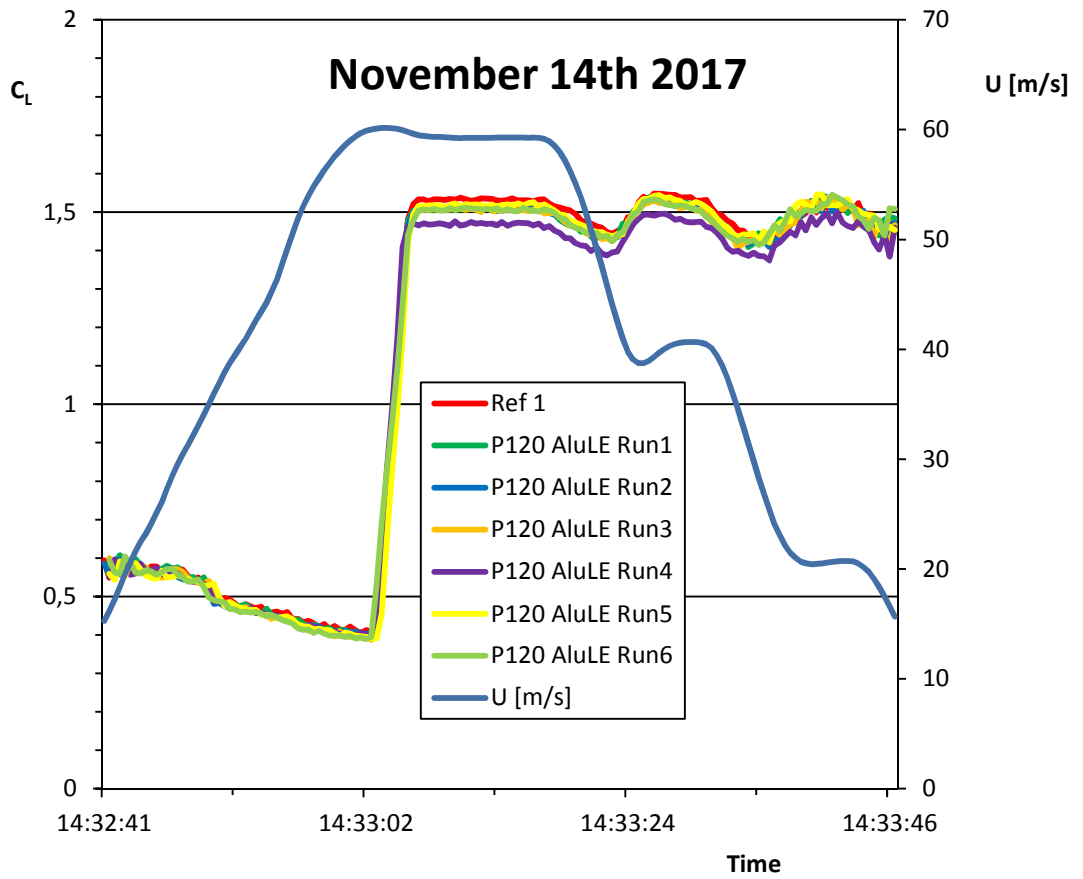


**Figure 40.** Lift coefficient  $C_L$  as function of time during a simulated take-off of P120 sandpaper measurements.

The wind tunnel tests for the P120 sandpaper contained three runs (run 1, 2 and 3) with the nominal target angle of attack. Runs 4 and 5 tested different target angles of attack. Run 6 was made with the nominal target angle of attack but with a lower rotation rate, which did not show an effect on the attained lift coefficient. The average lift coefficient of the four runs was  $C_L=1,508$  with a range of lift coefficient values  $\Delta C_L=0,0040$ .

The lift reduction due to sandpaper was determined in the above mentioned figures by calculating the difference of the clean wing and sandpaper wing average values of the twenty measurement points after the rotation. As the different sandpaper fore edge configurations had only a marginal effect on the lift coefficient the results are summarized for the different grid types in Table 6. The inaccuracy of the lift coefficient difference of 0,0063 gives an inaccuracy of 6...22% for the differences shown in the table.

The results are presented as relative lift degradation  $\Delta C_L / C_{L\text{Clean}}$  as function of relative thickness and roughness as this dimensionless presentation permits direct comparison with different airfoils and wings. The absolute reduction of the two-dimensional lift coefficient is transformed into wing lift coefficient reduction in the linear range in proportion of the three and two-dimensional lift curve slopes. Consequently the absolute value of the wing lift coefficient reduction is lower than on the two-dimensional airfoil, but the relative reduction values are the same. As the selected wing section for the wind tunnel model is representative for the HL-CRM jet aircraft configuration the lift reduction is also representative for the aircraft.

The sandpaper lift reduction values are presented together with previous measurements on Cold Soaked Fuel Frost in Figure 41 and Figure 42. There was no noticeable evaporation/melting of the frost before rotation in the tested temperatures. The first figure shows that the sandpaper values stick out of the other measured values when presented as function of surface roughness added dimensionless thickness. In the second figure the sandpaper values fit fairly well the linear trend of growing lift loss, when presented as function of dimensionless surface roughness height. It seems that for sandpaper the effect of backing paper contribution to the added thickness is not significant. The sandpaper roughness seems to be more relevant for the lift reduction. This feels logical as the effect of the backing paper is felt as a slight increase in the airfoil camber and thickness increasing the potential flow lift. The sandpaper roughness on the other hand is the dominating effect and it disturbs the upper surface boundary layer increasing the displacement thickness, which has a decambering effect.

**Table 6.** Lift coefficient reduction for different sandpaper grit values based on the measurements in Figure 38 to Figure 40.

Grit	t/c	k/c	$C_L$ Clean	$C_L$ Sandpaper	$\Delta C_L$	$\Delta C_L / C_{L\text{clean}}$
P40	0,00189	0,00068	1,537	1,437	0,100	0,065
P80	0,00088	0,00032	1,537	1,500	0,037	0,024
P120	0,00066	0,00020	1,537	1,508	0,029	0,019

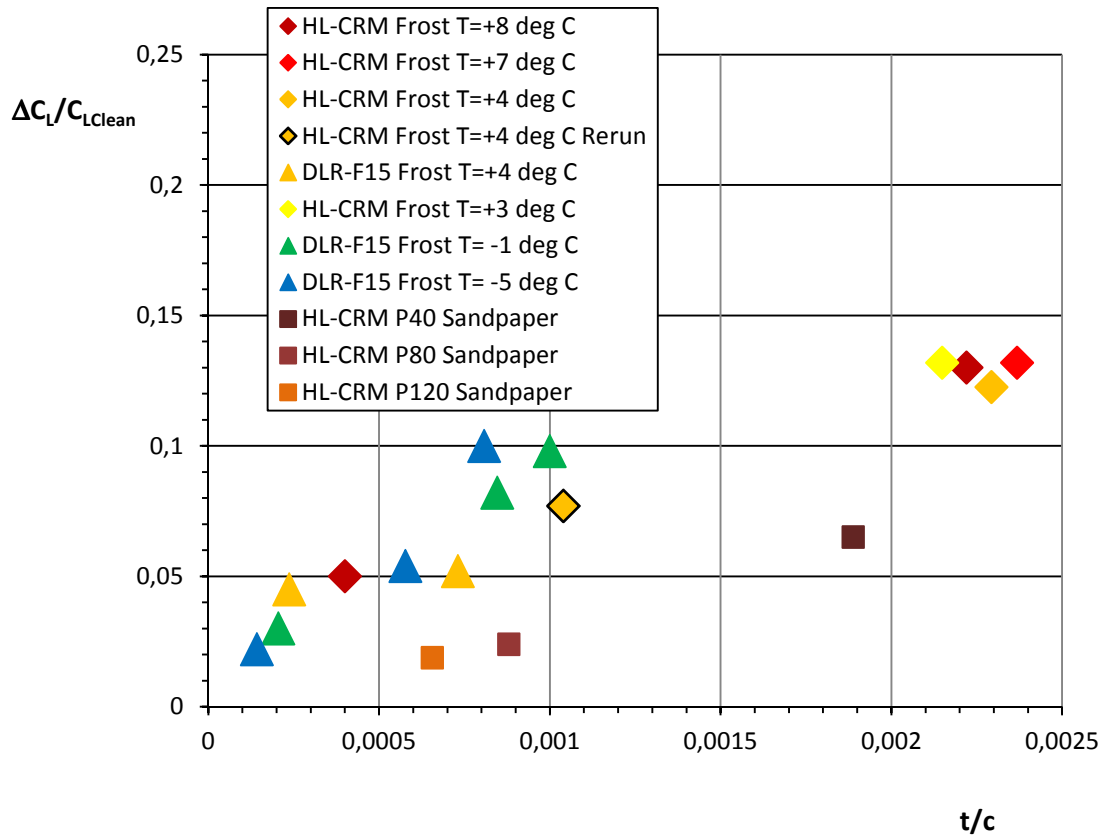


**Figure 41.** Relative Lift coefficient reduction as function of surface roughness added dimensionless thickness (data also from ref. [1], [2] and [16]).

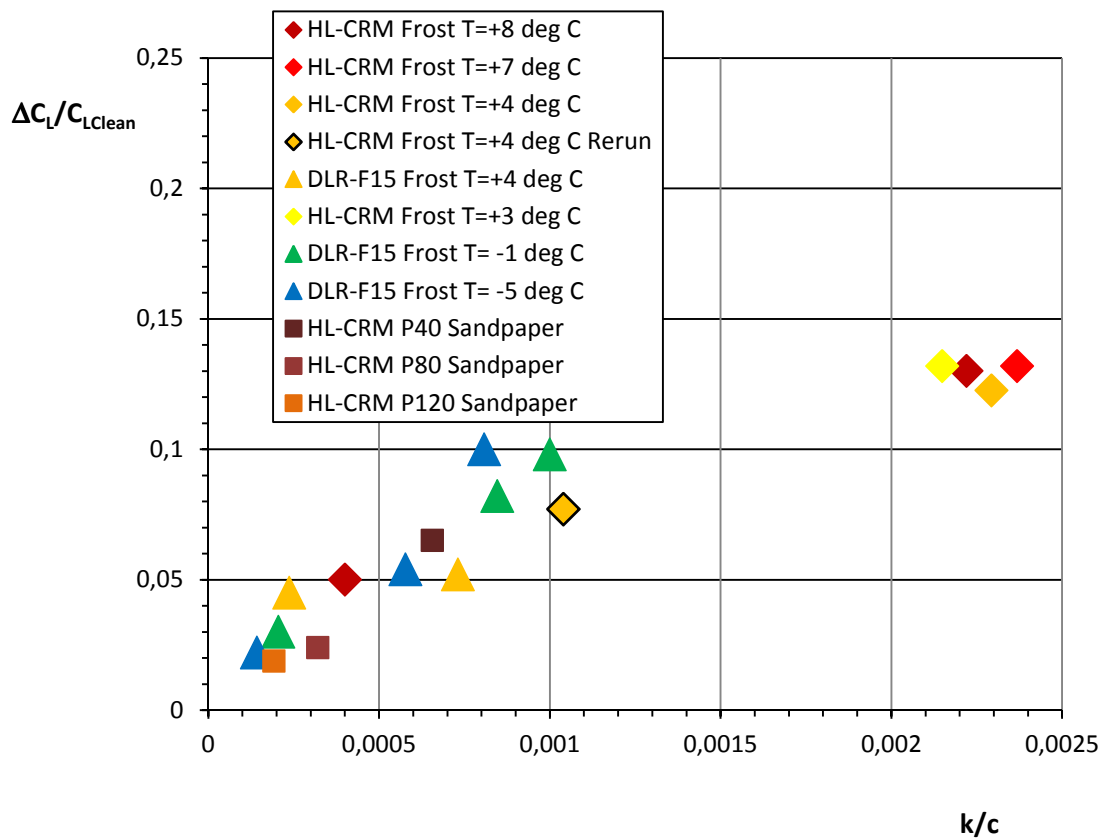


**Figure 42.** Relative Lift coefficient reduction as function of dimensionless surface roughness height (data also from ref. [1], [2] and [16]).

### 3.4.2 Boundary layer displacement thickness

The boundary layer displacement thickness values, corresponding to the lift force measurements, were measured with two boundary layer rakes at the aft edge of the airfoil main element. The measurement interval was 0,02 seconds. A moving averaging over 26 values, corresponding to a time period of 0,52 seconds, was performed to smooth out the measured pressures. In spite of this the time histories show quite detailed characteristics.

The measured boundary layer displacement thicknesses on clean wing are collected into Figure 43, Figure 44 and Figure 45. The measurements show a small variation at constant angle of attack after the rotation although the results should be the same. This is due to inaccuracies in pressure measurements, angle of attack after rotation and all other sources of possible variations. A small extra inaccuracy was caused by the missing outermost pressure value on the right hand side rake, which had to be taken the same as the corresponding value on the left hand rake. It is evident in the figures that the displacement thickness results of the left and right hand side rakes are grouped at slightly different levels of about 0,4 mm. Obviously the rakes are slightly different or are positioned at slightly different levels from the wing surface or in slightly different directions. Due to the limited number of wind tunnel runs this was not obvious in the previous spring measurements of ref. [2] Soenne et al, in which the rakes were suspected to have moved. Then it looked like only one measured curve of six was affected by rake movement as only one curve was aside from the group of other measurements. Now it seems that the isolated right hand measurement was done with a rake which had not moved during the measurements. The other two right hand side rake results probably contain inaccuracy due to rake movement as the curves were grouped together with the left hand measurements. Besides this the new data does not change anything in the ref. [2] report, but the repeatability seems now to be better on an individual rake.

The average values of each curve after the rotation were calculated using 250 measurement points corresponding to a time period of 5 seconds. The average value of the clean wing displacement thicknesses of the 14 left hand side rake measurements gave after the rotation a value  $\delta^*=4,75$  mm. The range of measured average values on the left hand side was  $\Delta\delta^*=0,17$  mm. On the right hand side the average value was  $\delta^*=4,36$  mm and the range of the measurements  $\Delta\delta^*=0,13$  mm. The average value of the left and right hand side measurements was now  $\delta^*=4,56$  mm whereas the corresponding value in the previous spring measurements was  $\delta^*=4,42$  mm so the repeatability seems to be good.

On one rake the repeatability seems to give a maximum deviation from the average value  $\Delta\delta^*=0,5*0,17=0,085$  mm. When calculating the difference of two boundary layer displacement thicknesses the accuracy is reduced to  $\Delta\delta^*=\sqrt{2}*0,085=0,12$  mm. This is a very good repeatability when the displacement thicknesses are more than 4 mm for the clean wing and even more with sandpaper. The absolute accuracy of the displacement thickness measurement is however less as the left and right hand side rakes give different results. The accuracy range is  $4,75-4,36+0,17=0,56$  mm and thus the maximum deviation is  $\pm 0,28$  mm, which is better than 7% on the clean wing boundary layer displacement thickness.

Time histories of the boundary layer displacement thickness with sandpaper are presented in Figure 46 to Figure 48. The average 250 point displacement thickness values, corresponding to a time period of 5 seconds, were calculated for the flow conditions after the model rotation. Boundary layer velocity profiles for the different sandpapers at a selected time instant after the model rotation are presented in Figure 49 to give some feel for the precision needed in the measurements. One can see that the straight line profiles are somewhat angular polygons due to limiting the number of pressure tubes to eight. The definition of the displacement thickness is

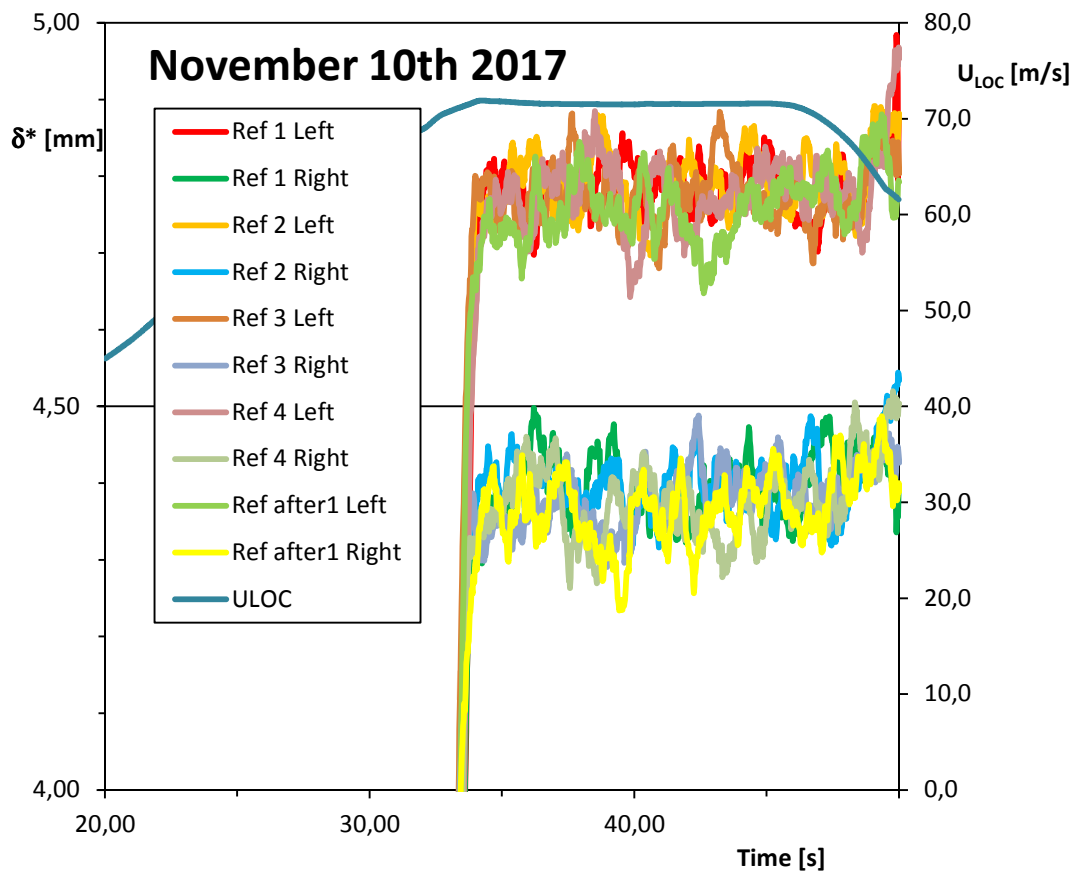
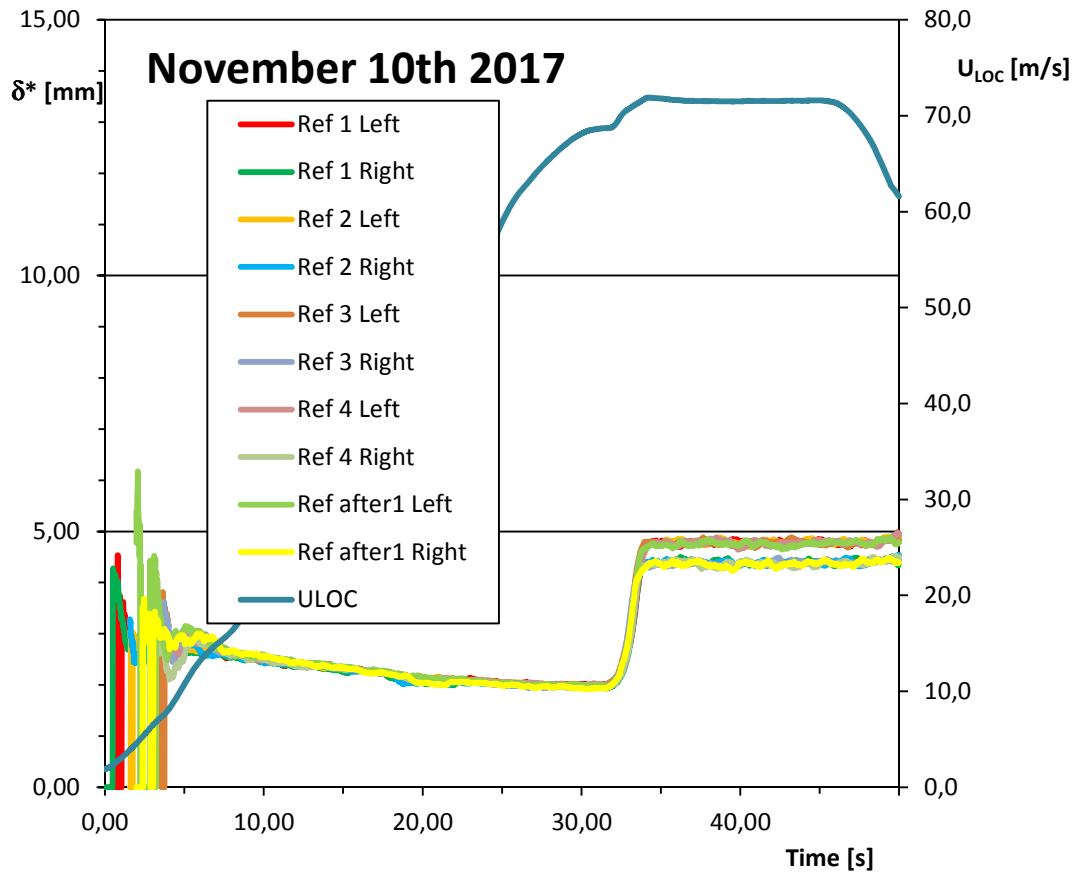


**Figure 43.** Boundary layer displacement thickness  $\delta^*$  as function of time during a simulated take-off on clean wing measurements.

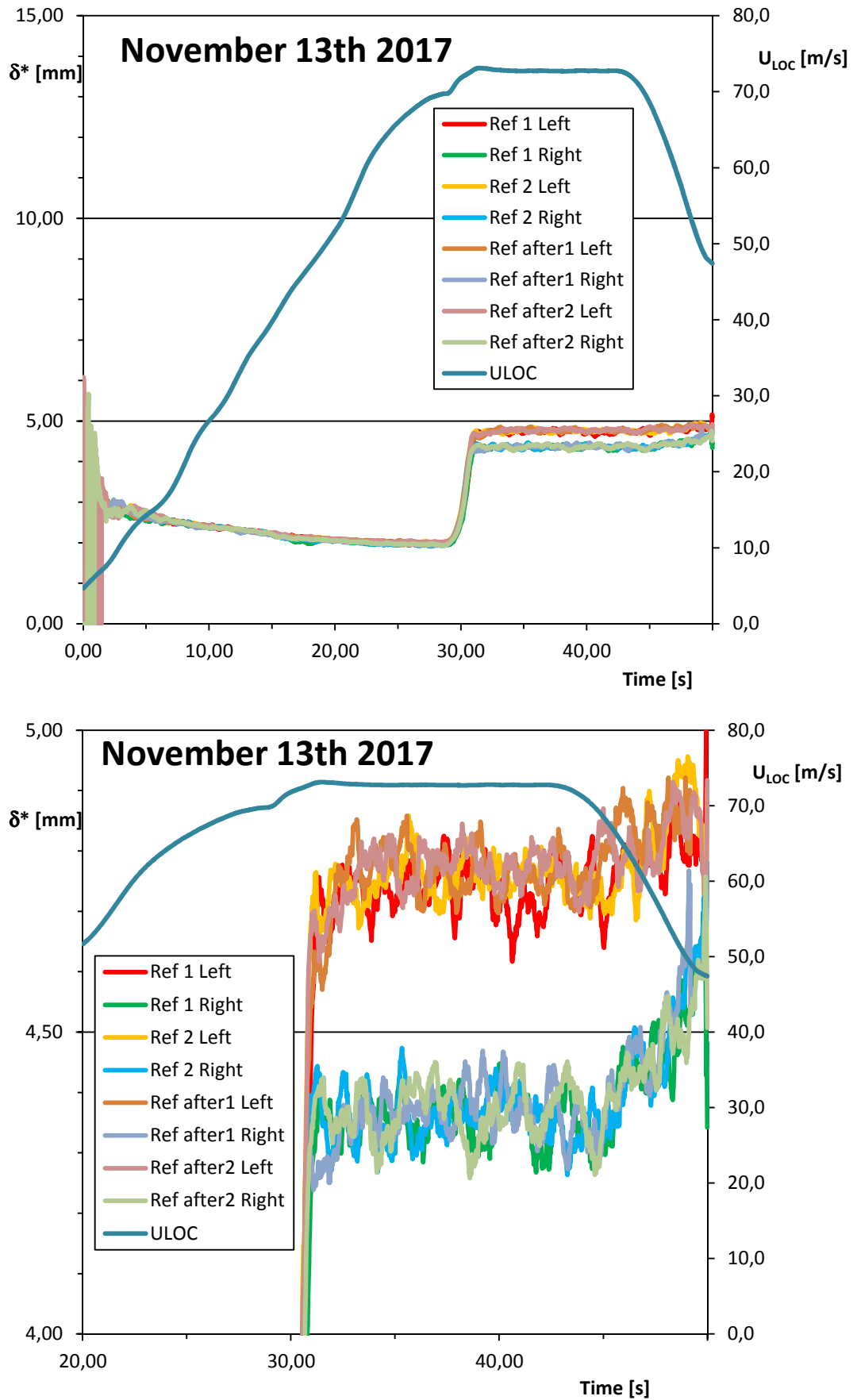


**Figure 44.** Boundary layer displacement thickness  $\delta^*$  as function of time during a simulated take-off on clean wing measurements.

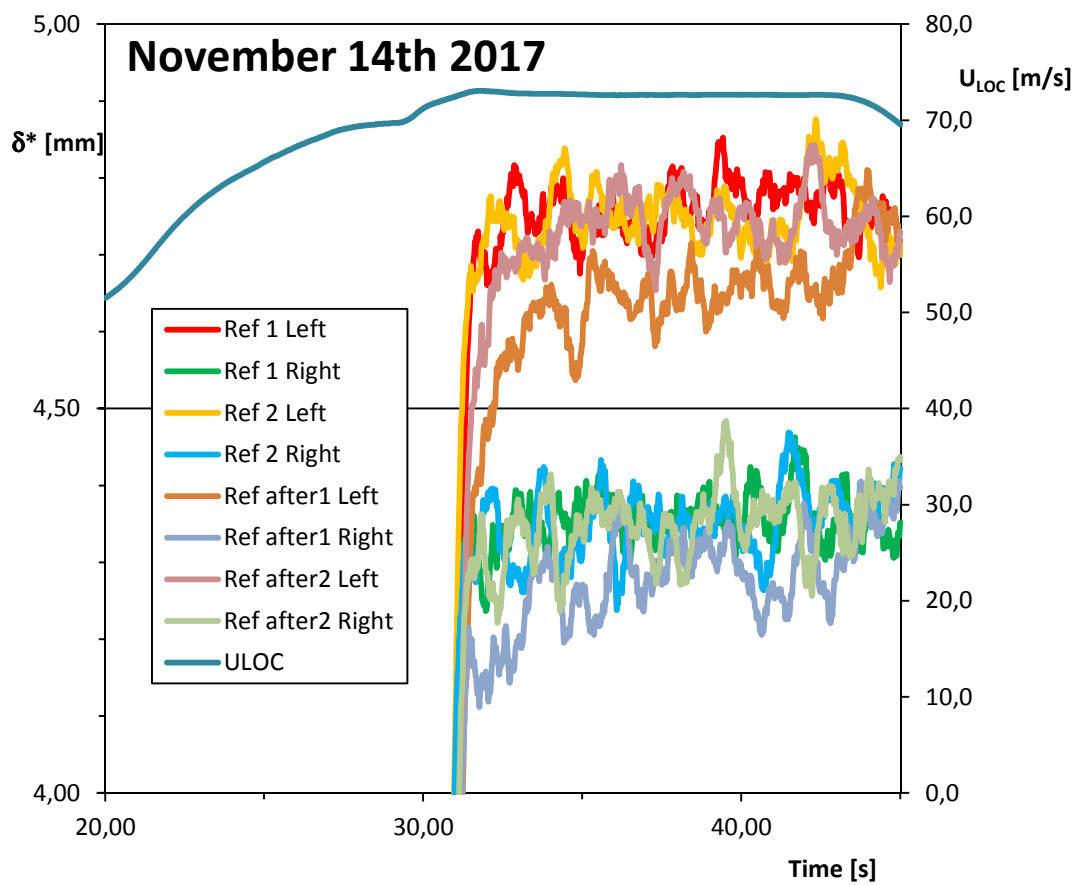
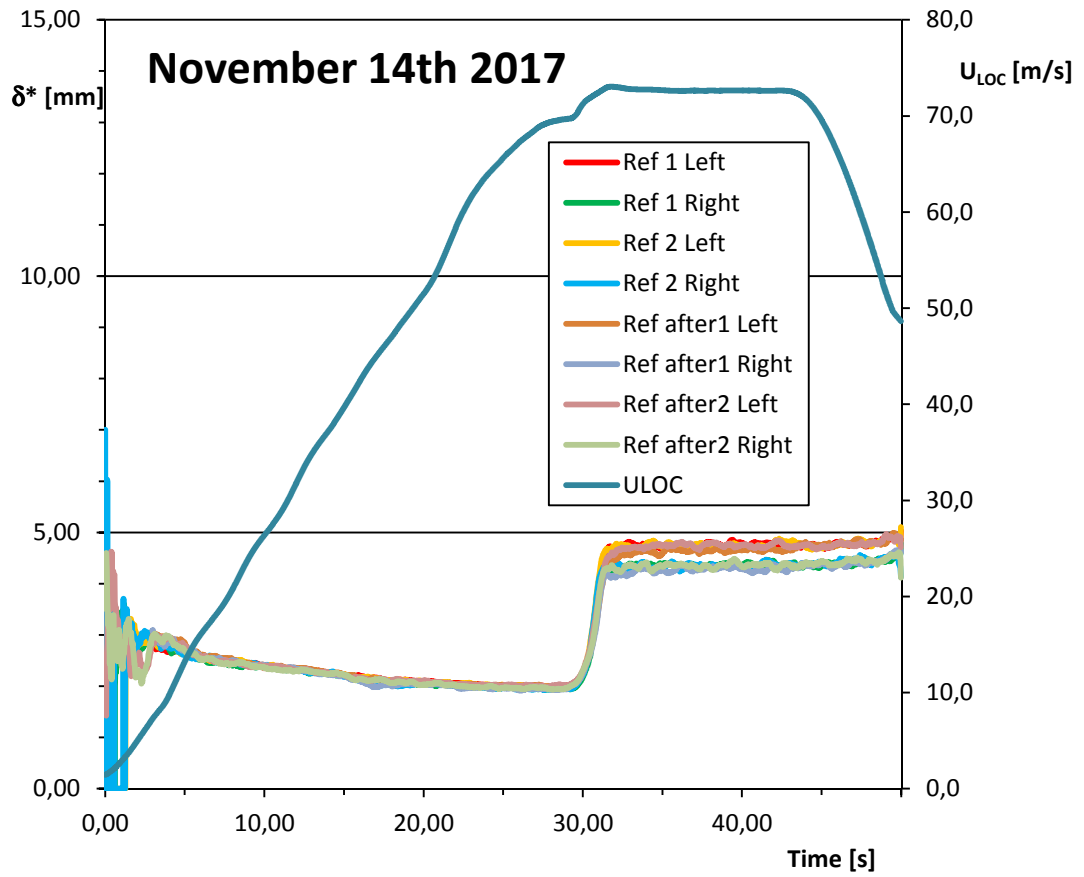


**Figure 45.** Boundary layer displacement thickness  $\delta^*$  as function of time during a simulated take-off on clean wing measurements.

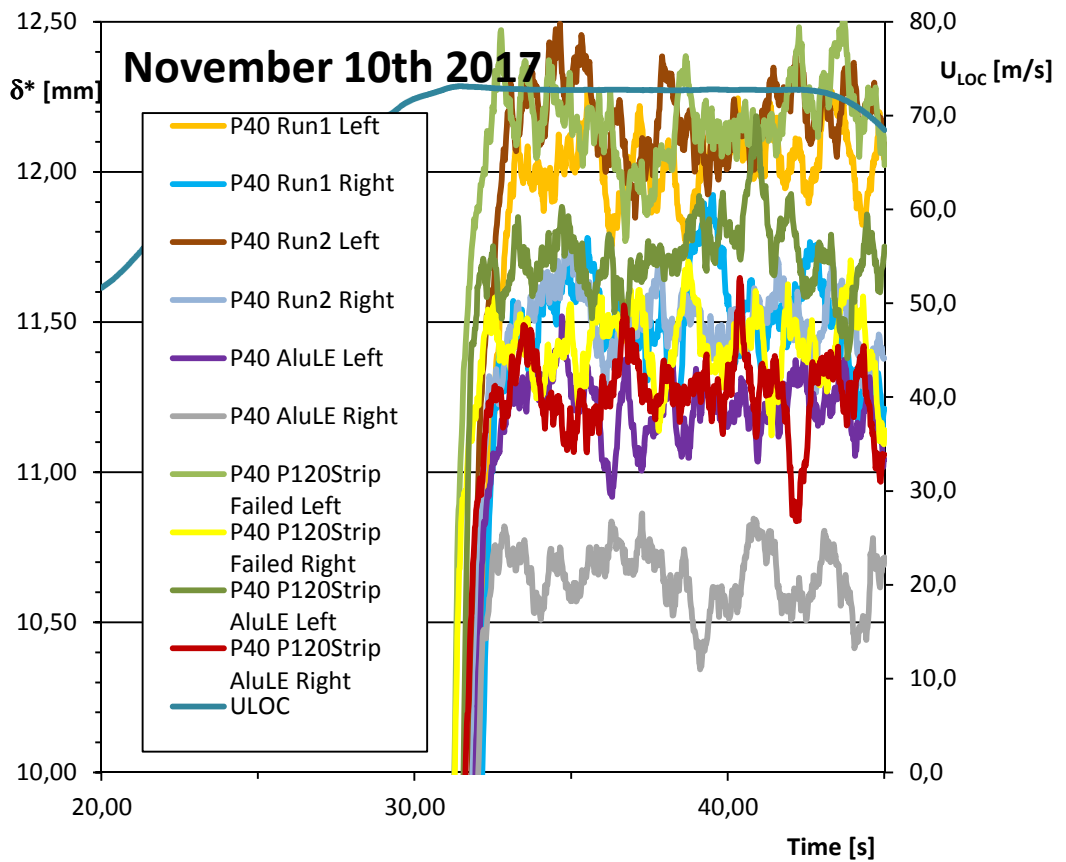
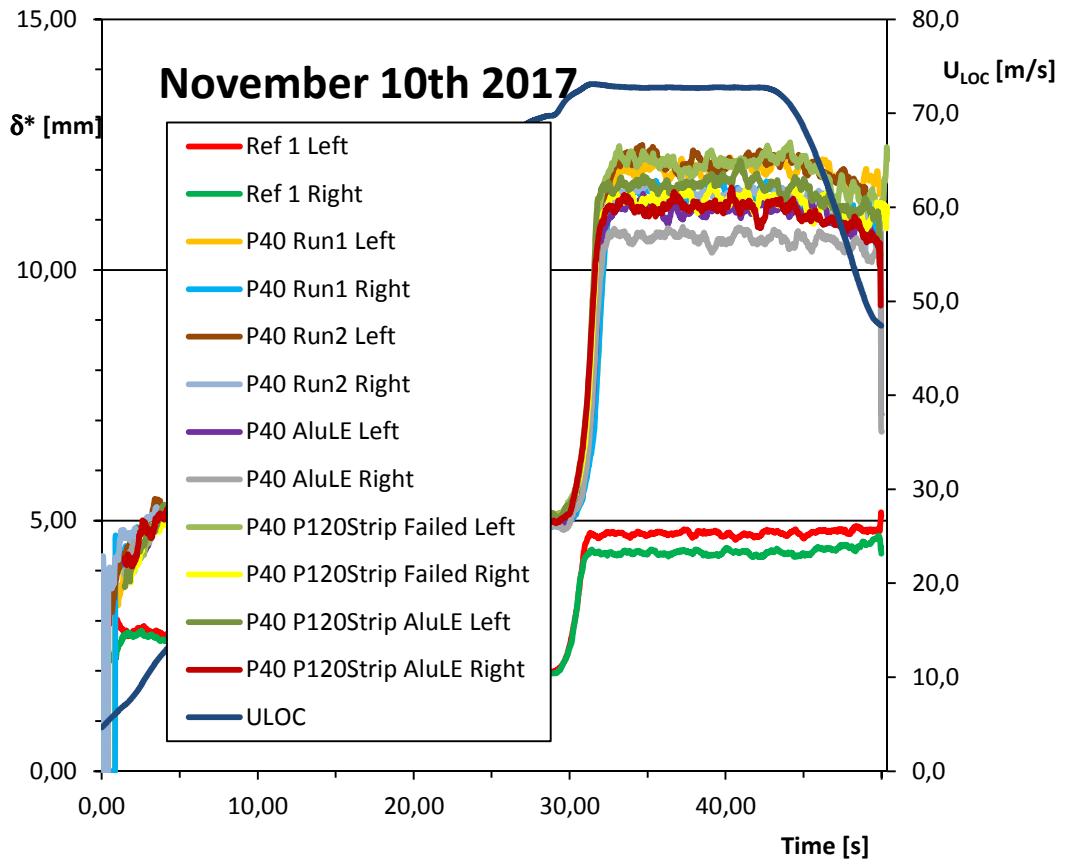


**Figure 46.** Boundary layer displacement thickness  $\delta^*$  as function of time during a simulated take-off with P40 sandpaper on the wing model.

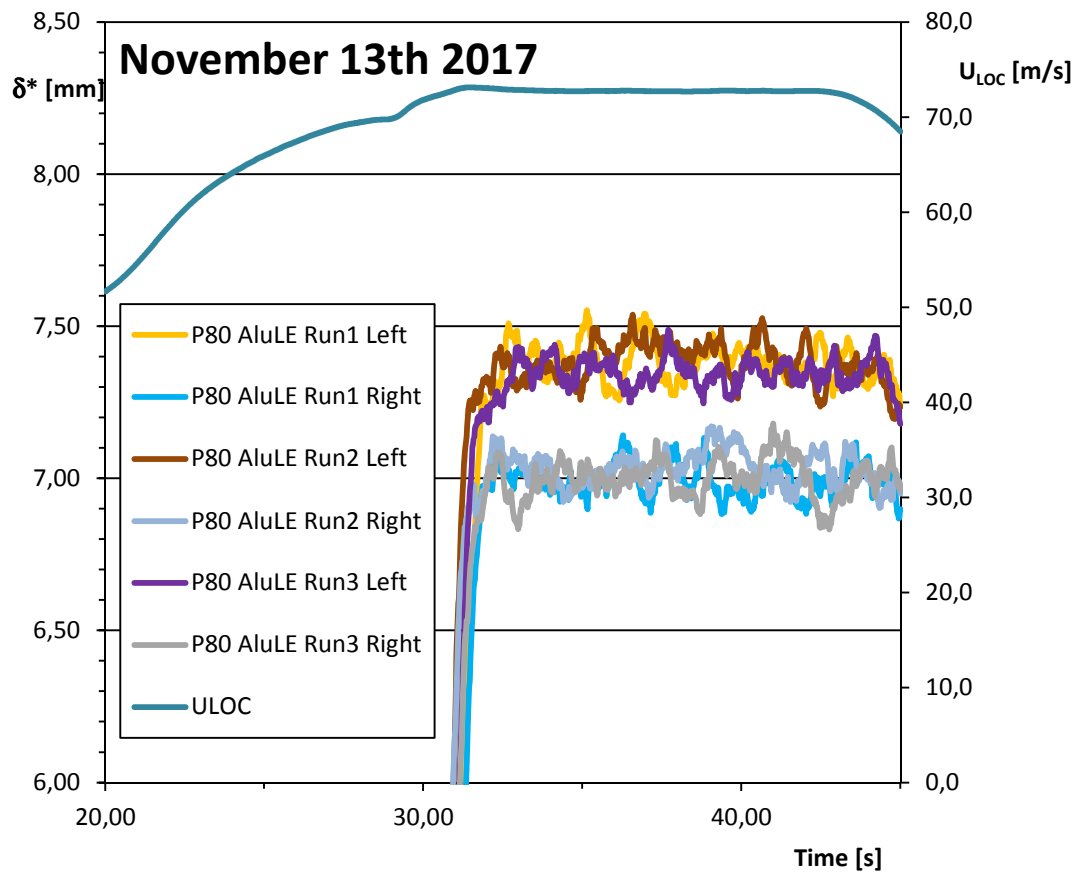
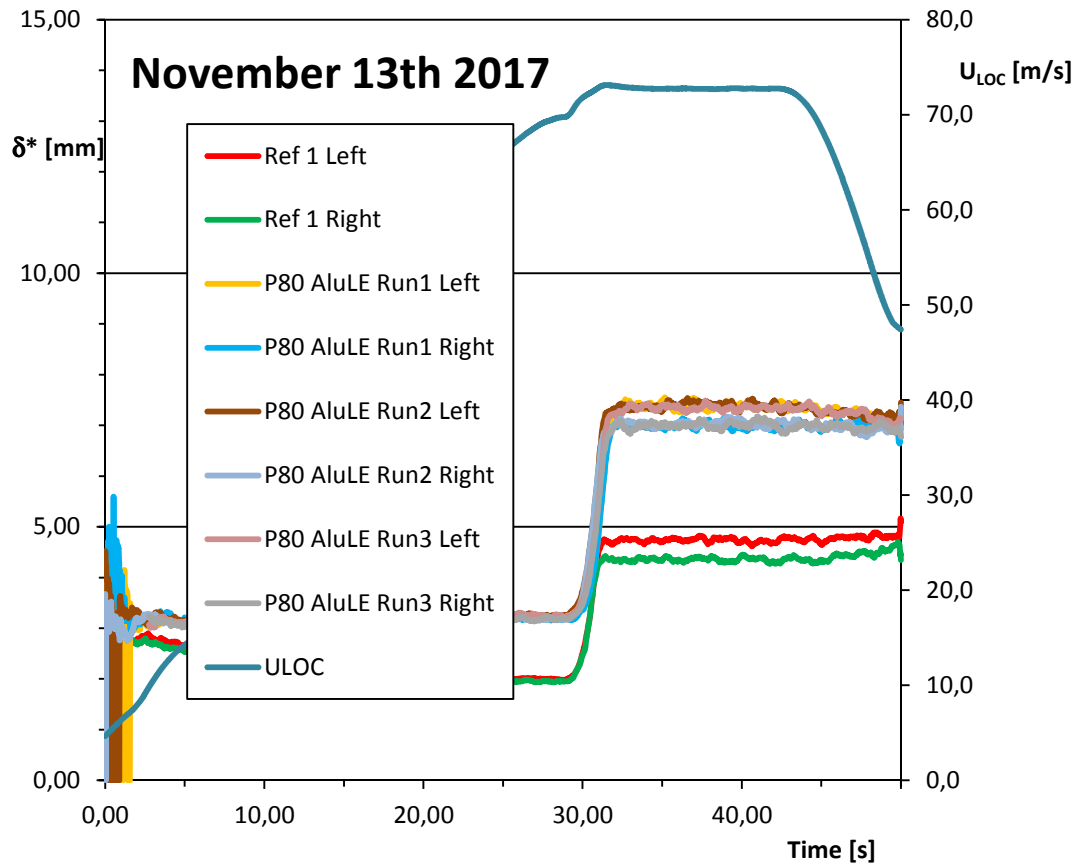


**Figure 47.** Boundary layer displacement thickness  $\delta^*$  as function of time during a simulated take-off with P80 sandpaper on the wing model.

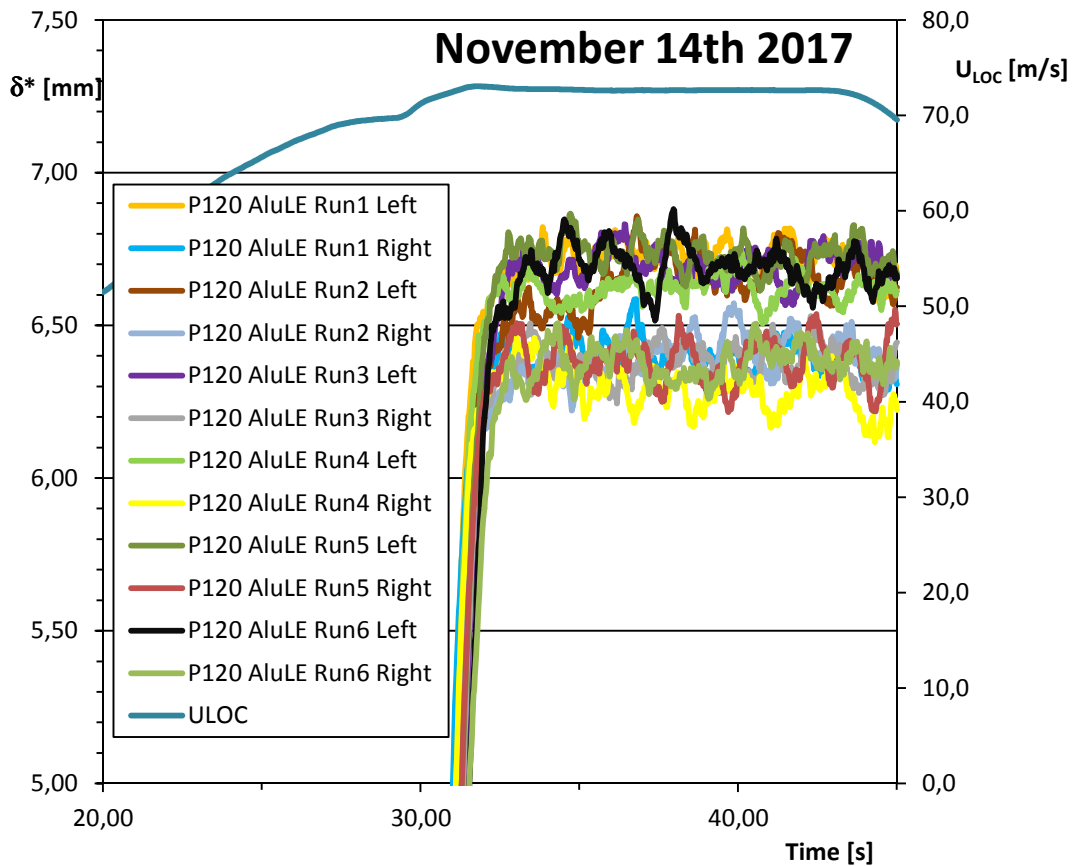
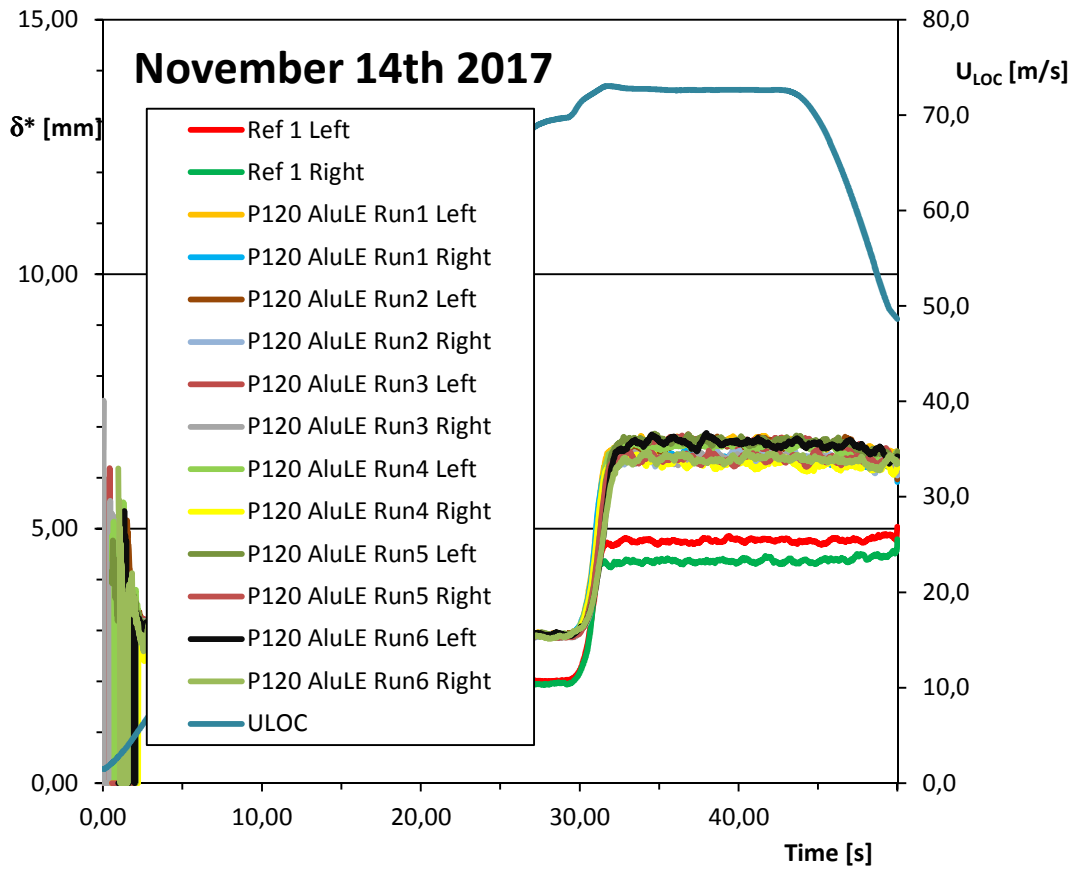


**Figure 48.** Boundary layer displacement thickness  $\delta^*$  as function of time during a simulated take-off with P120 sandpaper on the wing model.

### November 10th to 14th

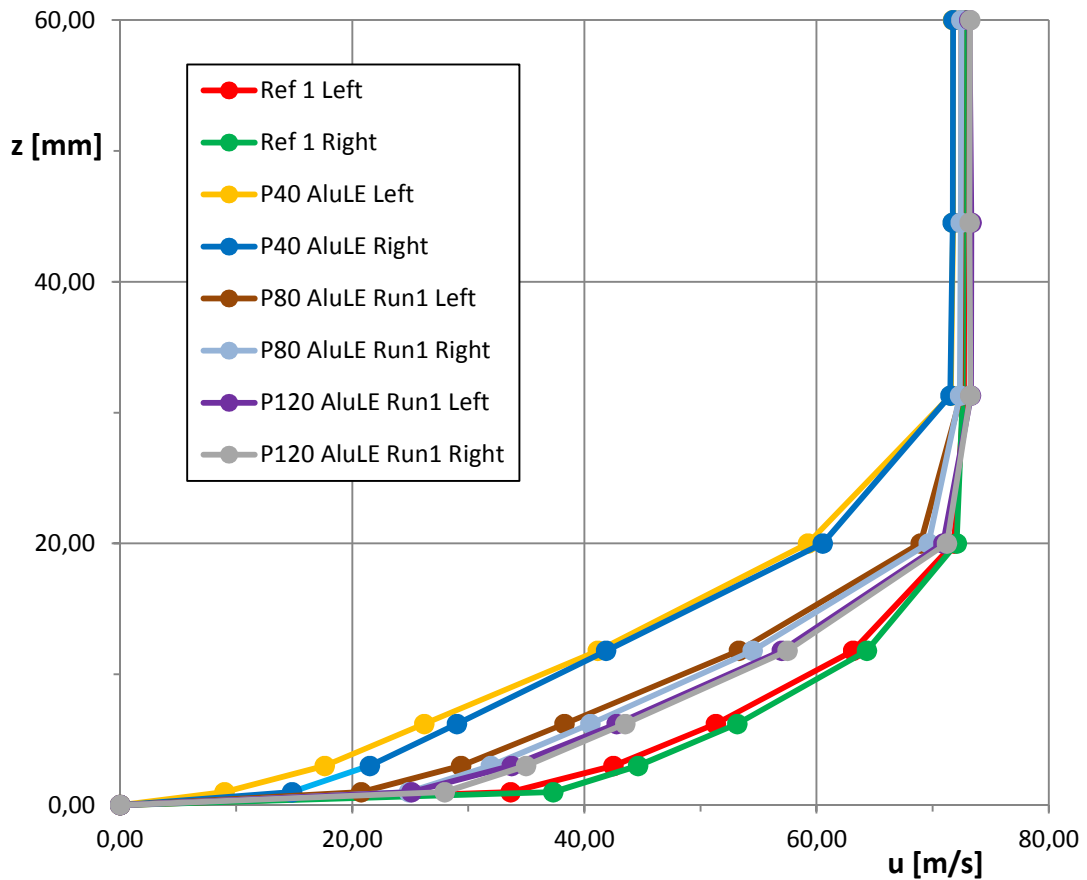


**Figure 49.** Boundary layer velocity profiles after wing model rotation.

$$\delta^* = \int_0^{\delta} \left(1 - \frac{u}{U_{LOC}}\right) dz \quad (3)$$

where  $U_{LOC}$  is the local flow speed at the boundary layer outer edge,  $u$  is the local flow speed in the boundary layer at normal distance  $z$  from the wing surface and  $\delta$  is the boundary layer thickness. The calculation of the displacement thickness is transformed into determining the area of the trapeziums defining the reduced flow due to the boundary layer. Consequently the calculated displacement thickness is slightly exaggerated, but derived in the same way in each calculation.

The results in Figure 46 show only small variations for the different sandpaper fore edge configurations. The average displacement thickness of the three wind tunnel runs with P40 sandpaper (including the one with the P120 Strip Failed) was  $\delta^*=11,80$  mm with a range of values  $\Delta\delta^*=0,77$  mm. For the wing model with P40 sandpaper and aluminum tape at the sandpaper fore edge the average displacement thickness was  $\delta^*=10,94$  mm. P40 sandpaper with a P120 strip and aluminum tape increased the displacement thickness slightly to  $\delta^*=11,48$  mm. The changes due to smoothing the sandpaper fore edge with aluminum tape and P120 strip do not follow the logical order of the effects on the lift coefficient. This may be an indication of the inaccuracy of the rake measurements.

Figure 47 shows three wind tunnel runs with P80 sandpaper and aluminum tape on the sandpaper fore edge. The average displacement thickness for the three runs was  $\delta^*=7,19$  mm with a range of values  $\Delta\delta^*=0,028$  mm which was well within the established repeatability.

The wind tunnel tests for the P120 sandpaper contained three runs (run 1, 2 and 3) with the nominal target angle of attack. Runs 4 and 5 tested different target angles of attack. Run 6 was made with the nominal target angle of attack but with a lower rotation rate, which did not show an effect on the attained displacement thickness. The average displacement thickness of the four runs was  $\delta^*=6,55$  mm with a range of values  $\Delta\delta^*=0,051$  mm, again well within the established repeatability.

The displacement thickness increase due to sandpaper was determined in the above mentioned figures by calculating the average boundary layer thickness during 5 seconds after the rotation with and without sandpaper on the wing. The difference on the left and right hand sides were calculated separately to filter the effects of the rakes. As the different sandpaper fore edge configurations had only a marginal effect on the lift coefficient, the results are summarized for the different grid types in Table 7. The change in the displacement thickness is the difference of the measured sandpaper value and the clean wing value. The displacement thickness increments on the left and right hand sides are almost the same. The inaccuracy of  $\pm 0,28$  mm on the difference of two measured displacement thickness values corresponds to 4...13% on the increment values shown in the table.

The dimensionless boundary layer displacement thickness increments due to the sandpapers are presented together with previous measurements of Cold Soaked Fuel Frost in Figure 50 as function of dimensionless surface roughness height, because this was the relevant parameter for lift loss. There was no noticeable evaporation/melting of the frost before rotation in the tested temperatures. The figure shows an increasing increment with increasing roughness but the P40 sandpaper results seem not to fit the linear trend as well as the other two sandpaper values. Figure 51 shows the relative lift reduction as function of the dimensionless boundary layer displacement thickness increment. Here a fairly linear trend of increasing lift loss is shown as function of the dimensionless displacement thickness increment, but the sandpaper and frost trends seem to have somewhat different slopes.

**Table 7.** Boundary layer displacement thickness and lift coefficient change for the sandpapers based on the measurements in Figure 43 to Figure 48.

Case	t/c	k/c	$\delta^*$ [mm]		$\Delta\delta^*$ [mm]		$\Delta\delta^*/c$	$\frac{\Delta C_L}{C_{L,Clean}}$
			Left	Right	Left	Right		
Clean wing	0	0	4,75	4,36	0	0	0	0
P40	0,00189	0,00068	12,10	11,49	7,35	7,13	0,01158	0,065
P80	0,00088	0,00032	7,38	7,01	2,63	2,65	0,00422	0,024
P120	0,00066	0,00020	6,70	6,39	1,95	2,03	0,00318	0,019

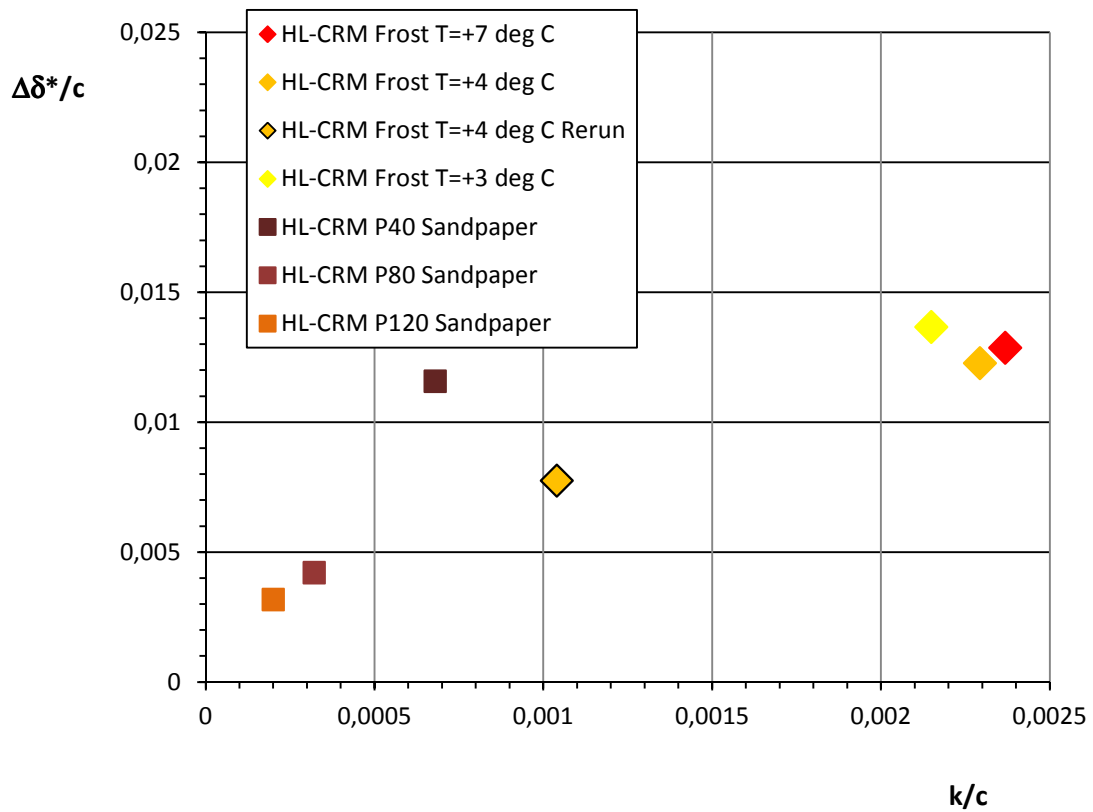


**Figure 50.** Dimensionless boundary layer displacement thickness increment as function of dimensionless surface roughness height (data also from ref. [2]).

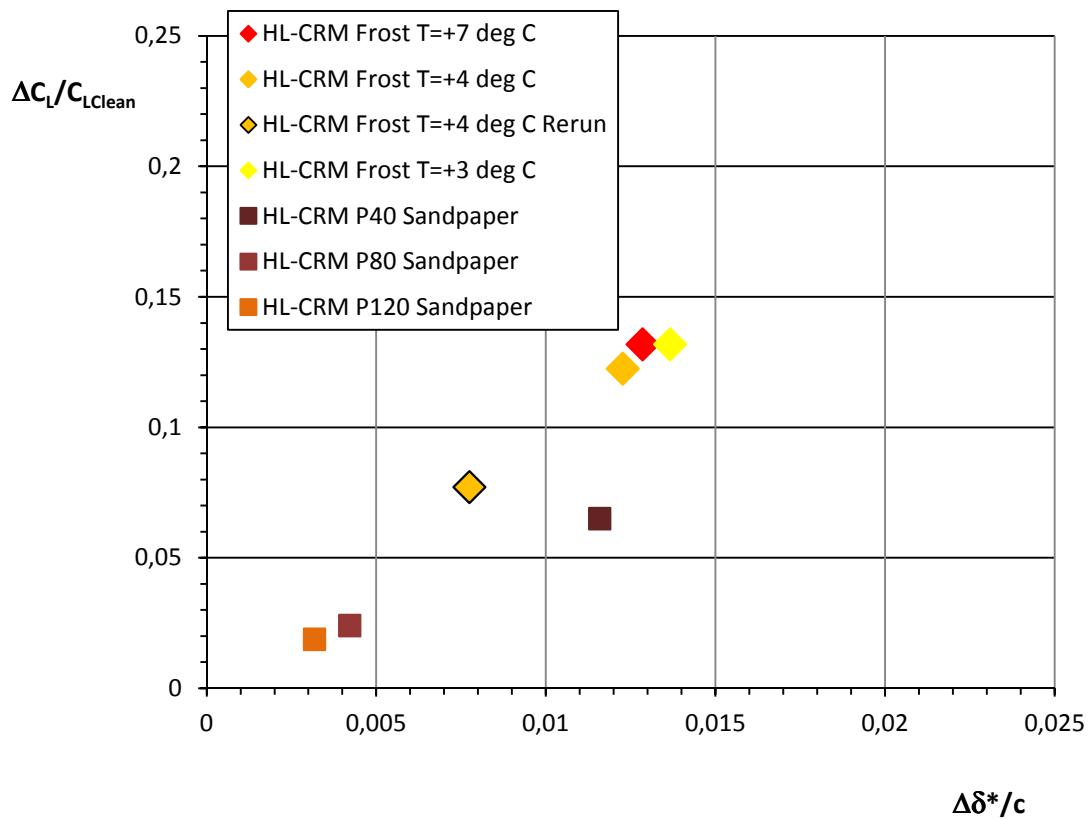


**Figure 51.** Relative Lift coefficient reduction as function of dimensionless boundary layer displacement thickness increment (data also from ref. [2]).

### 3.5 Anti-icing fluid measurements

The goal of the anti-icing fluid measurements was to check the typical lift reduction with fluids. Another goal was to correlate the lift reduction to boundary layer displacement thickness values. Both the boundary layer rake measurements at the main wing upper surface aft edge and the force balance measurements were simultaneously performed as time histories during the simulated take-off sequence. The interesting part is after rotation after which the fluid layer thickness is further diminished and the fluid effect is reduced.

The anti-icing fluid measurements were performed in two days using one fluid type per day, Type IV and Type II. Each day also clean wing reference measurements were done before and after the fluids measurements. Summaries of the fluids runs are presented in Table 8 and Table 9. The initial fluid thickness was measured with the Elcometer gauge. The target angle of attack in the wing model control system was  $5,9^\circ$ . For some reason Arteform did not record the displayed control system angles of attack.

**Table 8.** Type IV anti-icing fluid measurements on November 29th 2017.

Run	Description	$\alpha_i$ [°]
Ref 1	Clean wing reference run	
Ref 2	Clean wing reference run	
Type IV Run1	Initial fluid thickness 1,5 mm. The fluid went into the three lowest tubes.	
Type IV Run2	Initial fluid thickness 1,5 mm. The fluid went into the three lowest tubes.	
Ref after1	Clean wing reference run	
Ref after2	Clean wing reference run	
Ref after3	Clean wing reference run	
Ref after4	Clean wing reference run	

**Table 9.** Type II anti-icing fluid measurements on November 30th 2017.

Run	Description	$\alpha_i$ [°]
Ref 1	Clean wing reference run	
Ref 2	Clean wing reference run	
Type II Run1	Initial fluid thickness 1,2 mm. The three lowest tubes were plugged.	
Type II Run2	Initial fluid thickness 1,2 mm. The three lowest tubes were plugged.	
Ref after1	Clean wing reference run	

### 3.5.1 Lift coefficient

The clean wing measurements are collected into Figure 52 and Figure 53. It is noteworthy that the variation of the clean wing lift coefficient is considerably larger in the fluids measurements on November 29th than during the second day of fluids measurements or all previous sandpaper measurements. In the November 29th measurements the average value after the rotation of twenty measurement points (about 9 seconds) was for the lift coefficient  $C_L=1,541$  with a range of values 0,0197. In the November 30<sup>th</sup> measurements the corresponding average value was  $C_L=1,540$ , but the range was only 0,0047. During the sandpaper measurements the corresponding values for the clean wing were  $C_L=1,537$  and a range of 0,0089. The average value was virtually unchanged but for some reason the repeatability was degraded by about factor 2 in the November 29th measurements. The increased range gives for the lift coefficient an error of  $\pm 0,0098$ . The difference of two lift coefficients will have an inaccuracy of  $\sqrt{2} * 0,0098 = 0,0139$ . The range 0,0047 gives for the corresponding inaccuracy a value of  $\sqrt{2} * 0,00235 = 0,0033$ . The accuracy is as before on the repeatability of the lift coefficient, not on the absolute value.

The first day measurements with Type IV fluid are shown in Figure 54. During the second day the repeatability was back on the original good level and the results with the Type II anti-icing fluid on the wing are shown in Figure 55. The measurements with anti-icing fluids show after the rotation an increasing lift coefficient as the fluid thickness is reduced with time when the fluid is running off the wing model.

Before the rotation a varying lift coefficient is depicted in all figures as before. This is again due to the backlash in the mechanical system controlling the angle of attack. At higher angles of attack the system bottoms and this problem has not affected the lift force measurements after the rotation.

The lift reduction due to fluids was determined in the above mentioned figures by estimating visually the average lift coefficient after the rotation instant with and without fluid on the wing. The results are presented in Table 10 for relative lift degradation  $\Delta C_L / C_{L\text{clean}}$  as function of fluid initial dimensionless thickness. The above calculated inaccuracies of the clean wing and the fluid covered wing lift coefficient difference is for Type II fluid 9% and for Type IV 37%.

It is to be noted, that the fluid initial thickness is not the same as the thickness of a fluid wave formed during the fluid flow off. For this reason it is not meaningful to compare the lift reduction due to the fluid, based on the initial fluid thickness, with other surface contamination lift reductions based on contamination thickness. It has been argued that wind tunnel tests with fluids are not representative, because the fluid thickness cannot be scaled in the tests, see ref. [17] SAE ARP 6852 page 18. This is not quite true as the initial thickness of the fluid is dependent of the model size. The smaller the model is the smaller will the fluid initial thickness be due to the excess fluid running off the model. What is more important is that the lift reduction with the fluids is dependent on the fluid secondary wave. This wave comes from the fluid stored in the slat slot and/or in the low velocity area in the vicinity of the stagnation point when the wing is rotated during the

**Table 10.** Lift coefficient reduction for anti-icing fluids based on the measurements in Figure 54 and Figure 55.

Fluid	t/c	$C_{L\text{ clean}}$	$C_{L\text{ fluid}}$	$\Delta C_L$	$\Delta C_L / C_{L\text{ clean}}$
Type II	0,00240	1,541	1,482	0,0590	0,0383
Type IV	0,00192	1,541	1,483	0,0580	0,0376

take-off. The amount of the fluid in these areas depends on the model size, which actually scales the amount of the fluid available for the secondary wave.

The reduction of the two-dimensional lift coefficient is transformed into wing lift coefficient reduction in the linear range in proportion of the three and two-dimensional lift curve slopes. Consequently the absolute value of the wing lift coefficient reduction is lower than on the two-dimensional airfoil, but the relative reduction values are the same. As the selected wing section for the wind tunnel model is representative for the HL-CRM jet aircraft configuration the lift reduction is also representative for the aircraft.

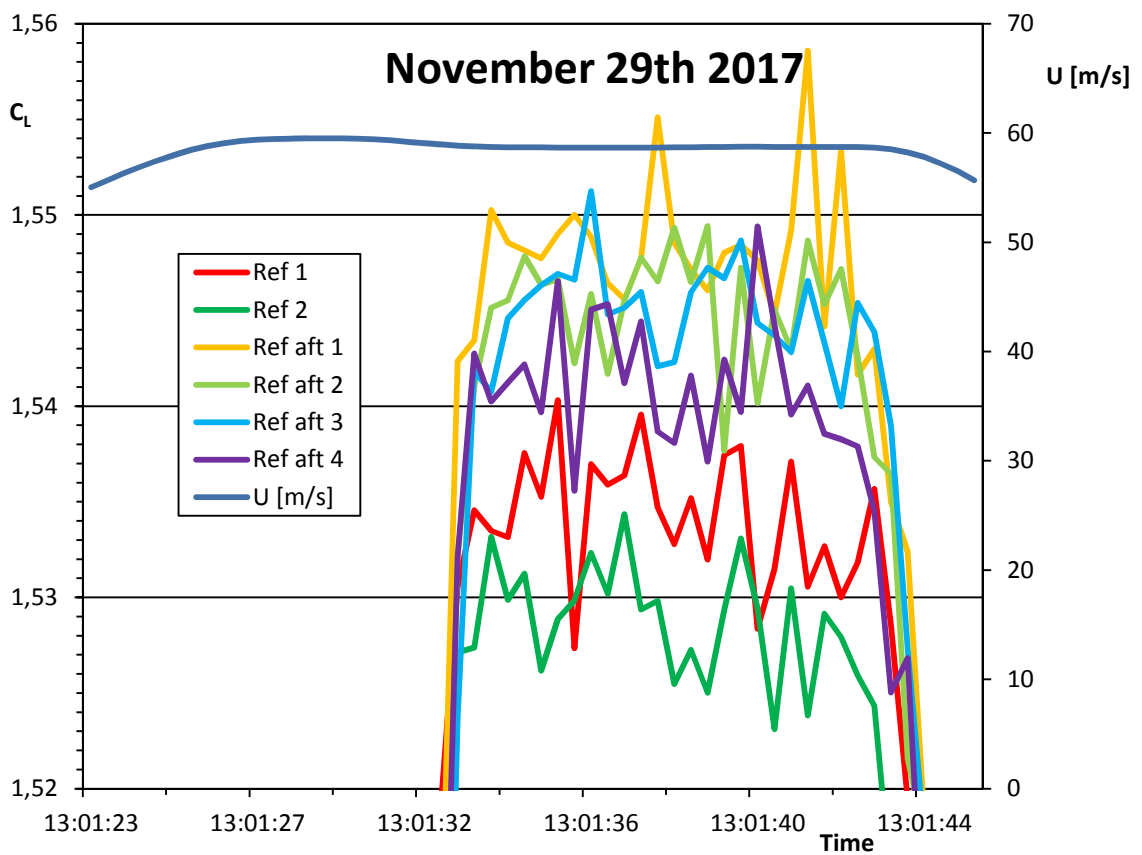
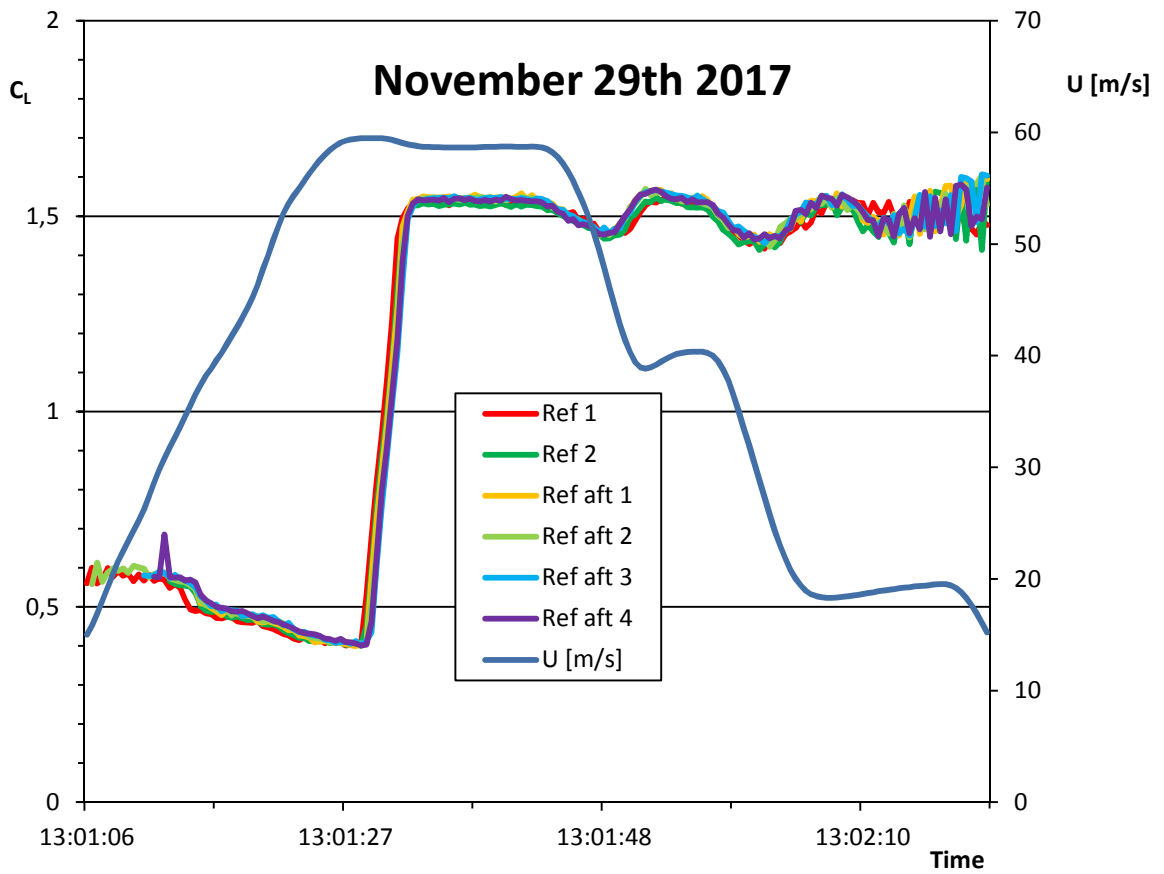


**Figure 52.** Lift coefficient  $C_L$  as function of time during a simulated take-off on a clean wing.

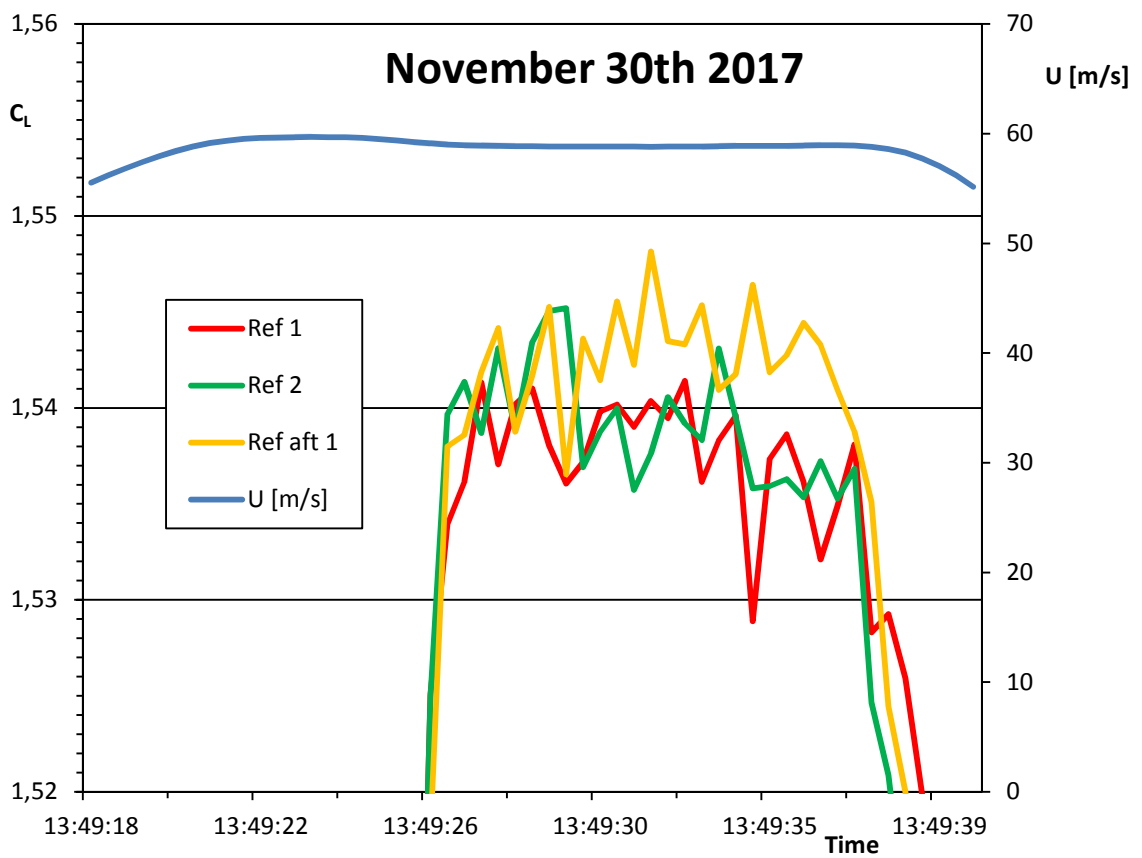
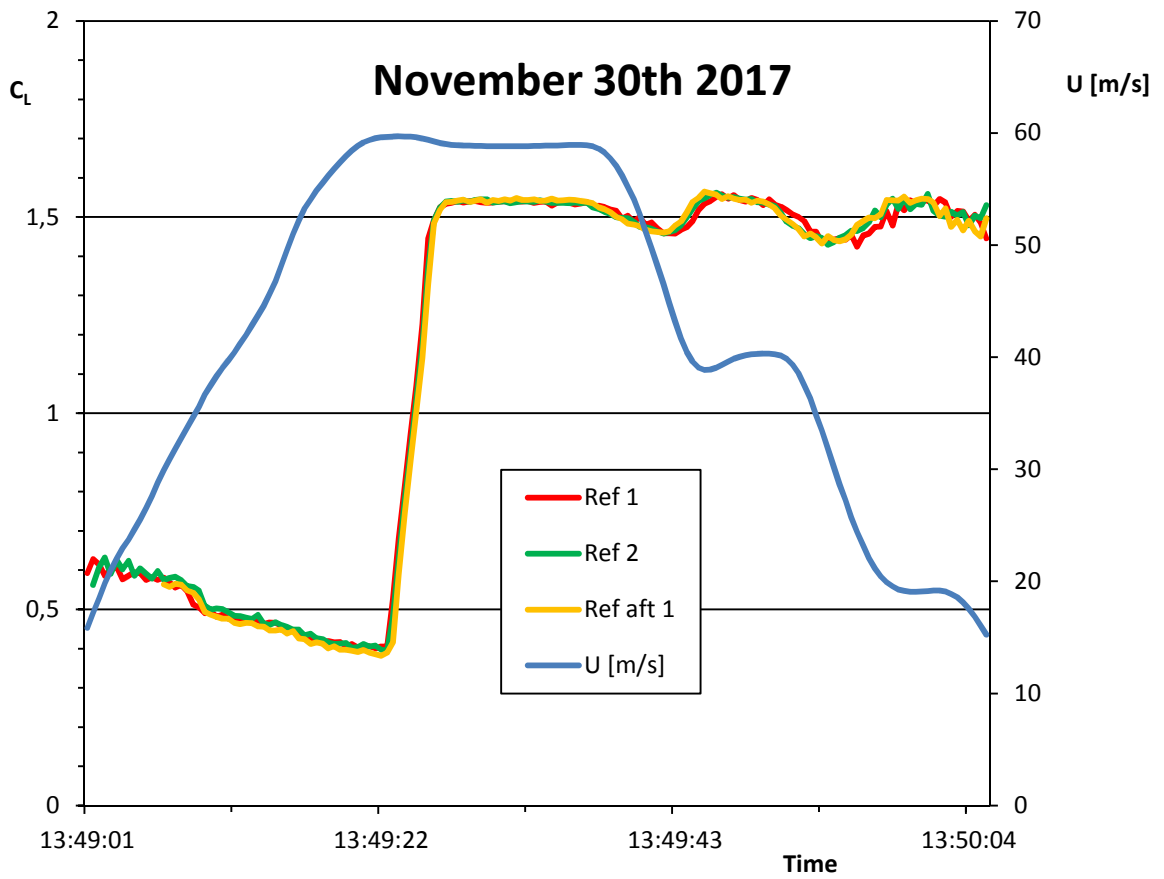


**Figure 53.** Lift coefficient  $C_L$  as function of time during a simulated take-off on a clean wing.

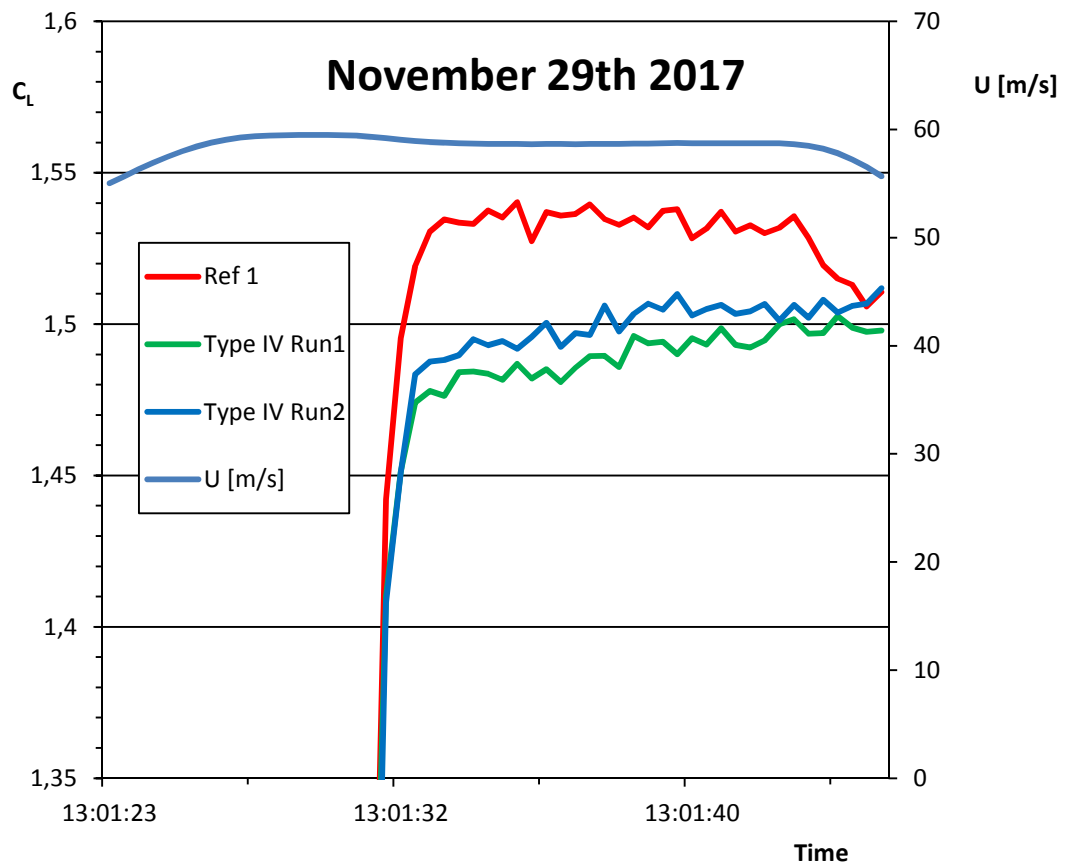
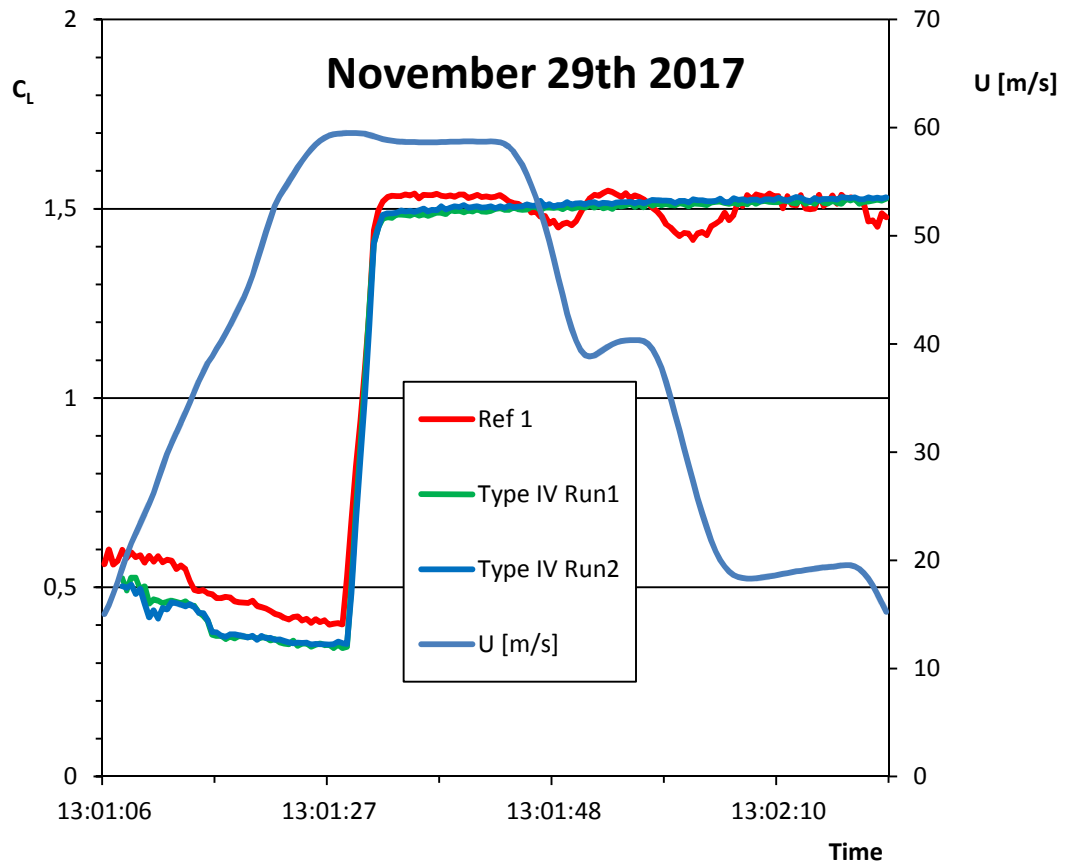


**Figure 54.** Lift coefficient  $C_L$  as function of time during a simulated take-off on the wing model with Type IV anti-icing fluid.

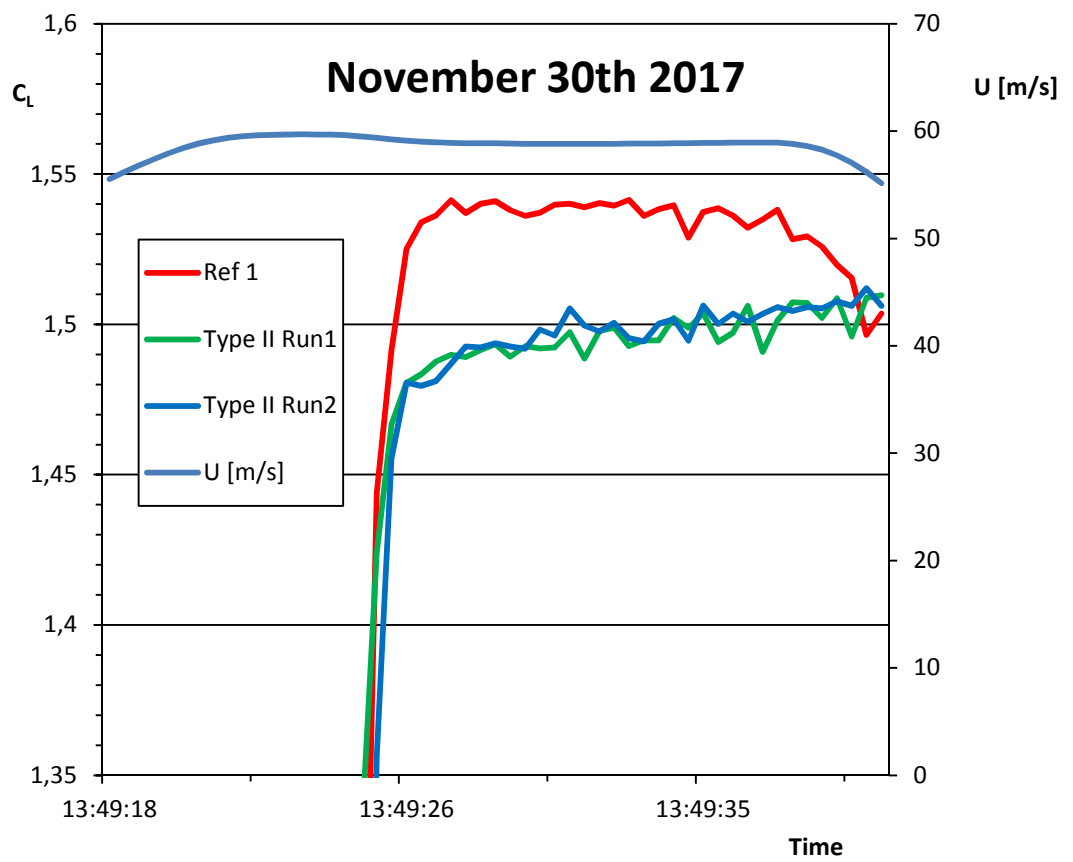
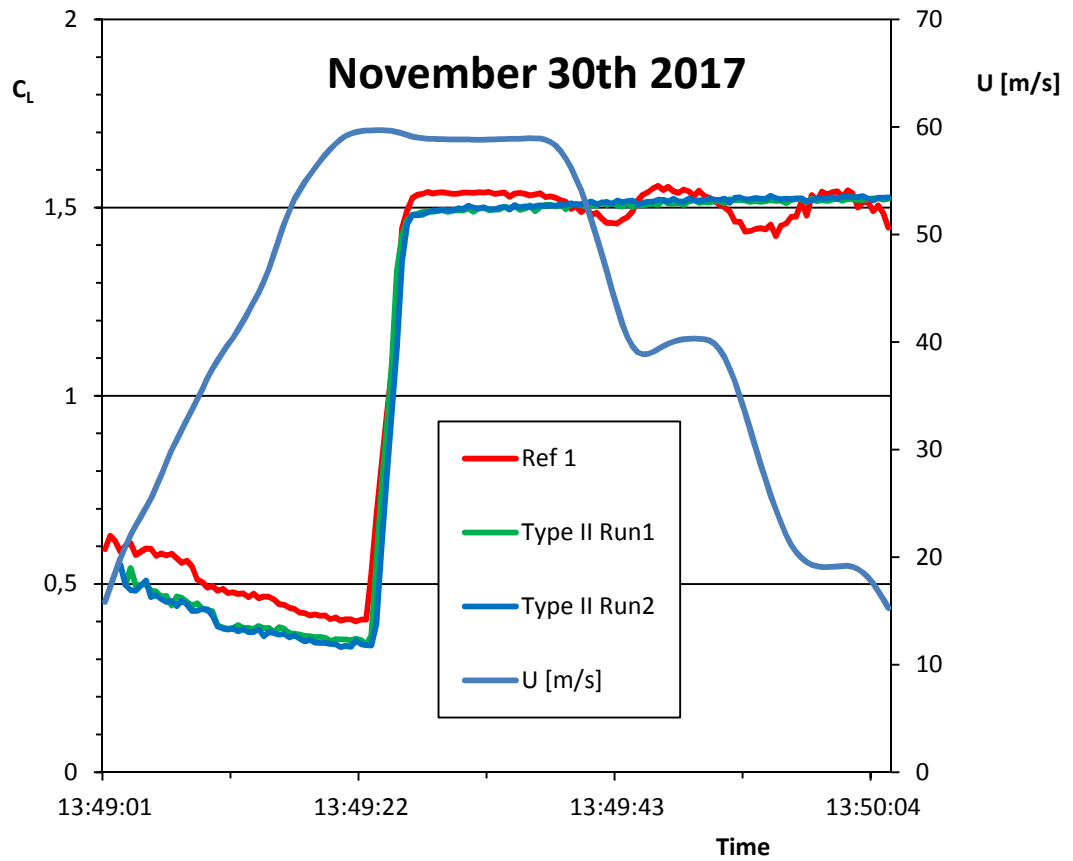


**Figure 55.** Lift coefficient  $C_L$  as function of time during a simulated take-off on the wing model with Type II anti-icing fluid.

### 3.5.2 Boundary layer displacement thickness

The boundary layer displacement thickness values, corresponding to the lift force measurements, were measured with two boundary layer rakes at the aft edge of the airfoil main element. The measurement interval was 0,02 seconds as previously and a moving averaging over 26 values, corresponding to a time period of 0,52 seconds, was performed to smooth out the measured pressures.

The measured boundary layer displacement thicknesses on clean wing are collected into Figure 56 and Figure 57. The measurements show again small variation after the rotation at constant angle of attack although the results should be the same. This is due to inaccuracies in pressure measurements, angle of attack after rotation and all other sources of possible variations. It is evident in the figures that the results of the left and right hand side rakes are grouped at slightly different levels of about 0,5 mm. Obviously the rakes are slightly different or are at slightly different levels from the wing surface or positioned in slightly different directions.

The average values of each curve after the rotation were calculated using 250 measurement points corresponding to a time period of 5 seconds. The average value of the clean wing displacement thicknesses of the 9 left hand side rake measurements gave after the rotation a value  $\delta^*=4,72$  mm. The range of the measured average values on the left hand side was  $\Delta\delta^*=0,21$  mm. The corresponding values in the sandpaper measurements were 4,75 mm and 0,17 mm. On the right hand side the average value was now  $\delta^*=4,19$  mm and the range of the measurements  $\Delta\delta^*=0,17$  mm. The corresponding values in the sandpaper measurements were 4,36 mm and 0,13 mm. The average value of the left and right hand side measurements was now  $\delta^*=4,46$  mm whereas the corresponding value during the sandpaper measurements was 4,56 mm so the repeatability seems to be good.

On one rake the repeatability seems to give a maximum deviation from the average value  $\Delta\delta^*=0,5*0,21=\pm 0,11$  mm. When calculating the difference of two boundary layer displacement thicknesses the inaccuracy was increased to  $\Delta\delta^*=\sqrt{2}*0,105=0,15$  mm. This is a very good repeatability when the displacement thicknesses are more than 4 mm for the clean wing and even more with the fluids. The absolute accuracy of the displacement thickness measurement was however less as the left and right hand side rakes give different results. The accuracy range was  $4,72-4,19+0,21=0,74$  mm and thus the maximum deviation was  $\pm 0,37$  mm, which is better than 10% on the clean wing displacement thickness.

Time histories of the boundary layer displacement thickness with Type IV and II fluids are presented in Figure 58 and Figure 59. It is seen in Figure 58 that before the rotation some of the rake pressure tubes were clogged as the calculated displacement thickness goes to zero. The reason for clogging is the primary wave of anti-icing fluid passing the rakes. After the rotation however, the displacement thicknesses are again displayed. The displacement thicknesses of the second run are though about 0,6 mm lower. In Type II fluid runs there is no clogging visible as the three pressure tubes closest to the wing surface were plugged.

The boundary layer velocity profiles just after the wing model rotation are presented for Type IV fluid in Figure 60. It is seen that the velocity profiles in the first run have the normal shape whereas in the second run there is a local inversion close to the wing surface. It seems that in the first wind tunnel run two pressure tubes were clogged during the wind tunnel acceleration, but after the rotation they have been again open and functioning normally. However, the fluid ingested in to the tubes during the first and second runs had partially clogged the two tubes in the second run. The velocity profiles for the Type II runs with plugged tubes are shown in Figure 61.

In Figure 60 are also shown fictitious velocity profiles for the first run with the three tubes closest to the surface plugged. The effect of this on the boundary layer displace-

ment thickness was  $\Delta\delta^*=1,99$  mm and 2,18 mm on the left and right hand sides respectively.

Time histories for the boundary layer displacement thickness of Type II fluid, shown in Figure 59, were measured with the three rake tubes closest to the surface plugged. The comparison of velocity profiles with Type II and IV fluids in Figure 62 shows a similarity motivating the correction of the plugged Type II results with the Type IV correction.

The results of Type II and IV fluid lift coefficient and boundary layer displacement thickness changes just after the rotation are collected into Table 11. On fluid Type II average values on both lift coefficient and displacement thickness were used. On Type IV the average value of the two lift coefficient measurements were used, but for the displacement thickness only the left and right hand side average of the first measurement was utilized as clogging was suspected to disturb the second rake measurement. The displacement thickness differences are calculated separately for the left and right hand sides to minimize the rake measuring system error. The measurement accuracy of  $\pm 0,37$  mm corresponds to an accuracy of about  $\pm 15\%$  of the increment value.

The relative lift coefficient reduction due to the fluids is shown as function of dimensionless boundary layer displacement thickness increment in Figure 63 together with results for sandpaper and Cold Soaked Fuel Frost. There was no noticeable evaporation/melting of the frost before rotation in the tested temperatures. Note that the two fluid values are almost on top of each other. The fluid values fit fairly well in the linear trend of the frost values. The sandpaper results also show a linear trend with somewhat different slope. Both trends indicate a lift loss approaching zero with the displacement thickness increment approaching zero, which feels physically correct.

**Table 11.** Boundary layer displacement thickness and lift coefficient change for anti-icing fluids based on the measurements in Figure 56 to Figure 59.

Case	$\delta^*$ [mm]		$\Delta\delta^*_{\text{Corr}}$ [mm]		$\Delta\delta^*$ [mm]		$\Delta\delta^*/c$	$\frac{\Delta C_L}{C_{L\text{Clean}}}$
	Left	Right	Left	Right	Left	Right		
Clean wing	4,72	4,19	0	0	0	0	0	0
Type II Plugged Run1	9,20	9,00	1,99	2,18	2,49	2,63	0,00412	0,0383
Run2	9,18	9,08	1,99	2,18	2,47	2,71		
Type IV Run1	7,30	6,70	0	0	2,58	2,51	0,00407	0,0376

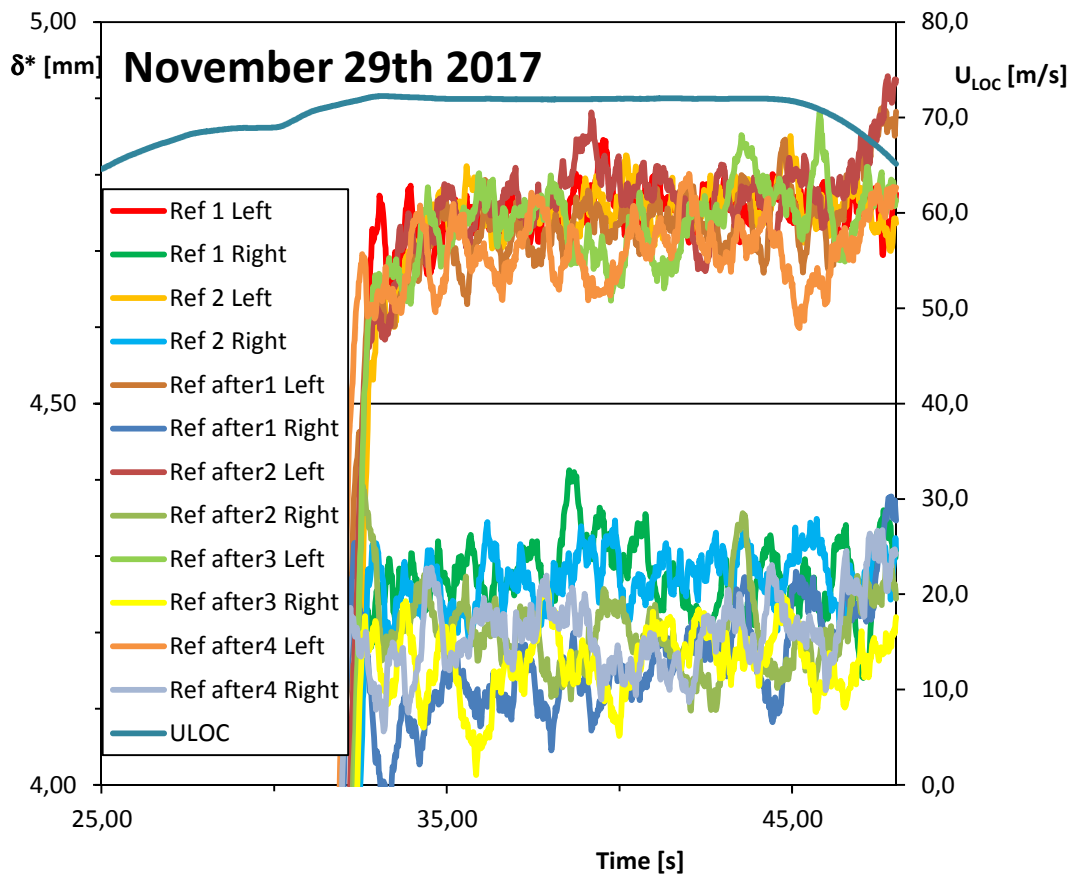
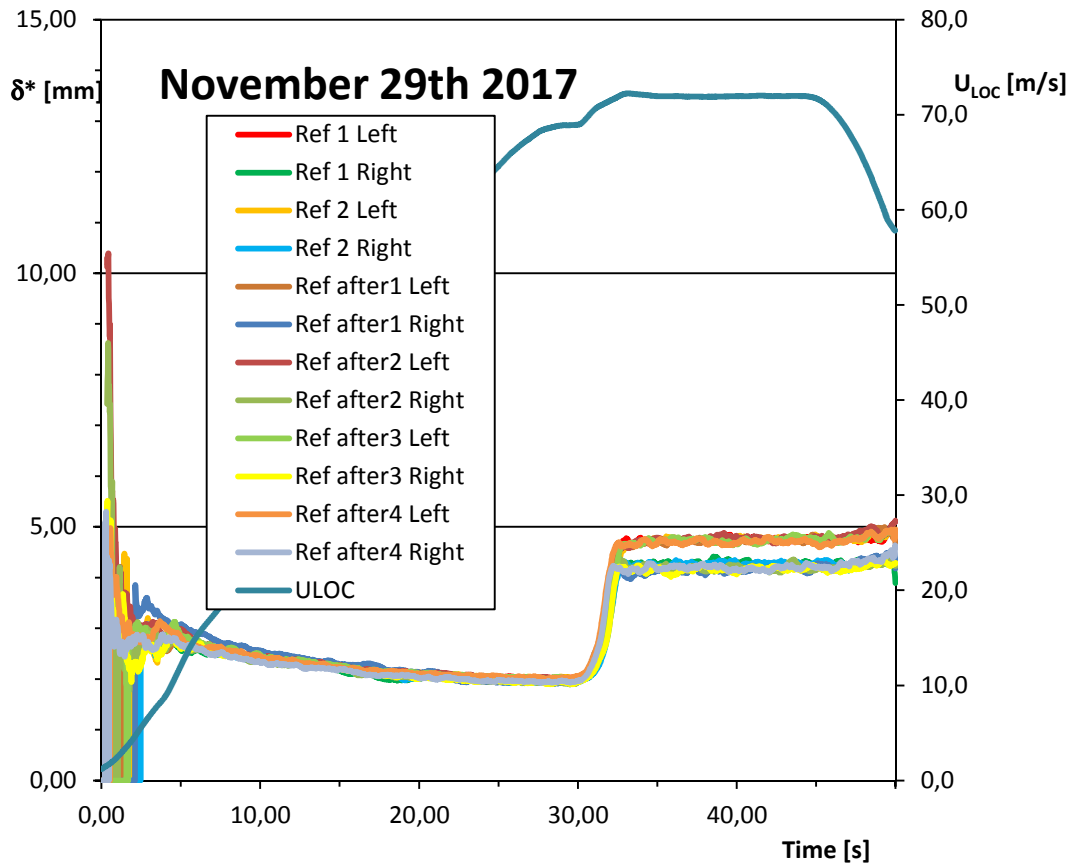


**Figure 56.** Boundary layer displacement thickness  $\delta^*$  as function of time during a simulated take-off on clean wing measurements.

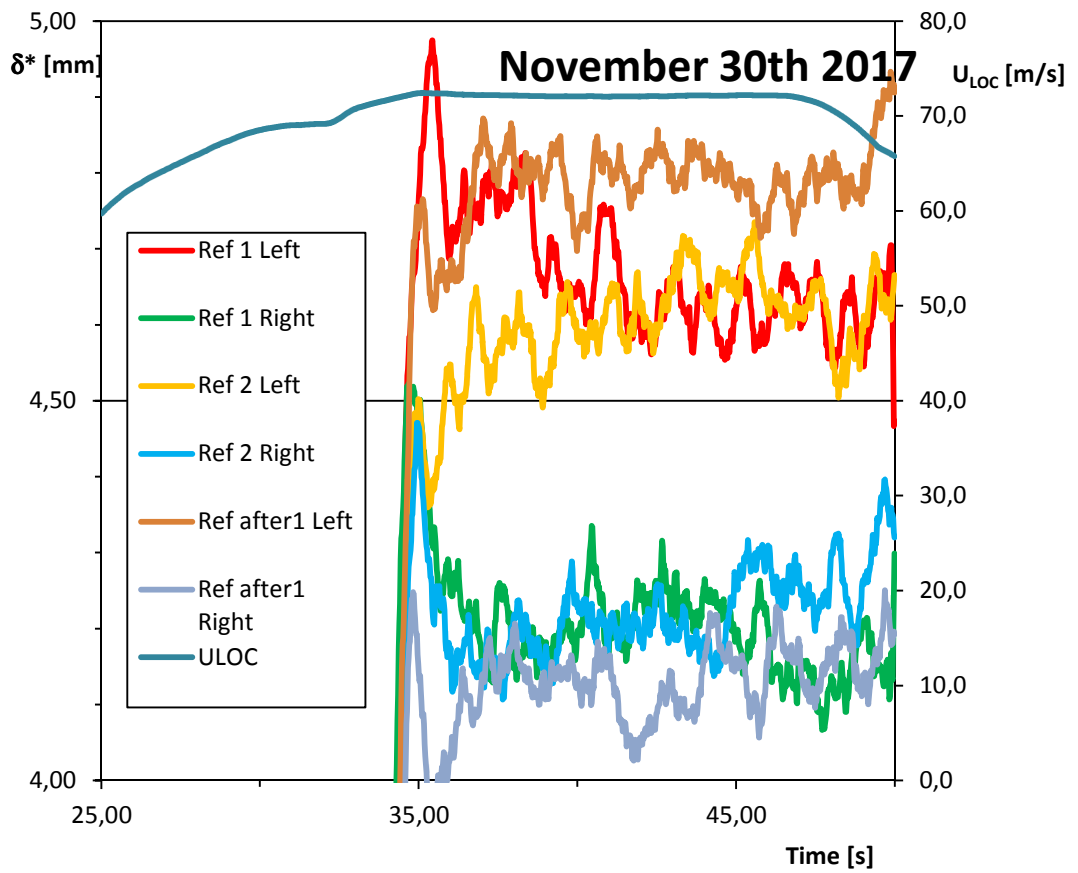
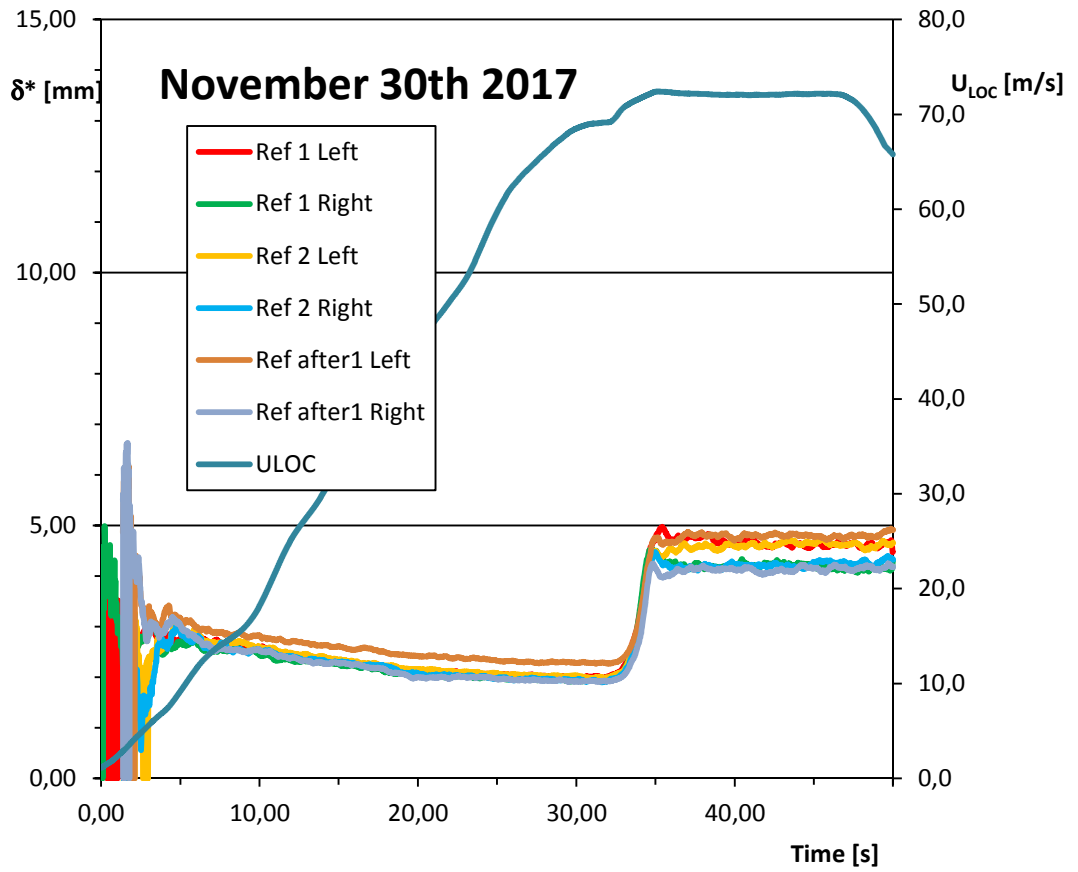


**Figure 57.** Boundary layer displacement thickness  $\delta^*$  as function of time during a simulated take-off on clean wing measurements.

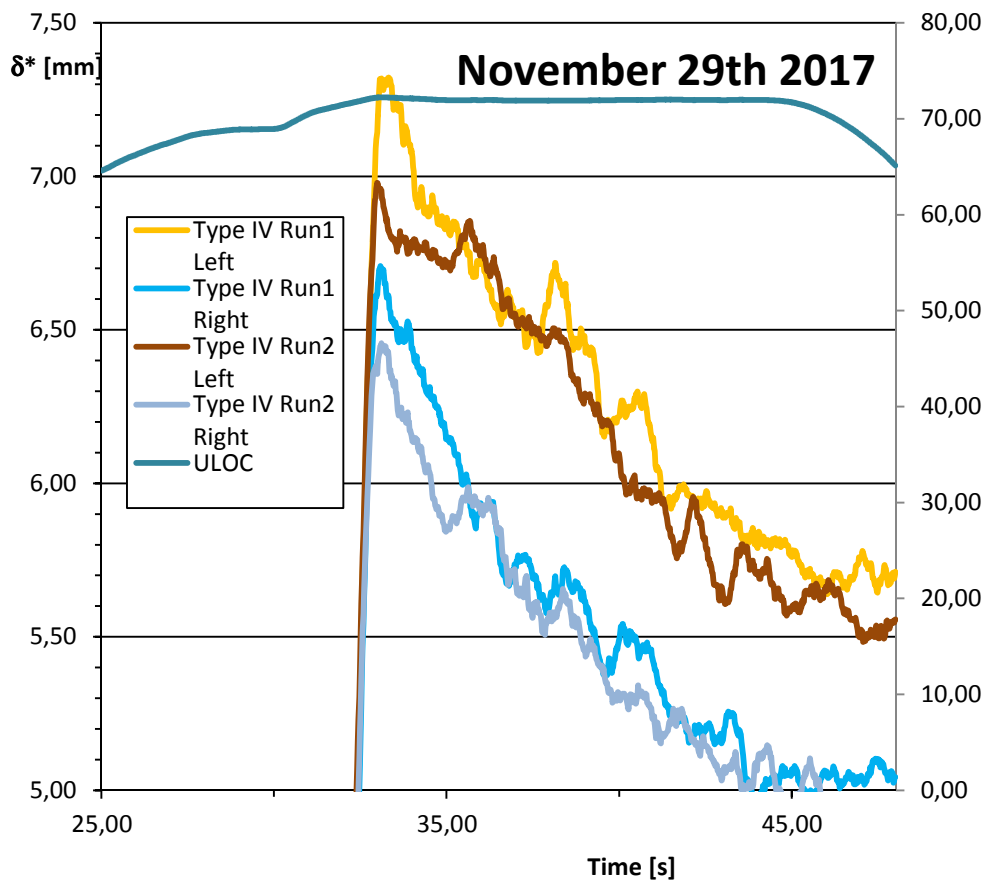
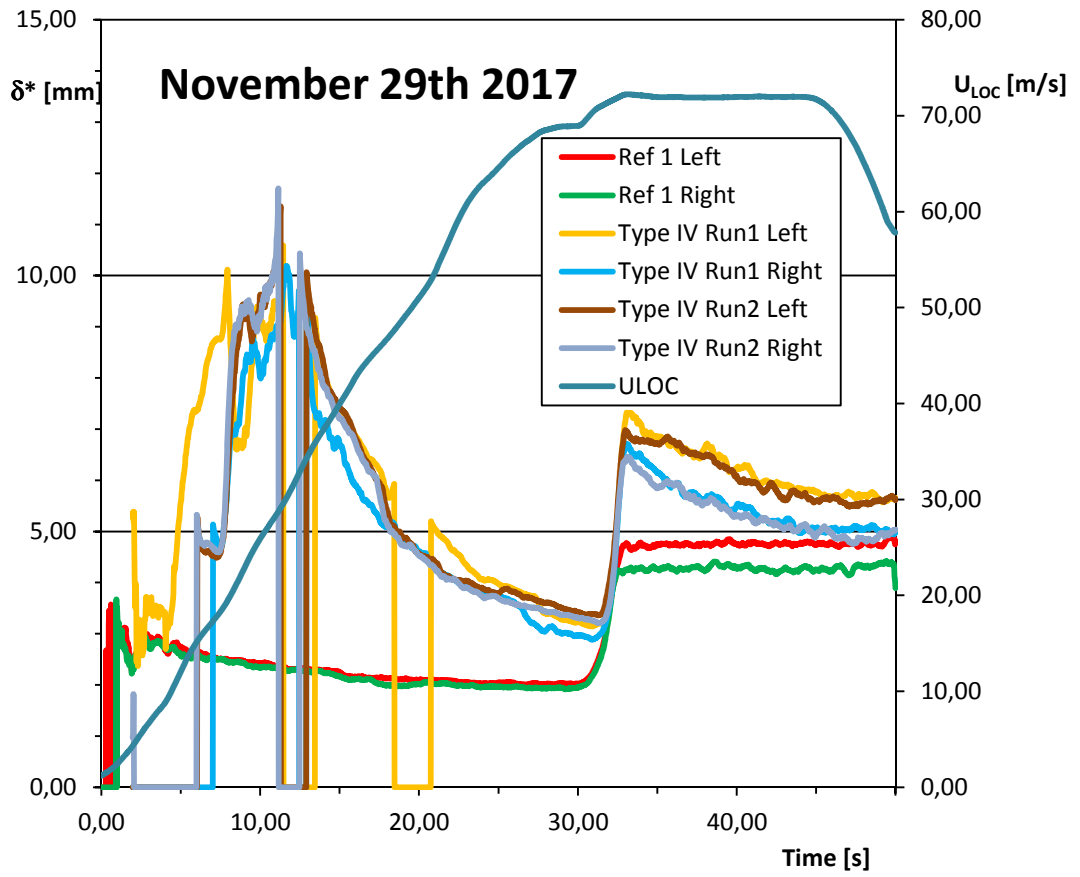


**Figure 58.** Boundary layer displacement thickness  $\delta^*$  as function of time during a simulated take-off with Type IV fluid on the wing.

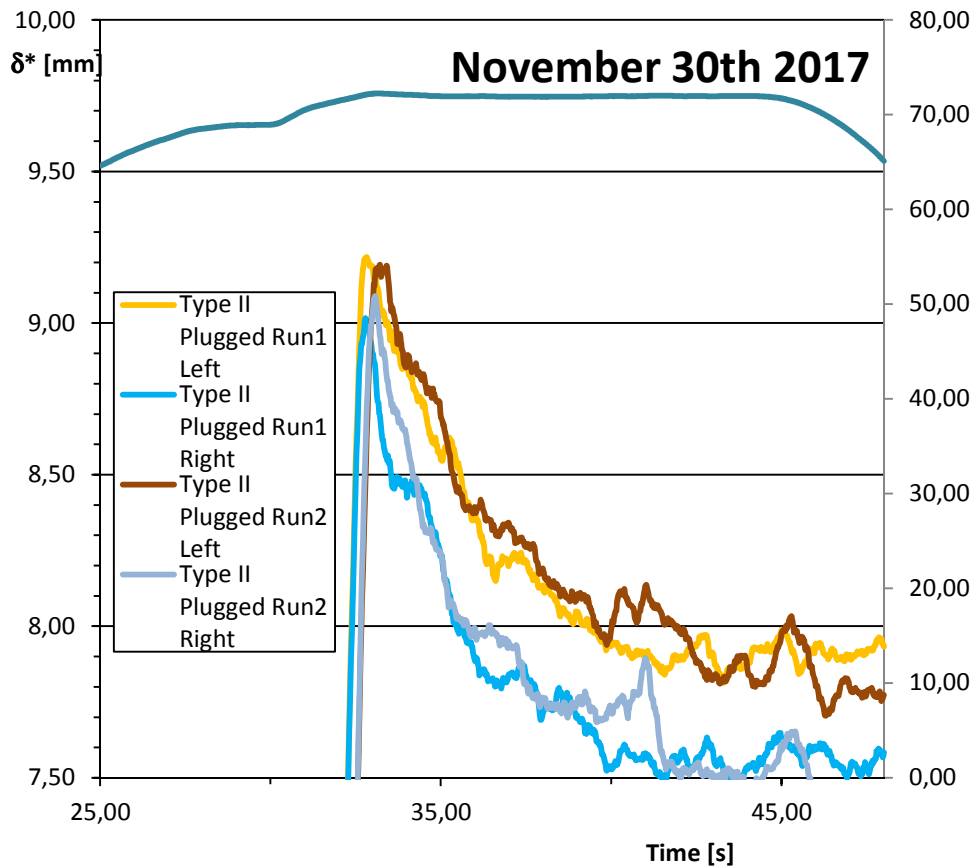
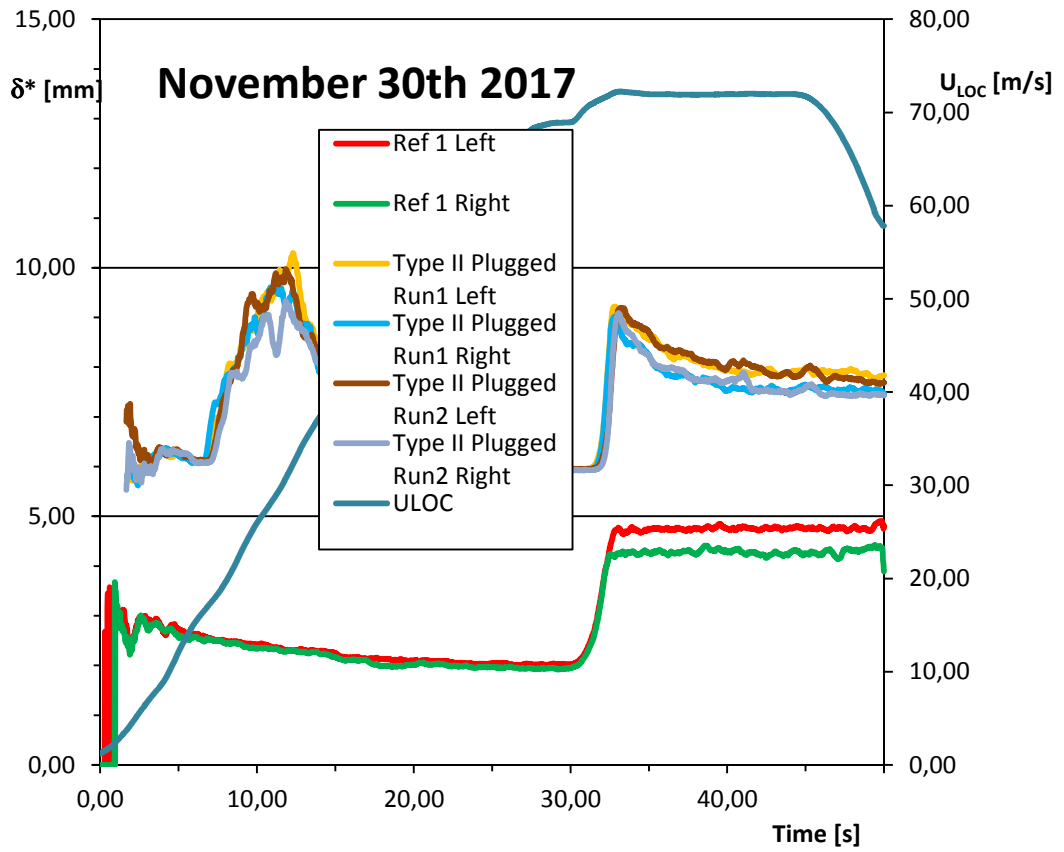


**Figure 59.** Boundary layer displacement thickness  $\delta^*$  as function of time during a simulated take-off with Type II fluid on the wing.

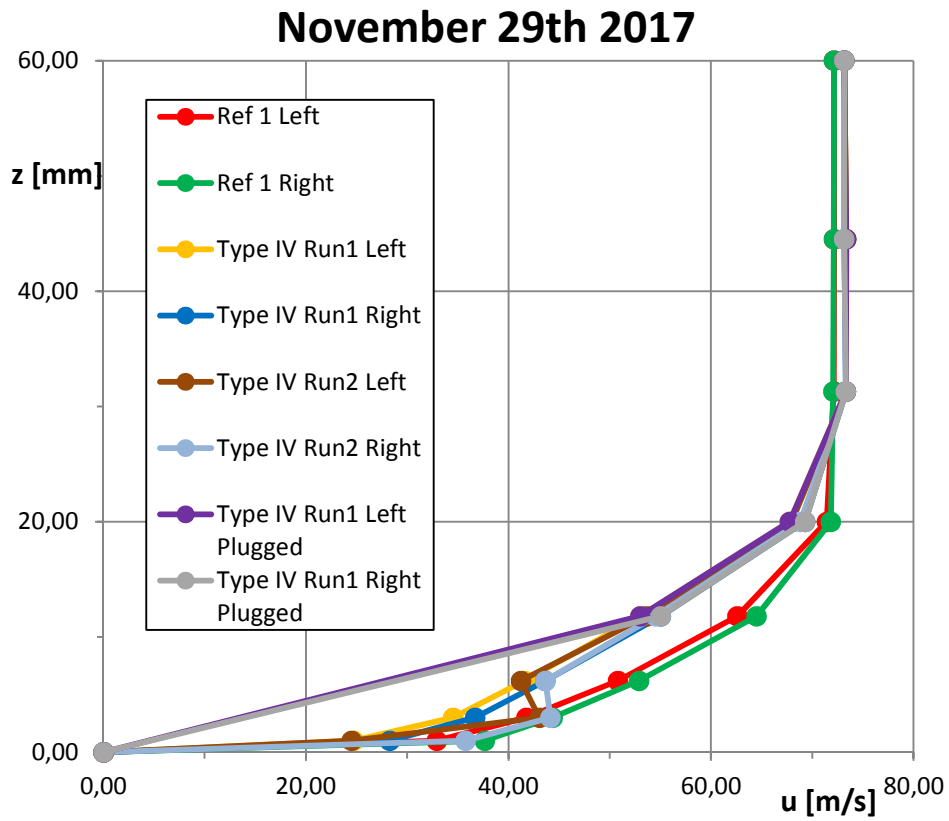


**Figure 60.** Boundary layer velocity profiles after wing model rotation.

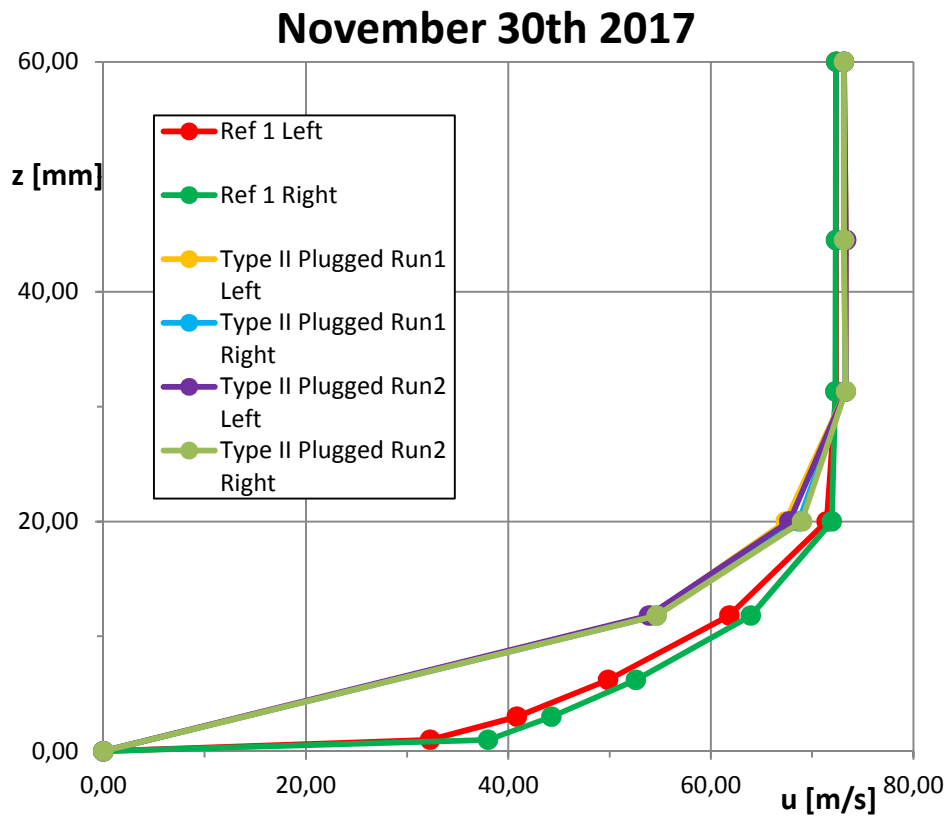


**Figure 61.** Boundary layer velocity profiles after wing model rotation.

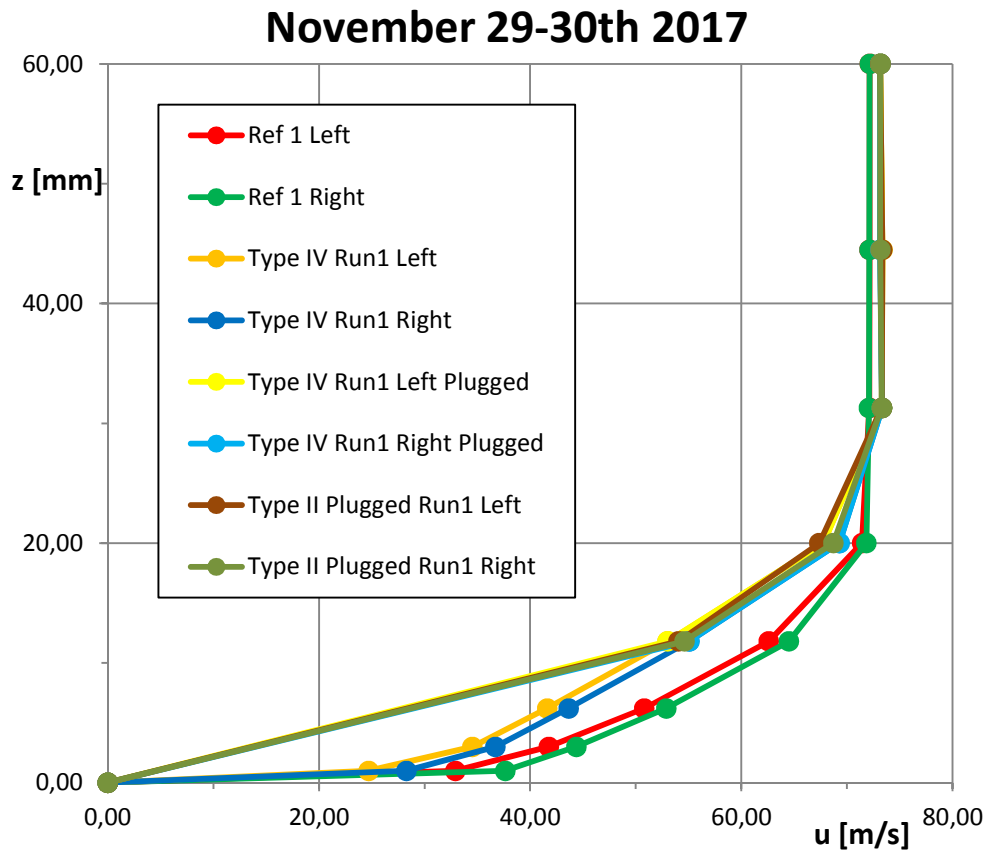


**Figure 62.** Boundary layer velocity profiles after wing model rotation.

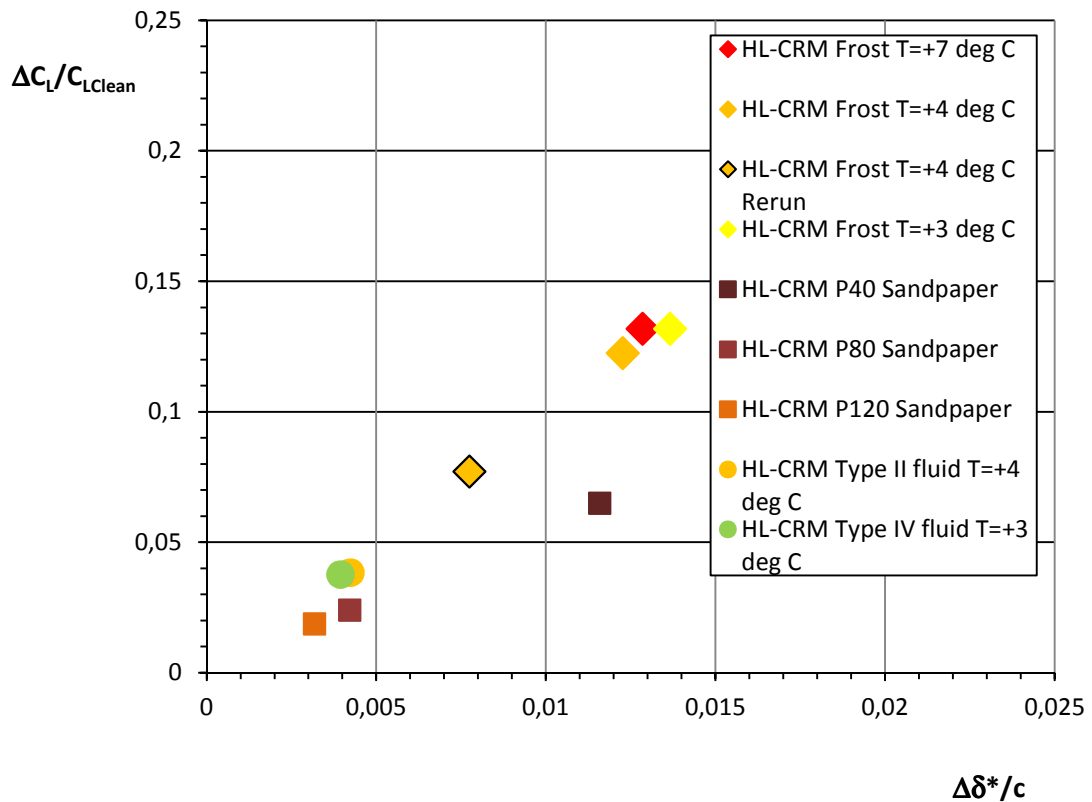


**Figure 63.** Relative Lift coefficient change as function of dimensionless boundary layer displacement thickness increment (data also from ref. [2]).

### 3.6 PVC plastic sheet measurements

The goal of the PVC plastic sheet measurements was to investigate the lift reduction due to an added smooth sheet to enable a separate study of the effects due to additional thickness and roughness. Another goal was to correlate the lift reduction to boundary layer displacement thickness values. The addition of a smooth layer introduces two effects. The first one is related to the step at the fore end of the sheet and its detrimental effect on boundary layer. The second one is due to the change in the airfoil upper surface contour. The addition of a relatively thin layer has an effect of increasing the airfoil thickness and camber. Increased thickness and camber change the pressure distribution in potential flow with an associated increase in lift. The effects of the step on the viscous boundary layer flow and potential flow are counteracting and the total effect may consequently be small.

Both the boundary layer rake measurements at the main wing upper surface aft edge and the force balance and were simultaneously performed as time histories during the simulated take-off sequence. The interesting part is after rotation and with a PVC plastic sheet the values are unchanged at constant angle of attack.

The complementary PVC plastic sheet measurements were performed during one day about a year after the sandpaper measurements. Clean wing reference measurements were performed before the PVC sheet measurements. A Summary of the PVC sheet runs is presented in Table 12. The target angle of attack in the wing model control system was  $5,9^\circ$ . This has in the past given an actual indicated control angle of attack  $\alpha_i$  from  $5,98^\circ$  to  $6,02^\circ$ . However, the control system has lately more often indicated an actual control angle of attack of  $6,37^\circ$ . During the October 29th measurements the control angle of attack display showed and angle of attack of  $6,37^\circ$ .

**Table 12.** Measurements of PVC plastic sheet on October 29th 2018.

Run	Description	$\alpha_i$ [ $^\circ$ ]
Ref 1	Clean wing reference run	6,37
Ref 2	Clean wing reference run	6,37
Ref 3	Clean wing reference run	6,37
Ref 4	Clean wing reference run	6,37 $^\circ$
PVC Sheet Run1	PVC Plastic sheet	6,37 $^\circ$
Run2	PVC plastic sheet	6,37 $^\circ$
Run3	PVC plastic sheet	6,37 $^\circ$

### 3.6.1 Measurement accuracy

The measurements October 29th 2018 showed constantly a rotation to an indicated angle of attack  $6,37^\circ$ . The lift coefficient values were checked by Trafic during the test day. The clean wing reference tests showed a corresponding average lift coefficient value of  $C_L=1,511$  with a range of  $\Delta C_L=0,00164$  for the four measurements. Consequently the repetition accuracy was good, but the average value during the March 2017 measurements was  $C_L=1,497$  (Ref. [2] Soenne et al page 49) and the October-November measurements 2017  $C_L=1,537$  to  $1,541$  (see Table 6 and Table 10). The change from the previous average values is larger than the maximum deviation from the present average value. The conclusion is that the accuracy in repetition is good but there is a level change from the previous values.

Before the PVC sheet measurements the CRM wing model was dismantled from the wind tunnel and stored half a year at the Trafic headquarters for display. For some unknown reason the attained angle of attack has slightly changed after mounting the model again into the wind tunnel test section. There should be no change as the model bottoms after the rotation and there is no mechanical backlash in the system. Arteform did not have an explanation for the lift coefficient level change. However, the change in lift coefficient level is small and the accuracy in repetition is good. This issue has no influence on the relative lift coefficient changes, which are calculated in per cent.

When the wing model was dismantled from the wind tunnel and then mounted again into the test section the boundary layer rakes were also again installed on the model. The reference tests on the clean wing model gave average values for the boundary layer displacement thicknesses  $\delta^*=5,32$  mm and  $\delta^*=4,63$  mm on the left and right hand sides respectively. The range of the four measurements was on both sides within  $\Delta\delta^*=0,02$  mm so the repetition accuracy was very good. In the March 2017 measurements the left and right hand side values were in the same group with only one value deviating. Consequently only an average value was calculated  $\delta^*=4,42$  mm (Ref. [2] page 50). In the November 10th to 14th 2017 clean wing measurements the average values on the left and right hand sides were  $\delta^*=4,75$  mm and  $\delta^*=4,36$  mm with the range of measurements on both sides within  $\Delta\delta^*=0,17$  mm (see page 50). In the November 29th to 30th 2017 measurements the average values on the left and right hand sides were  $\delta^*=4,72$  mm and  $\delta^*=4,19$  mm. The range of the 9 measurements was on both sides within  $\Delta\delta^*=0,21$  mm (see page 67).

Obviously the level of the measured clean wing boundary layer displacement thickness has changed with time and the difference between the left and right hand side measurements has increased. There is no physical reason for the difference, but the values should be the same. It has been speculated that the flexing of the slat and flap could be different on the left and right hand sides. It is unlikely that the structural flexure would be different and it would not change by time. The rakes may be slightly different in geometry and this may have changed during dismantling and mounting, but there is no solid proof for that. At present the cause of the differences is unknown. The differences between the left and right rakes can be minimized by calculating the displacement thickness increments separately for each rake. If the same boundary layer displacement thickness increment is obtained on the both rakes the system error is zero. For the sandpapers almost the same increments were obtained in Table 7 with a maximum difference of  $7,35-7,13=0,22$  mm. In the anti-icing fluid measurements the maximum difference was in Table 11  $2,47-2,71=-0,24$  mm. So the system error could be  $\pm 0,24$  mm. Calculating the increment separately for each side has reduced the system error from  $(5,32-4,63)/2=\pm 0,35$  mm to  $\pm 0,24$  mm. The total error is then  $0,21/2+0,24=\pm 0,35$  mm.

### 3.6.2 Lift coefficient

The measurement frequency of the force balance measurements was about 0,45 seconds. The clean wing measurements are collected into Figure 64. The measurements show a small variation although the result should be the same. This is due to inaccuracy in force measurement, angle of attack after rotation and all other sources of possible variations. The average values of twenty measurement points (about 9 seconds) after the rotation gave for the highest curve a value  $C_L=1,512$  and for the lowest  $C_L=1,510$  giving a range of average lift coefficient values of 0,0016. The range of the lift coefficient values is better than the corresponding numbers during the previous measurements 0,0097 in March 2017, 0,0089 in Nov 10 to 14 2017 and 0,0197 in Nov 29th and 30th 2017 measurements (ref. [2] Soinne et al page 43 and this report page 41 and 61).

The repeatability of the averaged lift coefficient values  $\pm 0,0008$  is well within the previously derived value  $\pm 0,006$  of ref. [1] Koivisto. The measured balance force values contain wind tunnel corrections for flow blockage due to the model and test section boundary layer but not due to flow curvature due to the wing model. Thus the accuracy is on the repeatability of the lift coefficient not on the absolute value.

When two values of lift coefficient are measured it is possible that the both errors have the same sign or opposite signs resulting in an error on the difference of 0 and 0,0016 respectively. Or the error on the difference could be some value in between. Assuming that the maximum errors act simultaneously in opposite directions is probably too conservative. However, it is likely that combining two inaccurate measurements cause a larger error than in a single measurement. Often a combined error, caused by several independent factors, is estimated using a root mean square value of the individual errors. The difference of two lift coefficients will then have an inaccuracy of  $\sqrt{2} * 0,0008 = 0,0011$ .

The lift coefficient time histories measured on a wing with the PVC sheet on the upper surface are shown in Figure 65. During the take-off roll before the rotation the lift coefficient should be constant as a constant angle of attack was specified. However, a varying lift coefficient is depicted. This is again due to a backlash in the mechanical system controlling the angle of attack. At higher angles of attack the system bottoms and this problem has not affected the lift force measurements after the rotation.

The lift reduction due to PVC plastic sheet was determined in the above mentioned figures by calculating the difference of the clean wing and PVC sheet covered wing average values of the twenty measurement points after the rotation. The results are summarized in Table 13. The inaccuracy of the lift coefficient difference of 0,0011 gives an inaccuracy of 16% for the difference of 0,007 shown in the table.

The results are presented as relative lift degradation  $\Delta C_L / C_{L, \text{Clean}}$  as function of relative thickness and roughness as this dimensionless presentation permits direct comparison with different airfoils and wings. The absolute reduction of the two-dimensional lift coefficient is transformed into wing lift coefficient reduction in the linear range in proportion of the three and two-dimensional lift curve slopes. Consequently the absolute value of

**Table 13.** Lift coefficient reduction for the PVC plastic sheet based on the measurements in Figure 64 and Figure 65.

Case	t/c	k/c	$C_L$ Clean	$C_L$ PVC Sheet	$\Delta C_L$	$\Delta C_L / C_{L, \text{clean}}$
PVC plastic sheet	0,00205	0	1,511	1,503	0,007	0,005

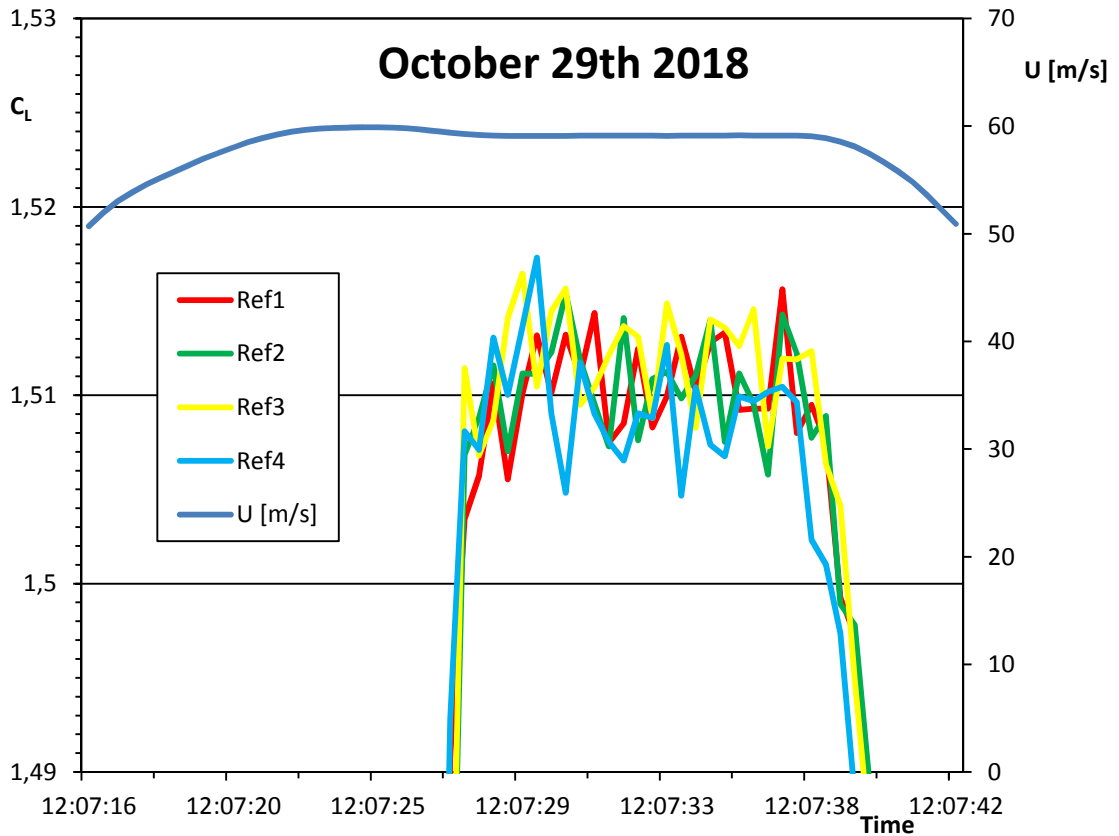
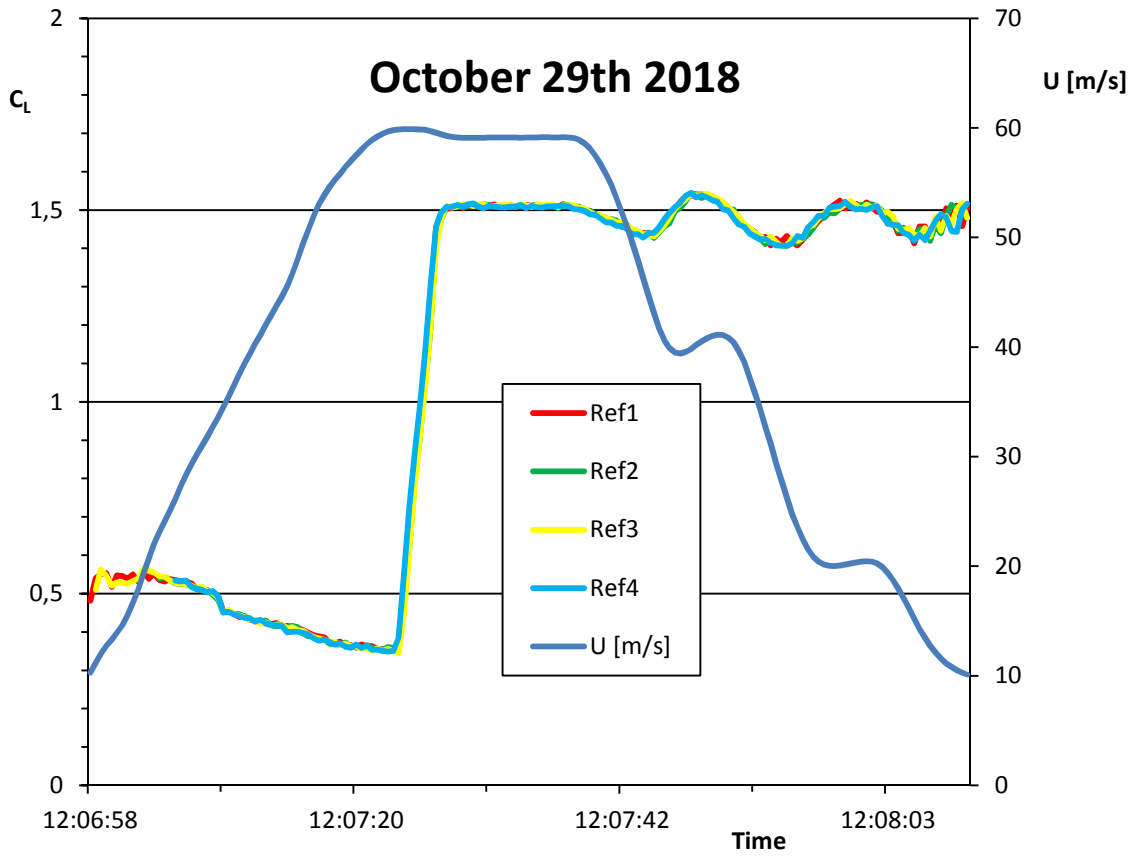


**Figure 64.** Lift coefficient  $C_L$  as function of time during a simulated take-off on a clean wing during the measurements on October 29<sup>th</sup>.

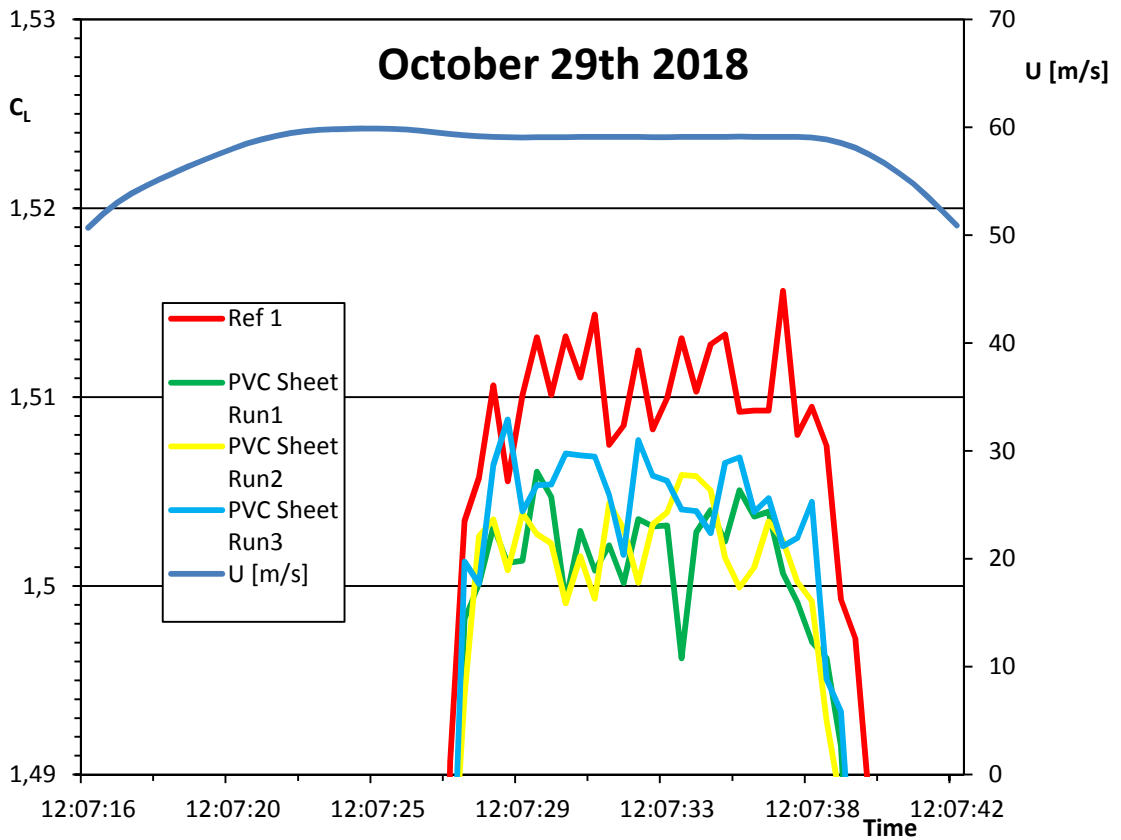
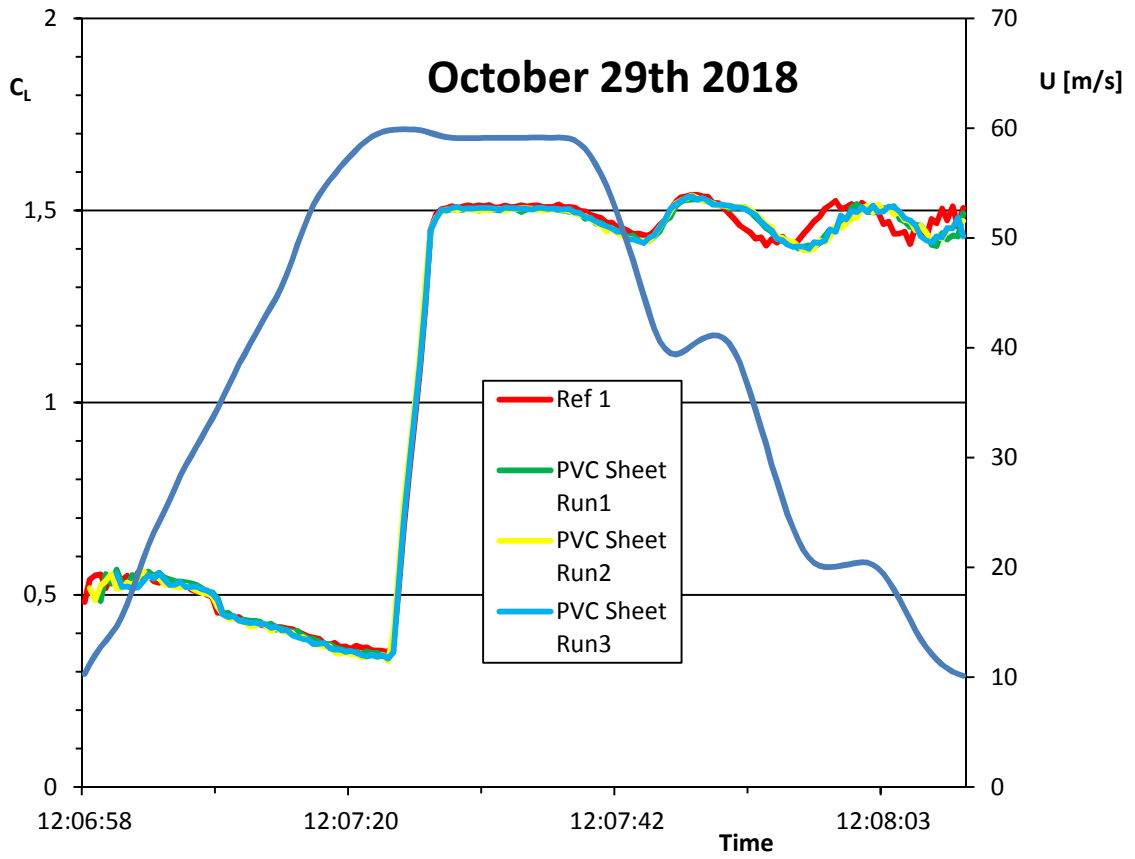


**Figure 65.** Lift coefficient  $C_L$  as function of time during a simulated take-off of PVC plastic sheet measurements.

the wing lift coefficient reduction is lower than on the two-dimensional airfoil, but the relative reduction values are the same. As the selected wing section for the wind tunnel model is representative for the HL-CRM jet aircraft configuration the lift reduction is also representative for the aircraft.

Broeren&Riley in ref. [18] point out on page 14 that the trends on percentage lift losses in two-dimensional flow at linear lift range and three-dimensional flow at maximum lift may be different. This refers to the 5,24% maximum lift reduction, that Hill&Ziarten ref. [10] considered acceptable. Now the FAA policy ref. [15] is based on the liftoff lift coefficient reduction which is in the linear lift range and the transformation to maximum lift has become obsolete.

A reason for inaccuracy in lift coefficient reduction is the Reynolds number in the present tests being different from full scale aircraft take-off situation. The allowable frost thickness should be confirmed with three-dimensional wind tunnel or flight testing for the aircraft configuration in question.

The PVC plastic sheet effect on lift reduction is presented in Figure 66 and Figure 67 together with previous measurements on Cold Soaked Fuel Frost, sandpaper and anti-icing fluids results. There was no noticeable evaporation/melting of the frost before rotation in the tested temperatures. The first figure shows that the PVC sheet value sticks out of the group of other measured values when presented as function of dimensionless thickness. In the second figure the PVC sheet value fits fairly well the linear trend of growing lift loss, when presented as function of dimensionless roughness height. It seems that for a PVC sheet the effect of thickness increase is not significant, but the lift reduction is due to the fore edge step and its detrimental effect on the boundary layer.

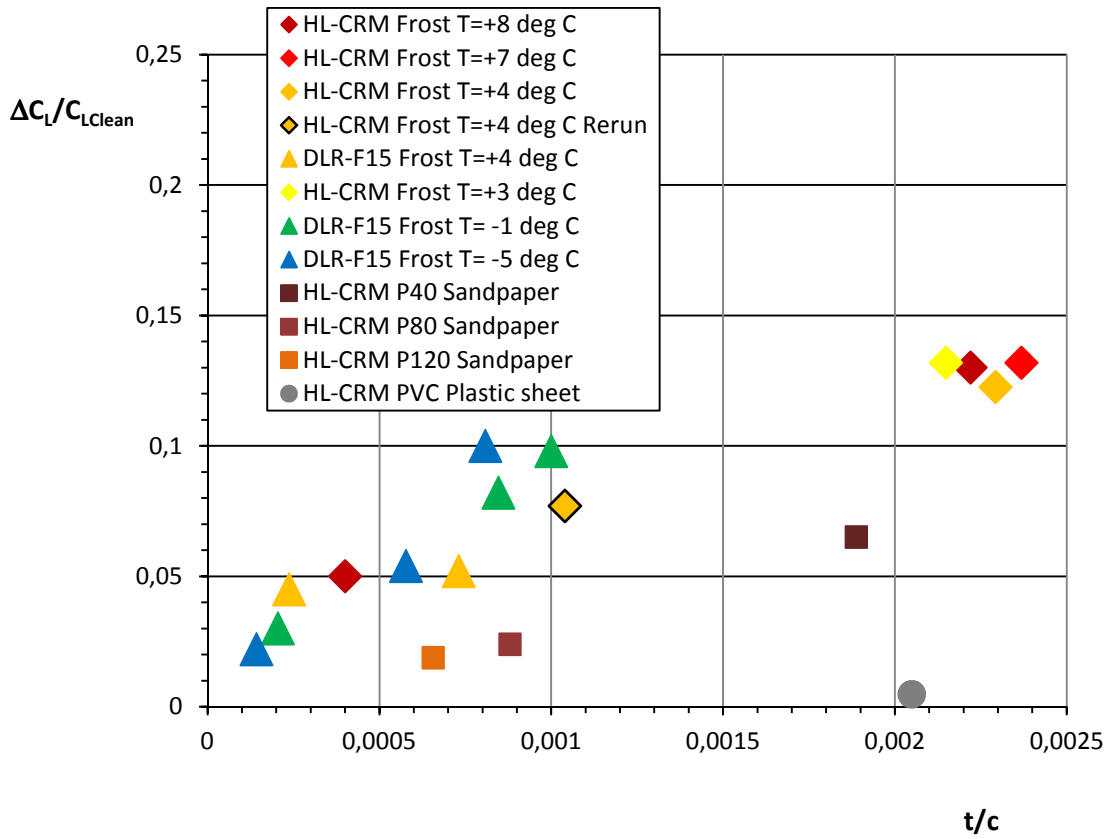


**Figure 66.** Relative Lift coefficient reduction as function of surface roughness added dimensionless thickness (data also from ref. [1], [2] and [16]).

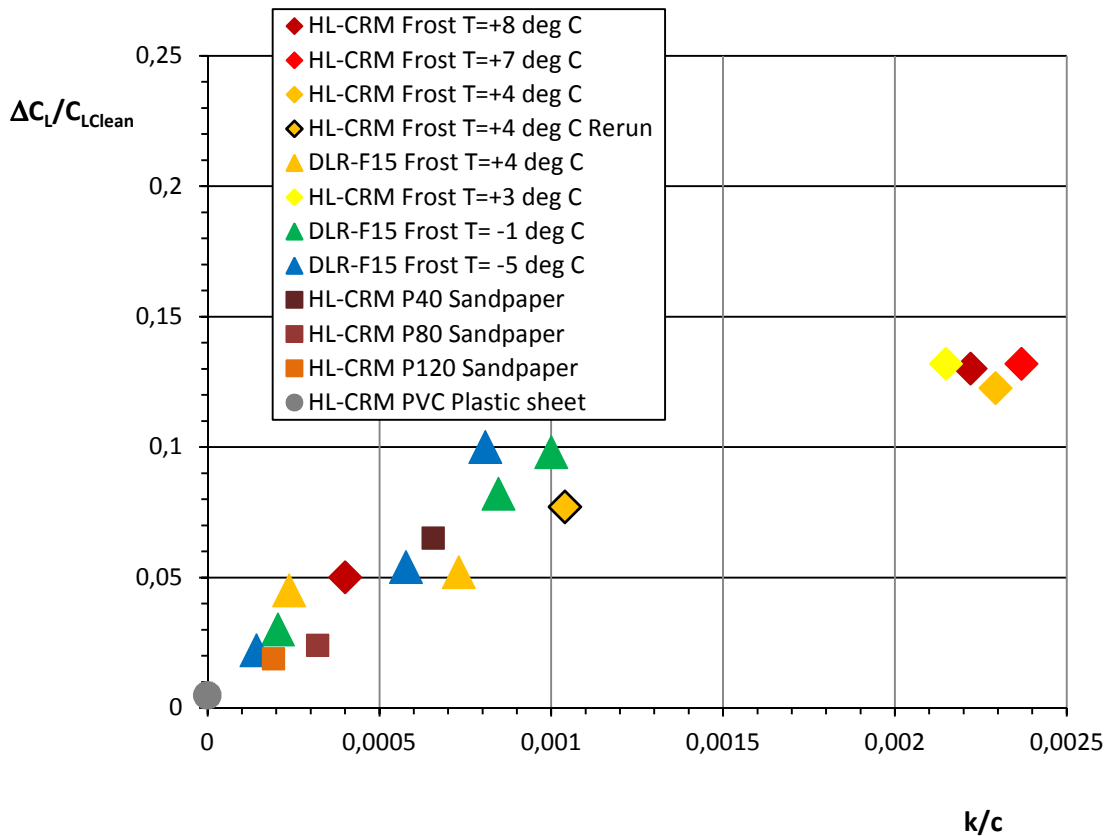


**Figure 67.** Relative Lift coefficient reduction as function of dimensionless surface roughness height (data also from ref. [1], [2] and [16]).

### 3.6.3 Boundary layer displacement thickness

The boundary layer displacement thickness values, corresponding to the lift force measurements, were measured with two boundary layer rakes at the aft edge of the airfoil main element. The measurement interval was 0,02 seconds. A moving averaging over 26 values, corresponding to a time period of 0,52 seconds, was performed to smooth out the measured pressures. In spite of this the time histories show quite detailed characteristics.

The measured boundary layer displacement thicknesses on clean wing are collected into Figure 68. The measurements show a small variation at constant angle of attack after the rotation although the results should be the same. This is due to inaccuracies in pressure measurements, angle of attack after rotation and all other sources of possible variations. It is evident in the figure that the results of the left and right hand side rakes are grouped at slightly different levels of about 0,7 mm. Obviously the rakes are slightly different or are positioned at slightly different levels from the wing surface or in slightly different directions.

The average values of each curve after the rotation were calculated using 250 measurement points corresponding to a time period of 5 seconds. The average value of the clean wing displacement thicknesses of the four left hand side rake measurements gave after the rotation a value  $\delta^*=5,32$  mm. On the right hand side the average value was  $\delta^*=4,63$  mm. The range of the four measurements was on both sides within  $\Delta\delta^*=0,02$  mm. On one rake the repeatability seems to give a maximum deviation from the average value  $\Delta\delta^*=0,5*0,02=0,01$  mm. When calculating the difference of two boundary layer displacement thicknesses the accuracy is reduced to  $\Delta\delta^*=\sqrt{2}*0,01=0,014$  mm. This is a very good repeatability when the displacement thicknesses are more than 4 mm for the clean wing and even more with the PVC sheet. The absolute accuracy of the displacement thickness measurement was however less as the left and right hand side rakes give different results. The accuracy range was  $5,32-4,63\pm 0,02=0,71$  mm and thus the maximum deviation was  $\pm 0,36$  mm, which is better than 10% on the clean wing displacement thickness.

Time histories of the boundary layer displacement thickness with the PVC plastic sheet are presented in Figure 69. The average 250 point displacement thickness values, corresponding to a time period of 5 seconds, were calculated for the flight condition after the model rotation. An example of a boundary layer velocity profile at a selected time instant after the model rotation is presented in Figure 70 to give some feel for the precision needed in the measurements. The effects due to the PVC sheet are fairly small. A more extensive comparison of the relative effects of sandpapers, anti-icing fluid, PVC plastic sheet and Cold soaked Fuel Frost is presented in Figure 71. Notice that the tunnel speed has been slightly different in the studied cases.

The displacement thickness increase due to the PVC sheet was determined in the above mentioned figures by calculating the average boundary layer thickness during 5 seconds after the rotation with and without the PVC sheet on the wing. The results are summarized for the PVC plastic sheet in Table 14. The change in the displacement thickness is the difference of the measured sandpaper value and the clean wing value. The displacement thickness increments are calculated separately for the left and right hand sides to minimize the rake measuring system error. The difference of the increment is now  $1,67-1,37=0,30$  mm. The total error could be  $\sqrt{2}*(0,02/2+0,30)=\pm 0,44$  mm. This is about 32% of the small increment value due to the PVC plastic sheet.

The dimensionless boundary layer displacement thickness increment due the PVC plastic sheet is presented together with previous measurements of Cold Soaked Fuel Frost and sandpapers in Figure 72 as function of dimensionless roughness height, because this was the relevant parameter for lift reduction. There was no noticeable evaporation/ melting of the frost before rotation in the tested temperatures. The figure shows an increasing increment with increasing roughness height. Figure 73 shows the relative lift reduction as function of the dimensionless boundary layer displacement thickness increment. Here a

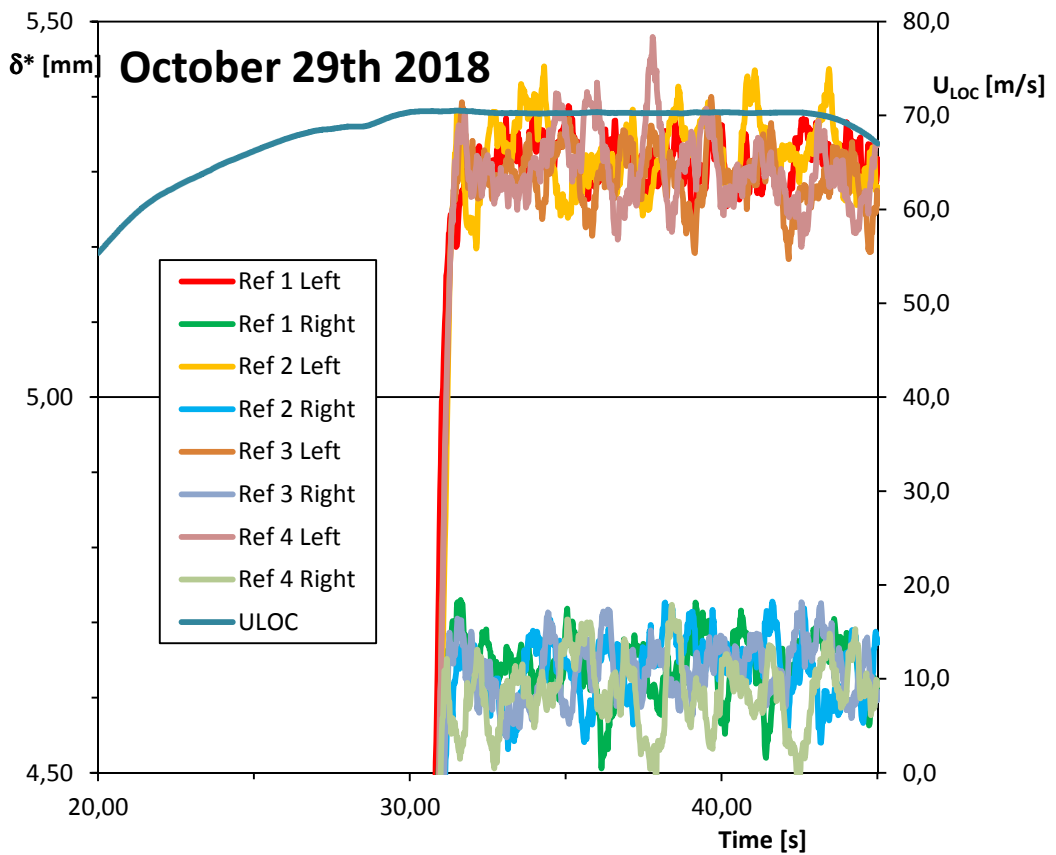
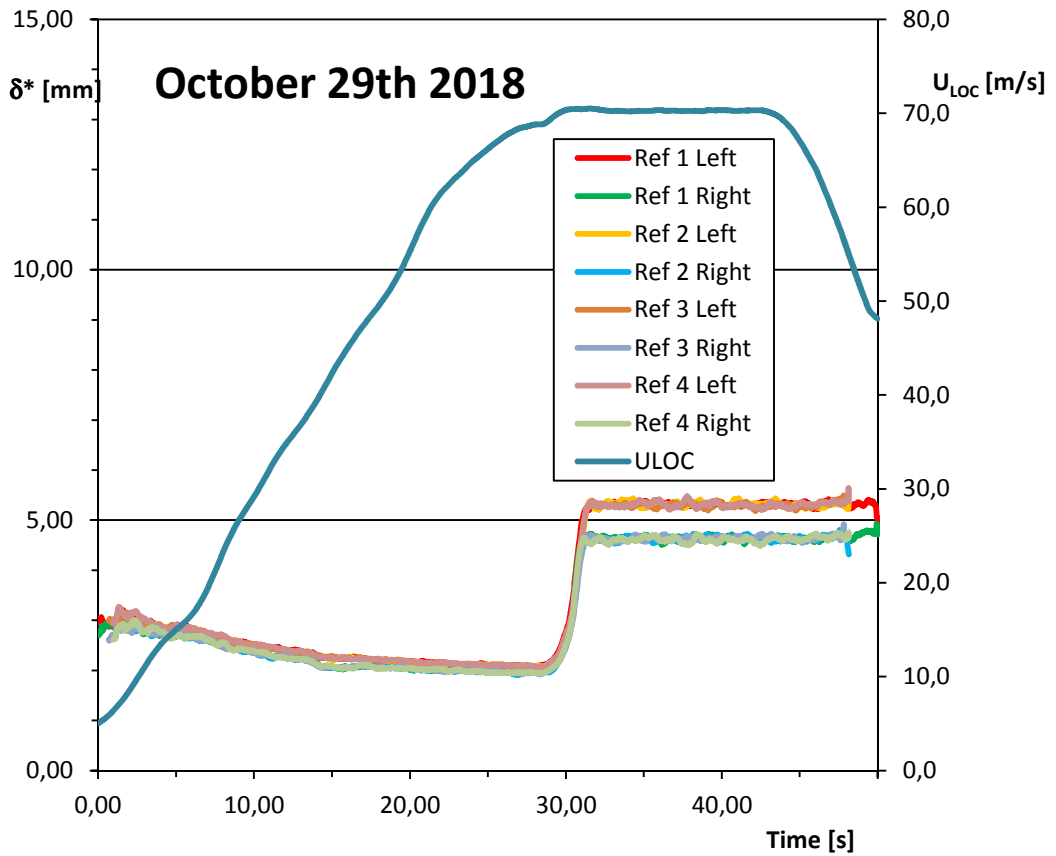


**Figure 68.** Boundary layer displacement thickness  $\delta^*$  as function of time during a simulated take-off on clean wing measurements.

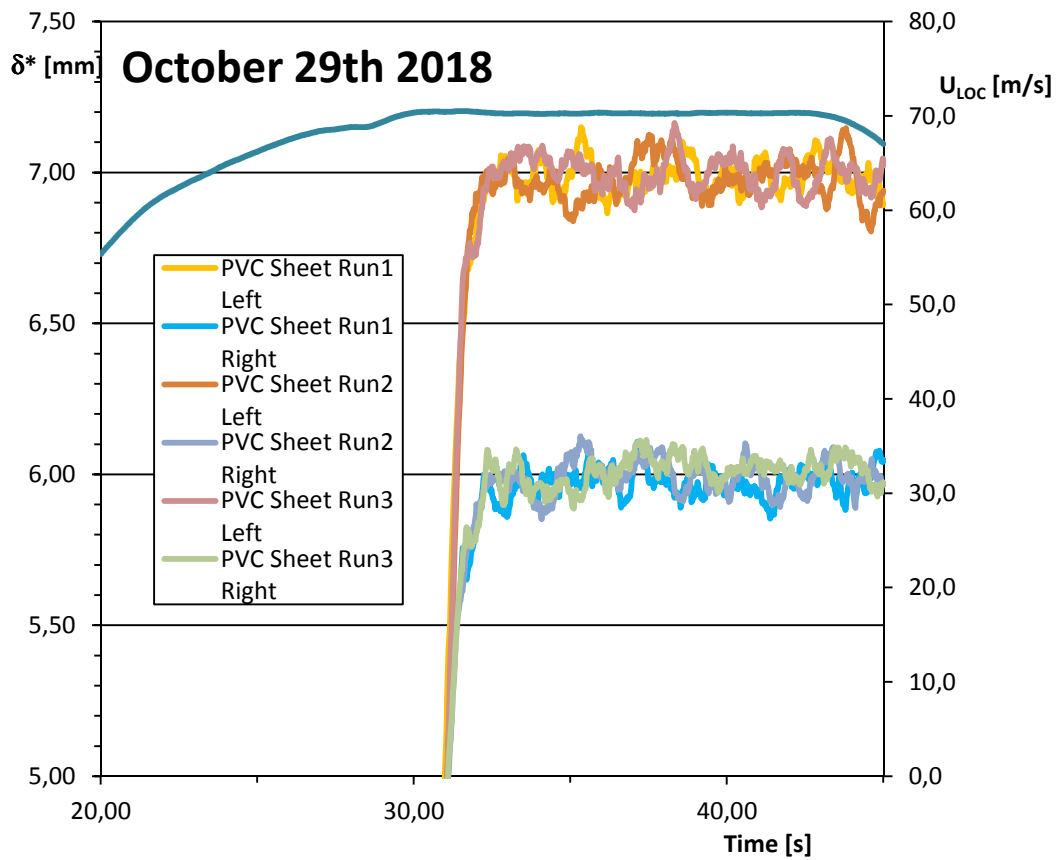
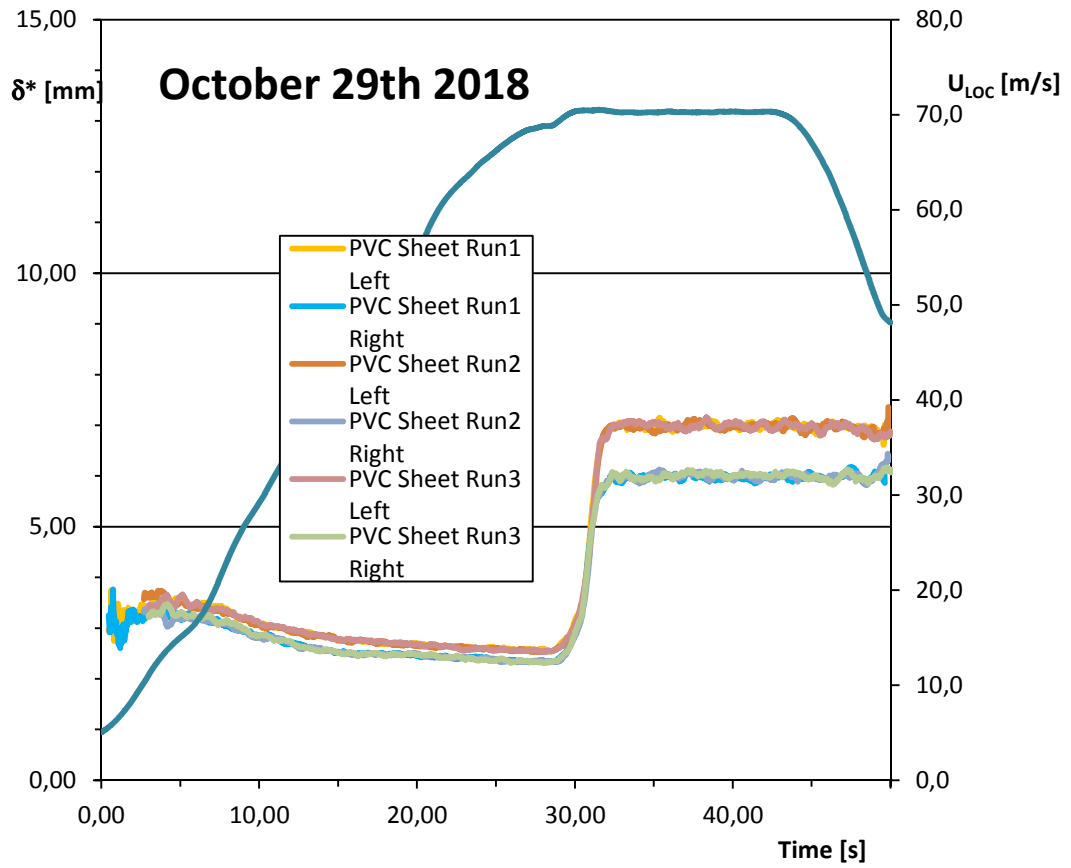


**Figure 69.** Boundary layer displacement thickness  $\delta^*$  as function of time during a simulated take-off with PVC plastic sheet on the wing model.

### November 29th 2018

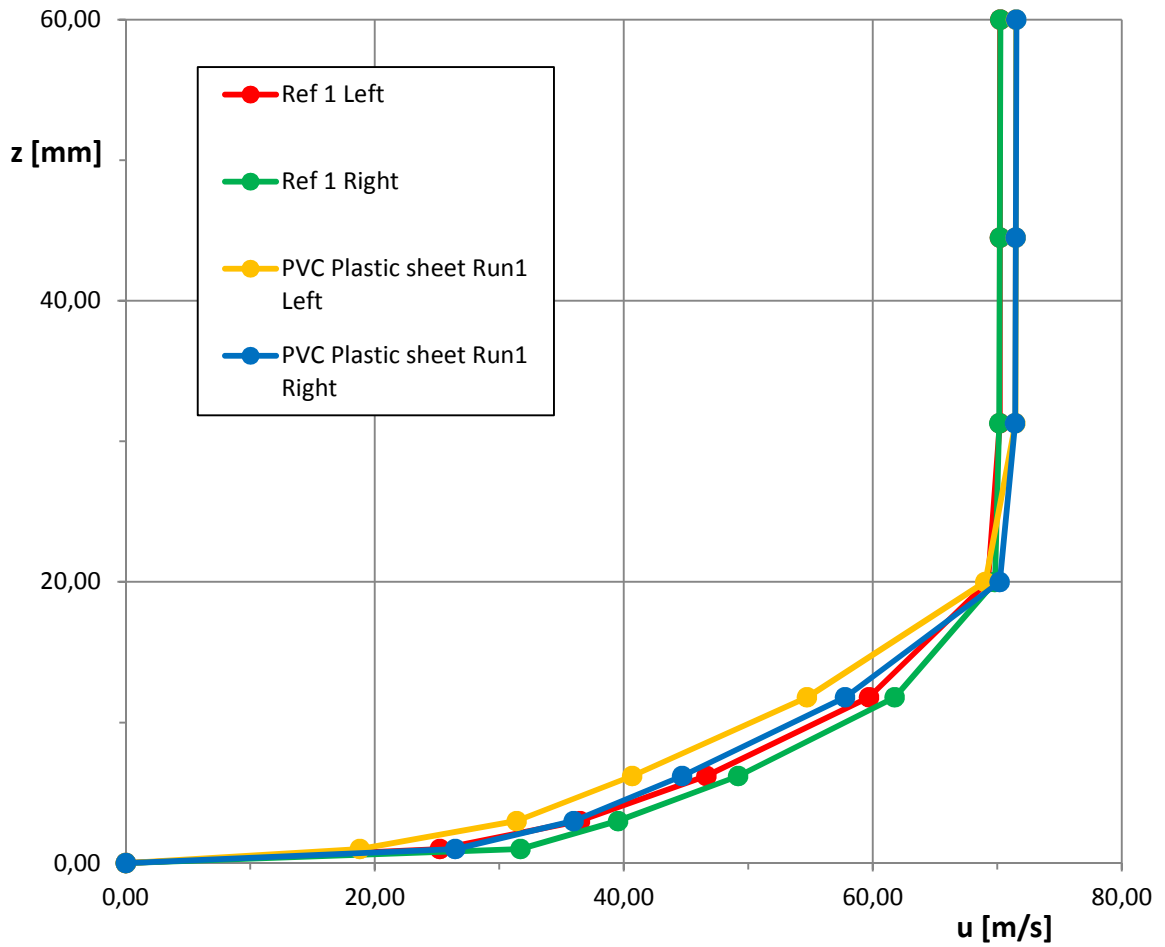


**Figure 70.** Boundary layer velocity profiles after wing model rotation.

fairly linear trend of increasing lift loss is shown as function of the dimensionless displacement thickness increment

**Table 14.** Boundary layer displacement thickness and lift coefficient change for PVC plastic sheet based on the measurements in Figure 68 and Figure 69.

Case	t/c	k/c	$\delta^*$ [mm]		$\Delta\delta^*$ [mm]		$\Delta\delta^*/c$	$\frac{C_L}{C_{L,Clean}}$
			Left	Right	Left	Right		
Clean wing	0	0	5,32	4,63	0	0	0	0
PVC Plastic sheet	0,00205	0	6,99	6,00	1,67	1,37	0,00243	0,005

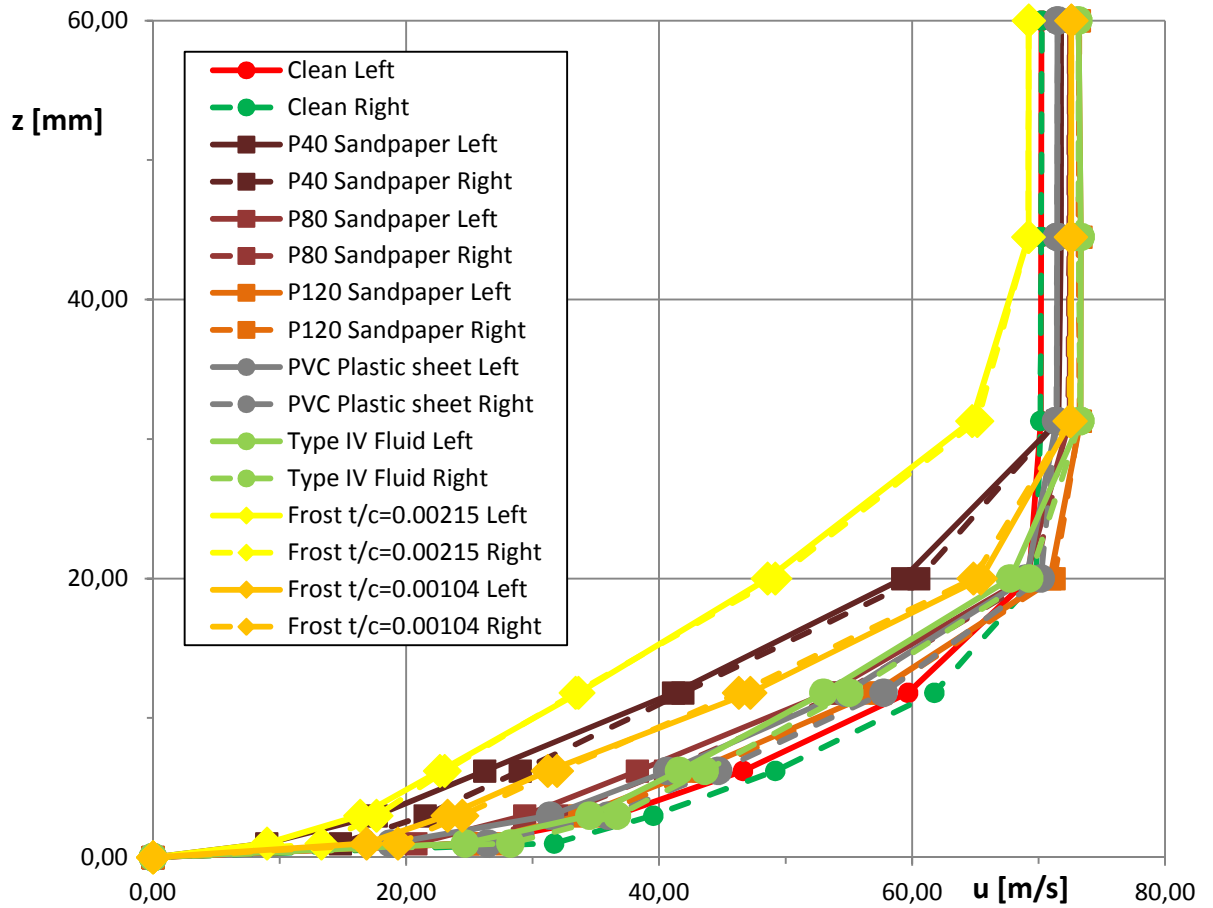


**Figure 71.** Boundary layer velocity profiles just after wing model rotation. The frost cases are from the measurements of March 21st and 24th of ref. [2].

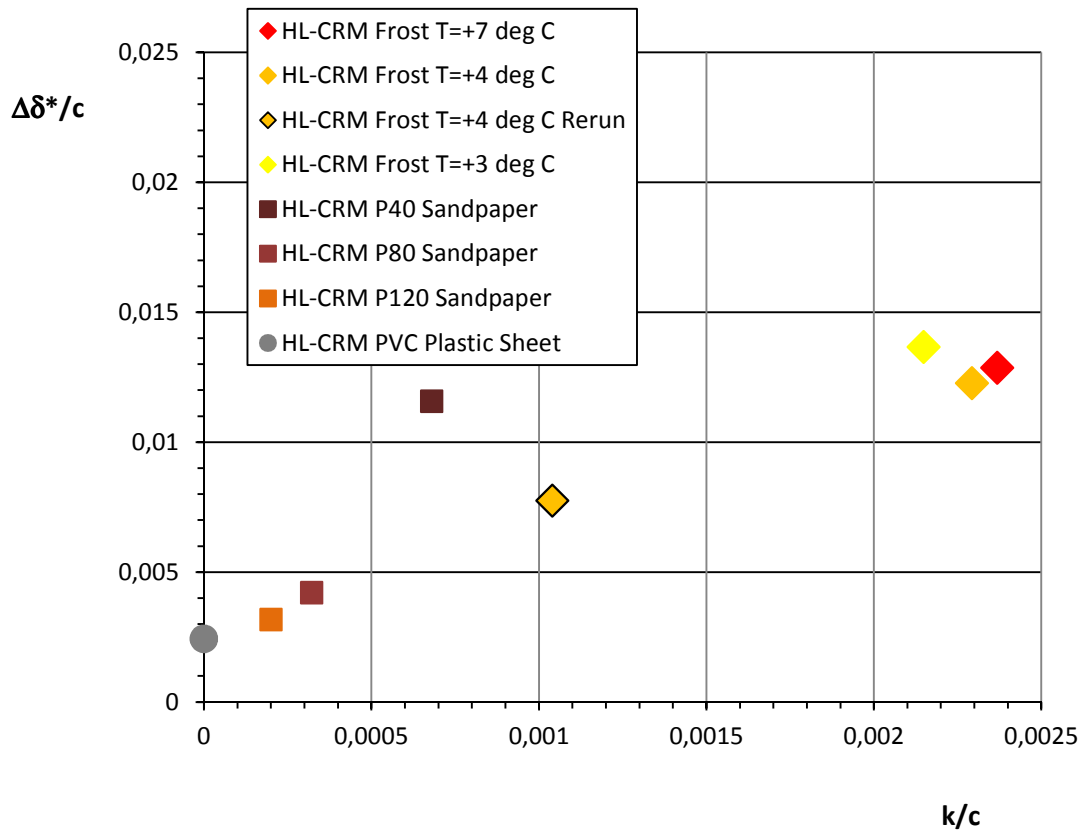


**Figure 72.** Dimensionless boundary layer displacement thickness increment as function of dimensionless surface roughness height (data also from ref. [2]).

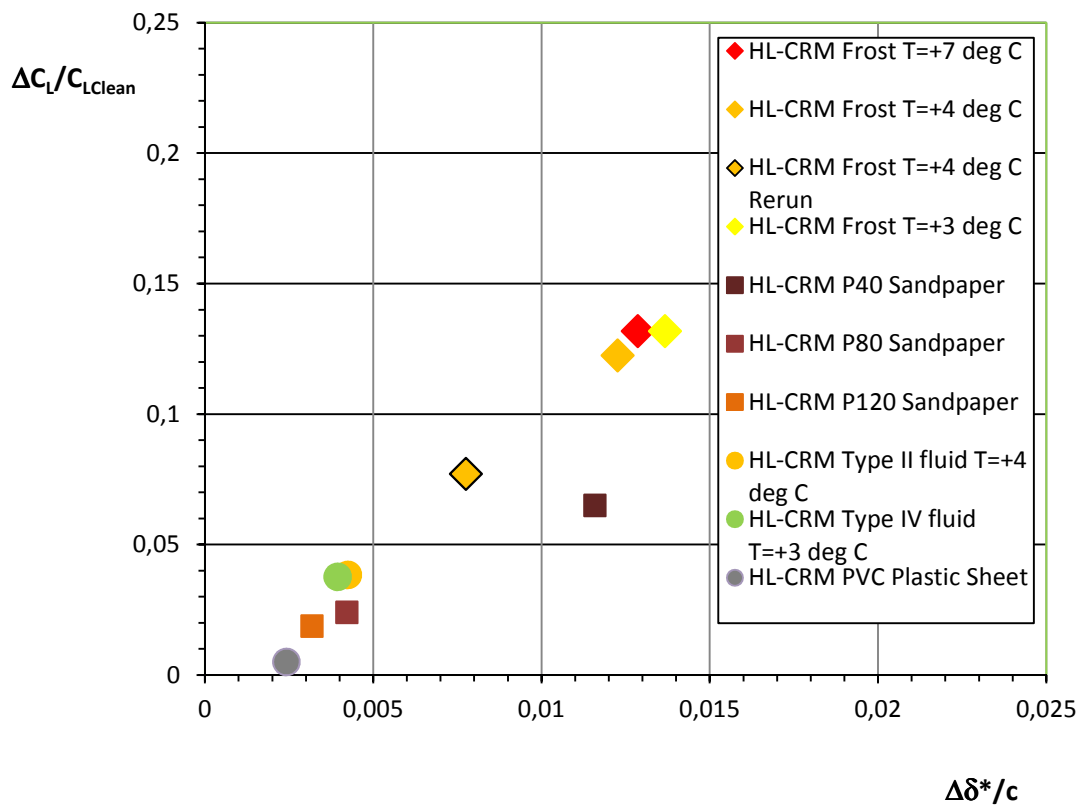


**Figure 73.** Relative lift coefficient reduction as function of dimensionless boundary layer displacement thickness increment (data also from ref. [2]).

## 4 Conclusions

The oil flow studies showed, that there was at the test Reynolds number of 1,3 million no flow separation present on the clean wing model upper surface at the junction of the wing and the end plate. Because the wing model rotation in the take-off sequence takes place at a higher Reynolds number, the performed test is conservative for the clean wing. The end plate contains a hole in the vicinity of the flap leading edge permitting flow from the higher pressure outboard of the end plate to the wing upper surface. As the hole functions the same way independent of if there is contamination on the wing surface or not, it is likely that there will not be separation on a contaminated wing either.

Wind tunnel measurements with different frost, sandpapers and smooth PVC plastic sheet on the wing model upper surface showed that the dimensionless surface roughness height is a more relevant parameter for lift coefficient reduction than the added dimensionless thickness. The lift coefficient reduction increased fairly linearly with dimensionless boundary layer displacement thickness increment with somewhat different slopes for frost and sandpaper.

Wind tunnel measurements with Type II and IV anti-icing fluids showed a lift reduction of about 4%. Relative lift coefficient reduction as function of dimensionless boundary layer displacement thickness increment fitted fairly well with the data of frost, sandpapers and a smooth PVC sheet.

## References

- [1] Koivisto P., Preliminary Cold Soaked Fuel Frost Studies with CRM Wing Model, Trafi Research Reports 12-2016, 2016, 11 p.
- [2] Soinne E., Rosnell T., Viljanen N., Aerodynamic, Laser and Photogrammetry Measurements on CRM Wing Model with Frost, Finnish Transport Safety Agency, Trafi Research Reports 11-2017, Helsinki, Finland, 2017, 60 p.
- [3] Hurme M., Measurement certificate, Aalto University, School of Engineering, Department of Applied Mechanics, 2015, 3 p.
- [4] Lacy D.S., Sclafani A.J., Development of the High Lift Common Research Model (HL-CRM): A Representative High Lift Configuration for Transonic Transports, AIAA paper 2016-0308, 24 p.
- [5] Kivekäs J., NASA HL-CRM (take-off) 2D-section definition for Frostwing-studies, Arteform Ltd Memo 20160519, 6 p.
- [6] Hoerner S.F., Fluid dynamic lift, second edition, 1985, 484 p.
- [7] Torenbeek E., Synthesis of subsonic airplane design, Delft University Press, 1976, 598 p.
- [8] Koivisto P., Effects of Anti-icing Treatment on Lift Degradation during Simulated Take-off, Finnish Transport Safety Agency Trafi Publications 25-2103, Helsinki, Finland, 2013, 22 p.
- [9] Kegerise M.A., Neuhart D.H., Wind Tunnel Test of a Risk-Reduction Wing/Fuselage Model to Examine Juncture-Flow Phenomena, NASA/TM-2016-219348, 2016, 118 p.
- [10] Hill E.G., Zierten T.A., Aerodynamic Effects of Aircraft Ground Deicing/Anti-Icing Fluids, Journal of Aircraft, Vol. 30, No.1 Jan-Feb 1993, page 24-34.
- [11] Bragg M.B., Heinrich D.C., Valarezo W.O, McGhee R.J., Effect of Underwing Frost on a Transport Aircraft Airfoil at Flight Reynolds Number, Journal of Aircraft Vol. 31, No. 6, 1994, pp. 1372, 1379.
- [12] Kivekäs J., Initial double rake tests CRM Frostwing, Arteform Ltd Internal memo, April 3rd 207, 10 p.
- [13] Delery J.M., Physics of Vortical Flows. Journal of Aircraft Vol. 29, No. 5, Sept.-Oct. 1992.
- [14] Simpson R.L., Junction Flows, Annual Review of Fluid Mechanics, 2001, vol 33, p. 415-443.
- [15] Policy Statement, Type Ceertification Policy for Approval of Use of Type II,III and IV Deicing/Anti-icing Fluids on Airplanes Certificated Under DFR Parts 23 and 25, Policy No. PS-ACE-23-05 PS-ANM-25-10, Federal Aviation Admnistration, 03/05/2015,14p.

- [16] Koivisto P., Effects of Cold Soaked Fuel Frost on Lift Degradation during Simulated Take-off, Finnish Transport Safety Agency Trafi Research Reports 4-2105, Helsinki, Finland, 2015.
- [17] SAE Aerospace Recommended Praactice ARP 6852 Rev 15.1, Methods and Processes for Evaluation of Aerodynamic Effects of SAE Aircraft Ground Deicing/Anti-icing Fkuids, SAE Aerospace, Montreal 2013, 77p.
- [18] Broeren A.P.,Riley J.T., Review of the Aerodynamic Acceptance Test and Application to Anti-Icing Fluids Testing in the NRC Propulsion and Icing Wind Tunnel, NASA/TM-2012-216014, 2012, 34 p.